

**The Age and Origin of Lithospheric Mantle Beneath Central Victoria Island  
and Parry Peninsula, Northern Canada**

by

Laura Elise Brin

A thesis submitted in partial fulfillment of the requirements for the degree of

Master of Science

Department of Earth and Atmospheric Science

University of Alberta

©Laura Elise Brin, 2016

## **Abstract**

New mineral major and trace element chemistry, bulk rock major element chemistry plus bulk rock and olivine PGE-Re-Os isotope data are presented for kimberlite-borne mantle xenoliths from Central Victoria Island, Nunavut and Parry Peninsula, Northwest Territories. The data, along with new and published mineral concentrate data from till, are used to constrain the composition, thickness and age of the lithospheric mantle beneath these two regions.

Geotherms constructed from single clinopyroxene thermobarometry on xenoliths and concentrate grains confirm that the lithospheric root in both locations extends into the diamond stability field (Central Victoria Island 120-215km; Parry Peninsula = 144-185km).

Although the highly refractory olivine MG-numbers of both peridotite suites and their very low bulk-rock Al contents indicate the presence of mantle keels as depleted as Archean mantle, the Re-Os and PGE data indicate that the bulk of the lithospheric mantle formed between ~ 2.3 and 1.8 Ga.

## **Dedication**

For Courtney

who without this would never have been possible

## Acknowledgements

First I would like to thank my supervisor Graham Pearson, for creating a project that encompassed everything I love about geology, for the many opportunities this project has provided and for the support and encouragement throughout. To my committee: Graham Pearson, Thomas Stachel, Tom Chacko and Bruce Kjarsgaard, for taking the time to read my thesis and for the invaluable feedback. To Bruce Kjarsgaard and Alex Miskovic for the brilliant prelude to grad school and the opportunity to explore the Canadian Arctic. Thank you to Bruce Kienlen from Diamonds North, Steve Reford from Darnley Bay and Mike Sellers from DeBeers for providing the samples used for this project. To the many people who gave me help along the way: Mark Labbe, Sergei Matveev, Andrew Locock, Steve Creighton, Kathy Mather, Yan Luo and for an amazing lab group - Kate Hogberg, Dave Dockman, Pedro Waterton, Janina Czas, Yannick Bussweiler, Mandy Krebs, Amy Riches, Chiranjeeb Sakar, Jingao Lui, Qiao Shu, - I could not have asked for more.

A special thanks to Sarah Woodland who not only taught me so much about geochemistry but also about life and happiness. To Shaunaugh Whelan, Kate Hogberg, Stephanie Fleck, Chelsey and Shaun Harlton, who supported me, reminded me to have a life, and made sure I did not spend all of my time in the lab! To my parents, Pat and Norm Brin, for endless encouragement and love. And to Courtney. I can not imagine how I could have done this without you. I owe you so much, more than can ever be expressed.

## Table of Contents

<b>CHAPTER 1: Introduction and Regional Geology.....</b>	<b>1</b>
1.1 Introduction - Objectives of the Study.....	1
1.2 Regional Geology .....	3
1.2.1 Circum-Slave Geology.....	3
1.2.2 Victoria Island.....	4
1.2.3 Parry Peninsula .....	7
<b>CHAPTER 2: Samples and Methods.....</b>	<b>10</b>
2.1 Xenoliths .....	10
2.2 Mineral concentrate data.....	10
2.3 Sample Preparation .....	11
2.4 Analytical methods and standards .....	12
2.4.1 Electron Microprobe .....	12
2.4.2 X-ray Fluorescence .....	12
2.4.3 Re-Os Analytical Methods.....	13
2.4.4 PGE analysis .....	13
2.4.5 Trace element determinations .....	14
2.5 Thermobarometry .....	16
<b>CHAPTER 3: Results.....</b>	<b>17</b>
3.1 Petrography .....	17
3.1.1 Central Victoria Island peridotites .....	17
3.1.2 Parry Peninsula peridotites .....	19

3.2 Mineral Chemistry .....	22
3.2.1 Xenoliths.....	22
3.2.2 Concentrate Mineral Chemistry.....	34
3.3 Garnet Trace Element Chemistry .....	36
3.3.1 Xenoliths.....	36
3.3.2 Garnet Concentrate .....	37
3.4 Thermobarometry .....	39
3.4.1 Ni-in-garnet thermometer .....	39
3.4.2 Single Clinopyroxene Thermobarometer.....	41
3.4.3 Estimating Pressures from Ni-temperatures .....	42
3.5 Bulk Rock Major Element Chemistry and Modal Mineralogy.....	45
3.6 Re-Os Systematics .....	49
3.6.1 Isotope Systematics.....	49
3.6.2 Model Ages.....	51
3.7 Platinum Group Elements .....	54
<b>CHAPTER 4: Discussion .....</b>	<b>59</b>
4.1 Metasomatic interactions .....	59
4.1.1 Bulk rock compositions .....	59
4.1.2 Garnet trace elements.....	59
4.2 Melt Depletion .....	64
4.2.1 Mineral Chemistry and Major Element Evidence .....	64
4.2.2 PGE Evidence .....	68
4.2.3 Metasomatic disturbance of PGEs .....	72

4.3 Age Depletion and Lithosphere Formation in the Context of Regional Geology.....	75
4.4 Thermal Structure of the Lithosphere and Diamond Potential of the Parry Peninsula and Central Victoria Island .....	81
4.4.1 Central Victoria Island.....	83
4.4.2 Parry Peninsula .....	84
<b>CHAPTER 5: Conclusions.....</b>	<b>87</b>
5.1 Future Work.....	89
5.1.1 Central Victoria Island.....	89
5.1.2 Parry Peninsula .....	90
<b>References.....</b>	<b>92</b>
<b>APPENDICES.....</b>	<b>100</b>
Appendix A1 Sample and Data Sources.....	101
Appendix A2 Standards and Reproducibility .....	105
Appendix A3 Petrography .....	107
Appendix A4 Garnet Repeatability.....	127
Appendix A5 Concentrate Data.....	128
A5.1 Concentrate mineral chemistry .....	128
A5.2 Thermobarometry for mineral concentrate .....	128
A5.2.1 Single Clinopyroxene.....	128
A5.2.2 Nickel in Garnet Thermometer .....	132
Appendix 6 Thermobarometry.....	133
Appendix 7 Central Victoria Island mineral grain re-analysis .....	138

A7.1 Mineral Chemistry .....	138
A7.2 Thermobarometry.....	150
A7.2.1 Single Clinopyroxene.....	150
A7.3 Garnet trace elements.....	153
Appendix A8 Model ages .....	154

## List of Tables

Table 3.1 Major element compositions of Parry Peninsula peridotites.....	24
Table 3.2 Major element compositions of central Victoria Island peridotites.....	28
Table 3.3 Garnet trace elements for central Victoria Island .....	38
Table 3.4 Representative nickel-in-garnet thermometer results from xenolith mineral separates for Central Victoria Island.....	40
Table 3.5 Temperatures and pressures for Parry Peninsula.....	42
Table 3.6 Whole rock compositions from XRF for central Victoria Island and Parry Peninsula peridotites .....	46
Table 3.7 Re-Os Isotopic systematics for Central Victoria Island peridotites, Parry Peninsula peridotites and their olivines. ....	51
Table 3.8 PGE concentrations for central Victoria Island whole rock xenoliths, Parry Peninsula whole rock xenoliths and Parry Peninsula olivines. ....	56
Table A1.1 Central Victoria Island kimberlites UTM NAD83 zone 10.....	101
Table A1.2 Parry Peninsula kimberlites UTM NAD83 zone 12,13 .....	103
Table A2.1 Standards used for calibration for the Cameca and Jeol microprobe instruments.....	105
Table A2.2 Elemental Count times for Microprobe.....	105
Table A2.3 Reproducibility of secondary standards at 2 standard deviations of the mean difference.....	106
Table A3.1 - Central Victoria Island xenolith sample list with data capture.....	107
Table A3.2 Parry Peninsula xenolith sample list with data capture .....	108
Table A4.1 Garnet repeatability for SnO-24.....	127
Table A5.1 Count of concentrate grains by mineralogy .....	128
Table A5.2 Temperatures and pressures of central Victoria Island clinopyroxene concentrate .....	129

Table A5.3 Temperatures and pressures of Parry Peninsula clinopyroxene concentrate .....	130
Table A5.4 Nickel temperatures from central Victoria Island garnet concentrate .....	132
Table A6.1 Parameters used for FITPLOT thermobarometry.....	133
Table A7.1 DeBeers EDS garnet compositions used for industry comparison ..	140
Table A7.2 University of Alberta Electron Microprobe garnet compositions....	141
Table A7.3 DeBeers EDS clinopyroxene compositions used for industry comparison.....	142
Table A7.4 University of Alberta WDS clinopyroxene compositions .....	146
Table A7.5 University of Alberta WDS versus Industry EDS single-clinopyroxene thermobarometry.....	151
Table A7.6 Concentrate garnet trace element trends .....	153

## List of Figures

Figure 1.1 Map of Canada showing kimberlite localities and regional geology modified from Kjarsgaard. Project localities highlighted.....	2
Figure 1.2 Surficial Geology map of Victoria Island, Northern Canada..	6
Figure 1.3 Surficial Geology of Parry Peninsula NWT.....	8
Figure 2.1 Tracking of DrOsS secondary standard.....	14
Figure 2.2 $^{61}\text{Ni}$ to $^{60}\text{Ni}$ (ppm).....	15
Figure 3.1 Garnet grain fragments in epoxy mounts. ....	18
Figure 3.2 BSE images of garnet morphology for peridotite sample SnO-1.....	18
Figure 3.3 Parry Peninsula peridotite textures in thin section .....	20
Figure 3.4 Parry Peninsula peridotite xenoliths.....	21
Figure 3.5 Parry Peninsula peridotite sample DB2D displaying five phases. ....	22
Figure 3.6 Olivine MG# for central Victoria Island and Parry Peninsula peridotite xenoliths.....	30
Figure 3.7 CaO (wt%) versus MG# for olivines.....	31
Figure 3.8 TiO <sub>2</sub> concentration versus MG# for clinopyroxene.....	32
Figure 3.9. CaO vs Cr <sub>2</sub> O <sub>3</sub> for xenolithic garnets from central Victoria Island.....	33
Figure 3.10 CaO vs Cr <sub>2</sub> O <sub>3</sub> for xenolithic garnets from Parry Peninsula. ....	34
Figure 3.11 Chondrite-normalized rare earth element plots for garnets from Central Victoria Island peridotite xenoliths.....	39
Figure 3.12 Probability density diagram Ni-in garnet temperatures from central Victoria Island xenoliths.....	41
Figure 3.13 FITPLOT (Mather <i>et al.</i> , 2011) geotherms for Parry Peninsula .....	60
Figure 4.2 A: (Sm/Dy) <sub>N</sub> vs FeO (wt%) for garnet. ....	62
Figure 4.3 Covariation of yttrium and zirconium for central Victoria Island garnets.....	63
Figure 4.4 Histograms of Olivine MG#.....	65

Figure 4.5 Olivine MG# vs. melt fraction for residual peridotites.....	66
Figure 4.6 Spinel Tri-plot of Fe <sup>3+</sup> -Cr-Al .....	67
Figure 4.7 Variation of bulk rock Ir and Pd with Al <sub>2</sub> O <sub>3</sub> .....	70
Figure 4.8 Covariation plots of normalized Pd/Ir and Pt/Ir versus Al <sub>2</sub> O <sub>3</sub> . ....	71
Figure 4.9 (Os/Ir) <sub>N</sub> versus (Pt/Ir) <sub>N</sub> for central Victoria Island, Parry Peninsula and circum-cratonic peridotites. ....	73
Figure 4.10 Variation of <sup>187</sup> Os/ <sup>188</sup> Os isotopic ratios with (Pd/Ir) <sub>N</sub> and (Pt/Ir) <sub>N</sub> ....	75
Figure 4.11 Calculated T <sub>RD</sub> model age versus actual age of melting for varying degrees of melt removal from peridotite starting with PUM – like composition.....	76
Figure 4.12 Probability density plot for T <sub>RD</sub> model ages of central Victoria Island and Parry Peninsula peridotites.....	77
Figure 4.13 Whole rock MG# versus Mg/Si ratios.....	81
Figure 4.14 Probability density diagram of Ni-in-garnet temperatures for garnet till concentrate from central Victoria Island. ....	84
Figure 4.15 FITPLOT geotherm for Central Victoria Island, Parry Peninsula and Lac de Gras. ....	86
Figure A1.1 Location of kimberlites on Victoria Island.....	102
Figure A1.2 Location of kimberlites on Parry Peninsula .....	104
Figure A3.1 Hand sample images of central Victoria Island xenoliths in core ..	109
Figure A3.2 Hand sample images of central Victoria Island xenoliths in core ..	110
Figure A3.3 Hand sample images of central Victoria Island xenoliths in core ..	111
Figure A3.4 Hand sample images of central Victoria Island xenoliths in core ..	112
Figure A3.5 Thin section images of central Victoria Island xenoliths. ....	113
Figure A3.6 Thin section images of central Victoria Island xenoliths. ....	114
Figure A3.7 BSE images of SnO-1.....	115
Figure A3.8 Hand sample images of Parry Peninsula xenoliths in core.....	116
Figure A3.9 Hand sample images of Parry Peninsula xenoliths in core.....	117

Figure A3.10 Hand sample images of Parry Peninsula xenoliths in core.....	118
Figure A3.11 Thin section images of Parry Peninsula xenoliths.....	119
Figure A3.12 Thin section images of Parry Peninsula xenoliths.....	120
Figure A3.13 Thin section images of Parry Peninsula xenoliths.....	121
Figure A3.14 Thin section images of Parry Peninsula xenoliths.....	122
Figure A3.15: BSE images of Parry Peninsula xenoliths .....	123
Figure A3.16: BSE images of Parry Peninsula xenoliths .....	124
Figure A3.17 False colour BSE images of Parry Peninsula xenoliths.....	125
Figure A3.18 Electron microbeam mapping of DB8A.....	126
Figure A5.1 Victoria Island concentrate single-clinopyroxene temperatures and pressures by Kimberlite Trend.....	129
Figure A5.2 FITPLOT geotherm modeled on single-clinopyroxene temperatures and pressures from Parry Peninsula clinopyroxene concentrate.....	131
Figure A6.1 FITPLOT for Central Victoria Island xenoliths using Slave crustal parameters .....	134
Figure A6.2 FITPLOT for Parry Peninsula xenoliths with concentrate using Slave crustal parameters .....	135
Figure A6.3 FITPLOT for Central Victoria Island xenoliths using crustal parameters with lower crust heat generation. ....	136
Figure A6.4 FITPLOT for Parry Peninsula xenoliths with concentrate using crustal parameters with lower crust heat generation.....	137
Figure A7.1 EDS versus WDS for garnet concentrate. ....	139
Figure A7.2 EDS versus WDS for clinopyroxene concentrate.....	139
Figure A7.3 EDS versus WDS: Comparison of temperatures and pressures ....	150
Figure A8.1 $T_{RD}$ model ages for PP whole rock and olivines. ....	154
Figure A8.2 Probability density figure of $T_{RD}$ model ages for central Victoria Island and Parry Peninsula plot.....	156

## List of Abbreviations and Nomenclature

bdl	below detection limit
BSE	backscattered electrons images
°C	degrees Celsius
Chr	chromite
Cpx	clinopyroxene
CR#	chromium number: molar ratio of Cr/(Cr+Al)*100
CVI	Central Victoria island in reference to xenoliths
DrOsS	Durham Osmium standard
EDS	energy dispersion X-ray spectrometry
Fo	forsterite
g	gram
G9	lherzolitic garnets
G10	harzburgitic garnets
G10D	"D" suffix indicates a strong association with diamonds
Grt	garnet
GPa	gigapascal
HPA	High Pressure Asher
HREE	heavy rare earth elements
HSE	highly siderophile elements
kbar	kilobar
km	kilometer
LREE	light rare earth elements

MG#	magnesium number: molar ratio of Mg/(Mg+Fe)*100
$\text{mW/m}^2$	milliwatts per meter squared (unit of heat flow)
MREE	medium rare earth element
NIST	standard from the National Institute of International Standards
Ol	olivine
Opx	orthopyroxene
NTIMS	negative thermal ionization mass spectrometer
pdf	probability density figure
PGE	Platinum group elements
PP	Parry Peninsula in reference to xenoliths
ppb	concentration expressed at parts per billion
PPL	plain polarized light
ppm	concentration expressed at parts per million
$R^2$	correlation coefficient
REE	Rare earth elements
REE <sub>N</sub>	subscript "N" indicates normalization values
SCLM	Subcontinental Lithospheric Mantle
SEM	Secondary electron multiplier
T <sub>MA</sub>	"normal" model age
T <sub>RD</sub>	Re depletion model ages
WDS	wavelength dispersion X-ray spectrometry
wt%	concentration in weight percent
XPL	cross polarized light

# **CHAPTER 1: Introduction and Regional Geology**

## **1.1 Introduction - Objectives of the Study**

Due to its emergence as a global diamond resource, the mantle beneath the Slave craton has been of considerable economic and academic interest during the past two decades. In contrast, significant portions of subcratonic lithospheric mantle (SCLM) underlying other parts of Northern Canada have not been subjected to extensive petrological, geochemical, and geochronological study but could prove equally prospective for diamonds. In particular, the northerly extent of deep cratonic lithosphere in Arctic Canada, especially of the Slave craton, is poorly constrained at this time. Improved knowledge of the extent of cratonic mantle and its thermal history will have important implications for future diamond exploration in this region. This study focuses on characterizing the age and composition of lithospheric mantle beneath central Victoria Island, 500km to the North of the Slave craton, as well as beneath the Parry Peninsula, 700km Northwest of the western margin of the Slave craton (Figure 1.1).

Lithospheric mantle beneath Proterozoic terranes is thought by some authors to be distinct from that beneath Archean cratons. Archean cratonic mantle has experienced high degrees of melt removal and generally has a low geothermal gradient. In contrast, the standard model for mantle lithosphere beneath

Proterozoic terranes involves thinner lithosphere with higher heat flow and thermal gradients than Archean mantle (Haskerok and Chapman, 2011).

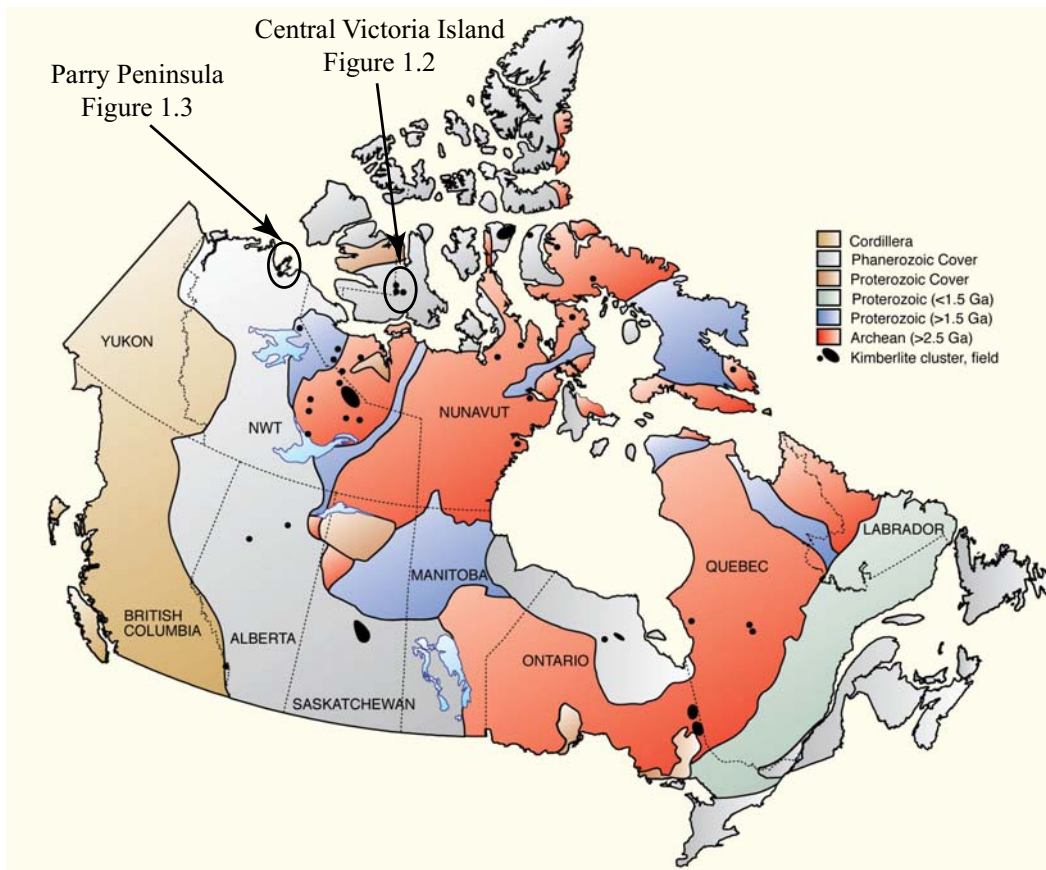


Figure 1.1 Map of Canada showing kimberlite localities and regional geology modified from Kjarsgaard. Project localities highlighted.

Until now, there have been no petrological or geochemical studies of the lithospheric mantle beneath Proterozoic crust in northern Canada, despite the fact that several kimberlite fields have been found to intrude through such crust. Here we present data from kimberlite-borne peridotite xenoliths recovered from drill cores of 1) the Snowy Owl kimberlite in central Victoria Island, NT, and 2) Darnley Bay kimberlites of the Parry Peninsula, NWT. Whether the lithosphere

that forms central Victoria Island is Archean or not is very contentious (e.g., Bleeker 2003) due to the single U-Pb zircon age obtained from this area. Whether the region represents a northerly extension of the Slave craton is an important issue to resolve within the context of regional tectonics. Similarly, while there are no extant outcrops of Archean crust within the Parry Peninsula area, the region has been named the “Mackenzie Craton” by some workers (Davies & Davies, 2013) due to the presence of kimberlites and abundant diamond-indicator minerals in the area. Clearly it is important to resolve the question of whether cratonic mantle underpins either of these two regions.

This study applies an integrated petrological and geochemical approach (mineral composition, bulk-rock major-element data, PGE abundances, Re-Os isotopes and garnet trace elements) to constraining the age, melt depletion history, metasomatism, thermal structure, formation and evolution of the lithosphere beneath central Victoria Island and the Parry Peninsula. The work compliments recent studies of circum-cratonic mantle in other regions (eg. Luguet *et al.*, 2009; Janney *et al.*, 2010) that compare lithospheric mantle beneath Archean and Proterozoic crustal regions and makes a possible assessment of the prospectiveness of such mantle for diamond potential.

## **1.2 Regional Geology**

### ***1.2.1 Circum-Slave Geology***

Northern Canada has a complicated collage of Archean cratons and Proterozoic suture zones that have been a coherent block since 1.7Ga (Hoffman, 1989).

Proterozoic terranes comprise 45% of the region but are understudied due to extensive Phanerozoic sedimentary cover. The Slave craton is nearest to both localities of this study, and is among the most investigated cratons in the world. Known kimberlites are highly concentrated in the center of province and extend upwards to the coast.

The western margin of the Slave craton is a succession of North-South trending belts added to the craton during the Proterozoic. The Wopmay Orogen, which formed from ~1.93-1.85Ga, comprises reworked Slave Craton basement and overlying Paleoproterozoic sedimentary cover rocks, as well as the accreted Hottah (1.95-1.89Ga) and Great Bear (1.88-1.85Ga) magmatic arcs (Hoffman, 1989; Jackson *et al.*, 2013, Ootes *et al.*, 2015). The Wopmay fault zone is considered to be the western extent of Archean crust.

### ***1.2.2 Victoria Island***

Victoria Island supra-crustal geology is mostly comprises Cambrian and Ordovician platformal carbonate units; however, basement rocks are exposed in the Minto, Wellington and Duke of York inliers (Figure 1.2). The largest of these inliers, the Minto inlier in the Northwest, consists of Paleoproterozoic Shaler Group rocks: deposits of tholeiitic flows overlying carbonate, evaporite and siliciclastic rocks that comprise the bulk of the stratigraphy (Campbell, 1981).

The oldest rocks on Victoria Island are located only in the Hadley Bay area as pink granitoids with cross-cutting granodiorites dated at 2405Ma (K-Ar, Thorsteinsson and Tozer, 1962). Franklin magmatism (723Ma) in this area is manifest as Neoproterozoic basalt flows and sills of the Natkusik Formation (Heaman *et al.*, 2003). Regional electromagnetic data also indicate the presence of two sets of diabase dykes; the NW-SE trending Mackenzie dykes (1270Ma) and the N-S trending 425Ma dykes (DNR internal report, 1999 *in* Kolebaba, *et al.*, 2003). The focus of the Mackenzie plume head has been proposed to be located off the SW shore of Victoria Island (Baragar *et al.*, 1996). The tectonic provenance of central Victoria Island is unclear as no Archean shield is exposed. Bleeker (2003) denotes this area as a possible extension of the Slave Craton but no published data exists to support this suggestion.

### *Kimberlites*

Victoria Island kimberlites occur along NW-SE trending parallel dyke array (Figure A1.1) comprising four main groups: the Galaxy structure, the Blue Ice trend, the Snowy Owl trend and the King Eider trend. Of the kimberlites explored in the latter two trends, 80% have been found to be diamondiferous (DNR news release, 2013). Perovskite dating of the Snowy Owl kimberlite produced a  $^{206}\text{Pb}/^{238}\text{U}$  date of  $271.2 \pm 2.6\text{Ma}$  (Heaman *et al.*, 2003). This date agrees with reported Pb/U date of 265-286Ma (Kolebaba *et al.*, 2003) but is older than an Ar-Ar phlogopite date of  $257 \pm 3\text{Ma}$  (Kahlert *in* Heaman *et al.*, 2003).

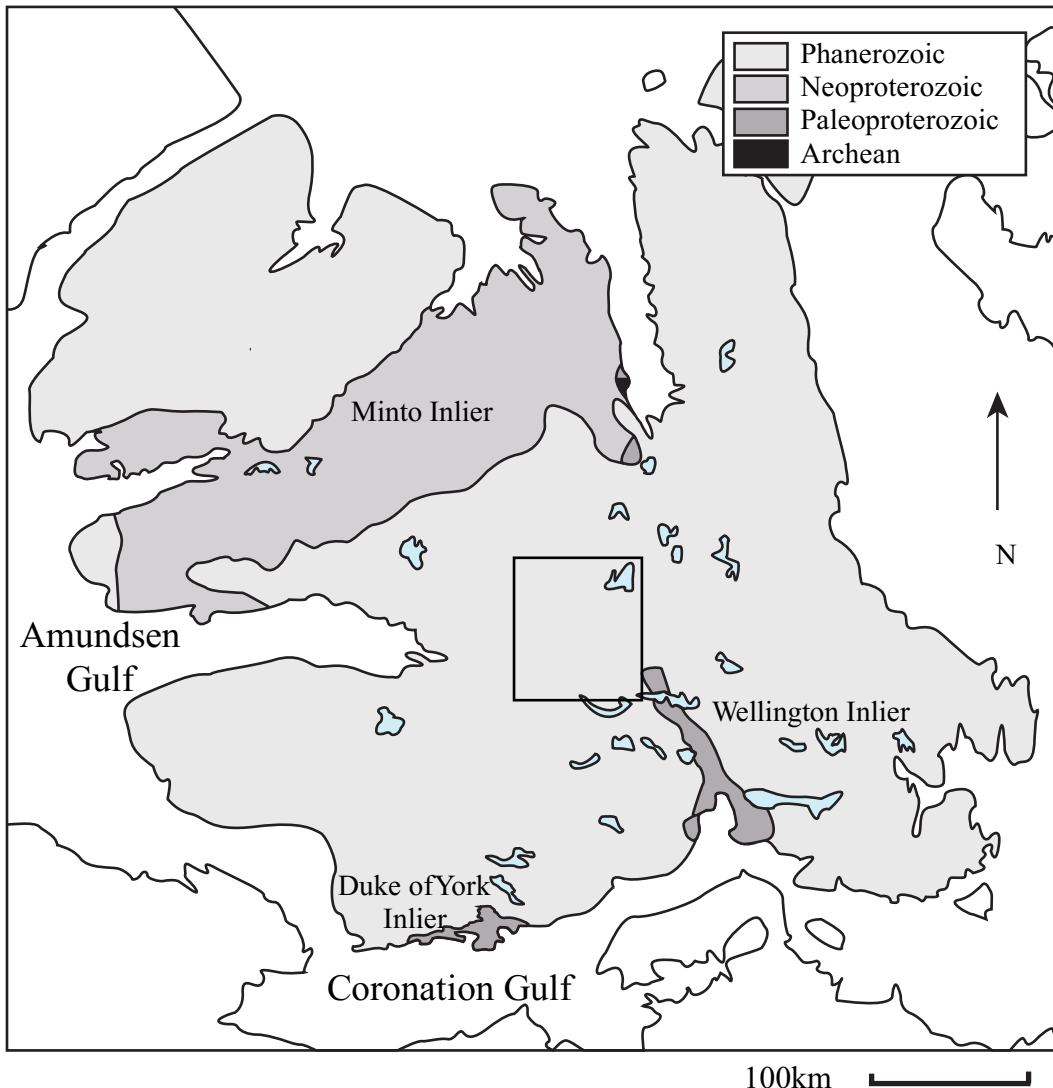


Figure 1.2 Surficial Geology map of Victoria Island, Northern Canada. Square indicates location of central Victoria Island kimberlites, for details see Appendix A1. Adapted from Rainbird et al. 1996.

### **1.2.3 Parry Peninsula**

The area of the Parry Peninsula, NWT, has been a center of mineral and diamond exploration since the 1950s; however, very little is known about the area geologically. Cherty dolomite units and quaternary moraines cover much of the peninsula (Yorath *et al.*, 1971). The Brock inlier, ~30km East of the Parry Peninsula, exposes basement rocks that likely underlie the Horton Plain region and Parry Peninsula. Sedimentary rocks correlated with the Shaler group, along with Franklin age intrusions comprise the Proterozoic component to this inlier (Rainbird *et al.*, 1994). These rocks are likely a structural extension of those seen in the Minto Inlier (Figure 1.2), as they fall along strike of the Minto antiformal structure.

The Parry Peninsula region is far outside of any recognized cratonic blocks (Bleaker, 2003). Nonetheless, the region is thought by some (e.g., Davies & Davies, 2013) to be underlain by an Archean mantle root due to the occurrence of diamonds and kimberlites. In models that involve cratonic basement and mantle, it is unclear whether this area represents a separate craton, or perhaps composite cratons, West of the Wopmay orogenic zone. The area has been referred to as Lena West due to its supposed similarities with diamond fields in Siberia and it has been suggested that a new craton, the 'Mackenzie craton', underpins this area and sources the kimberlites that erupt in an area ranging from the Amundsen Gulf,

south past the exploration properties south of Paulatuk to the Dharma kimberlite on the NE corner of Great Bear Lake (eg. Davies & Davies, 2013).

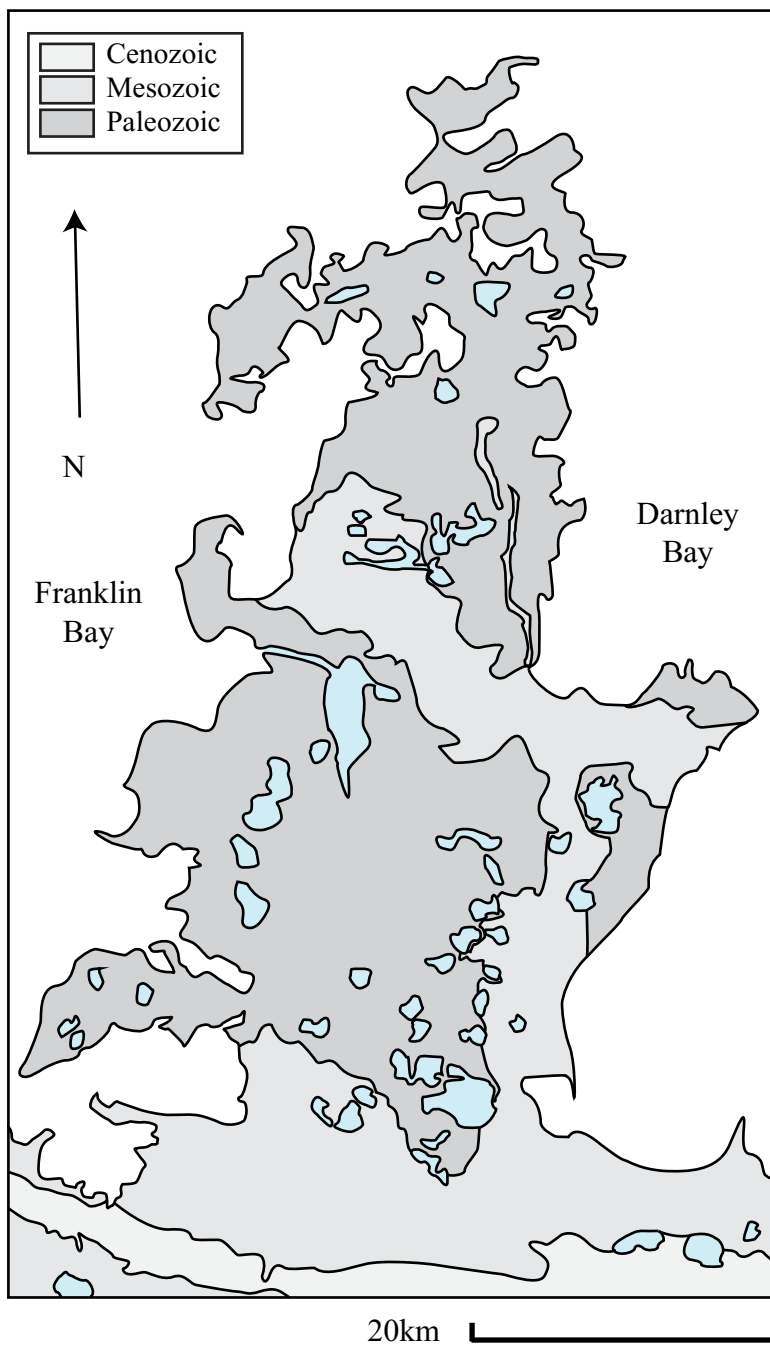


Figure 1.3 Surficial Geology of Parry Peninsula NWT. Adapted from Yorath *et al.* 1971.

The Parry Peninsula area was initially explored due to the presence of a large magnetic anomaly: the Darnley Bay Anomaly, which is the largest gravity anomaly in North America. Hornal (1970) and Stacey (1971) originally interpreted the anomaly as a basic or ultrabasic intrusion lying beneath the Proterozoic and Paleozoic sediments. This anomaly differs from other gravity anomalies in the Mackenzie Basin, such as the Mackenzie River Anomaly and Fort Simpson Anomaly, which are related to early Proterozoic magmatic arcs (Pilkington and Saltus, 2009). The Darnley Bay anomaly has also been found to be the source of a large magnetic variance which led to dynamic gravity and magnetic surveys to conclude that the anomaly represents a giant Cu-Ni-PGE deposit delineated by four plume centers (Reford, *et al.*, 2010). Surveying of circular magnetic anomalies resulted in the discovery of diamondiferous kimberlites in the Paulatuk area. One of these kimberlites has been dated at 270 Ma (Heaman *et al.*, 2003).

## **CHAPTER 2: Samples and Methods**

### **2.1 Xenoliths**

Central Victoria Island (CVI) xenoliths for this study were extracted from 22 drill cores of the Snowy Owl Kimberlite donated by Diamonds North Ltd. in conjunction with the Northwest Territories Geological Survey (NTGS). The xenoliths (n=36) range in size from 1cm to 8 cm and in weight from less than 1g to 76g. Fifteen samples were selected for further analysis based on size, minimal kimberlite contamination and minimal alteration. Where present, garnet and olivine grains were isolated as mineral separates.

Samples from the Parry Peninsula were donated by Darnley Bay Resources Ltd. Fifteen xenoliths were recovered from drill core, ranging in weight from 3g to 302g. The fresh nature of these samples permitted olivine mineral separates to be prepared for Re-Os isotope analysis as well as whole rock powders.

### **2.2 Mineral concentrate data**

Additional mineral concentrate data for the central Victoria Island kimberlite field came from various sources. Concentrate from the Snowy Owl kimberlite was provided by Diamonds North Resources Ltd., using materials used in their exploration campaign. All data from other kimberlites in the Snowy Owl trend

were obtained from Monopros internal reports. CVI indicator mineral data from kimberlites in the other trends were provided by Mike Seller of DeBeers Canada, along with the associated garnet and clinopyroxene grains. The contribution of the original mineral grain mounts allowed for new major-element analysis as well as laser-ablation trace-element work.

Kimberlite indicator minerals analyzed by Energy Dispersive Spectrometry (EDS), for the Darnley Bay exploration property were obtained through the GoData kimberlite indicator mineral database maintained by the NTGS. While the data quality of indicator minerals is uncertain, it is used qualitatively only for Cr-Ca diagrams for garnet classification and for T-P estimates using clinopyroxene.

### **2.3 Sample Preparation**

Peridotite xenoliths were removed from core using a combination of a MK660 saw, Isomet slow speed saw, and a hammer. All sawn edges were abraded with silicon carbide paper to remove saw marks and possible contamination or Rhenium and Osmium. Fragments of xenolith were isolated and sent to Vancouver Petrographics for thin sectioning. After being rinsed, coarse crush was obtained by isolating small volumes of xenolith in plastic that were then broken with a hammer, taking care to remove any residual kimberlite material, altered rims and vein fillings. Further crushing produced fine crush that allowed for mineral separation where applicable. Small volumes of the fine crush were then

powdered in an alumina ball mill or by hand in an agate mortar and pestle. Subsequent mineral separates were hand-picked and rinsed before being mounted or used for isotope chemistry. Grain mounts were made in-house.

## **2.4 Analytical methods and standards**

### ***2.4.1 Electron Microprobe***

Major-element mineral analysis was performed at the University of Alberta using a CAMECA SX100 electron microprobe and a JEOL 8900R electron microprobe, on both thin sections and mineral mounts. Wavelength dispersive spectroscopy (WDS) was employed operating at 20kV accelerating voltage, 20 nA probe current and 3 micron beam diameter. Standards used for calibration are listed in Appendix A2. Data reduction was performed using  $\Phi(rZ)$  correction (Armstrong, 1995) along side lower limit of detection filters following the method of Potts (1992). Counting times are provided in Appendix A2. Multiple spots on larger grains confirmed heterogeneity minerals.

### ***2.4.2 X-ray Fluorescence***

Whole-rock major-element analyses using X-ray Fluorescence (XRF) was conducted at Franklin Marshall College, using 2.5g aliquots of homogenized powdered sample and following the technique of Boyd and Mertzman (1987). Samples with more than 10g of powder were prioritized in order to complete both XRF and isotope dilution chemistry and ensure an integrated dataset.

#### **2.4.3 Re-Os Analytical Methods**

All platinum group elements (PGE) abundances and isotopic compositions were determined using isotope dilution techniques modified after Pearson & Woodland (2000). Approximately 1g of whole rock powder was digested, along with a mixed PGE spike, with inverse aqua regia (iAR: 2.5mL HCl:5mL HNO<sub>3</sub>) for 16 hours at 290°C and approximately 130bars in a high pressure ash (HPA, Anton Paar). Os was separated from the other PGEs using chloroform and HBr before microdistilling to purify the sample. The purified sample was then loaded onto a platinum filament using HBr, with BaOH used as an activator. Os was measured on a Thermo Triton Plus N-TIMS (negative thermal ionization mass spectrometer) at the Arctic Resources Laboratory, University of Alberta using the axial SEM in peak-hopping mode, at temperatures between 810 and 850°C. Osmium isotope compositions are corrected for mass-dependent isotope fractionation and oxygen isotope interferences. SEM yield and long-term performance of the instrument were monitored using 250pg loads of a Durham Osmium Standard (DrOsS; Luguet *et al.*, 2008) that yielded ion beams of similar size to most samples (Figure 2.1).

#### **2.4.4 PGE analysis**

PGEs were isolated through anion-exchange chromatography columns using AG1X8 resin (100-200 mesh) and the methods described by Pearson and Woodland (2000). The resulting solutions were measured on a Thermo Element XR2 ICPMS using a micro-concentric nebulizer. Solutions of 1ppb for each target

element were analyzed to measure and correct for instrument mass bias. Before each run, molecular oxide interferences from  $\text{ZrO}^+$ ,  $\text{HfO}^+$ ,  $\text{YbO}^+$  and  $\text{MoO}^+$  were measured to ensure offline oxide interference corrections would be accurate. Solutions of 1 ppb concentration of PGEs were made using 0.8N  $\text{HNO}_3$  except for Pd where 1N HCl was employed to more efficiently retain Pd in solution. Results were corrected for background and molecular oxide intake before isotope dilution calculations were performed.

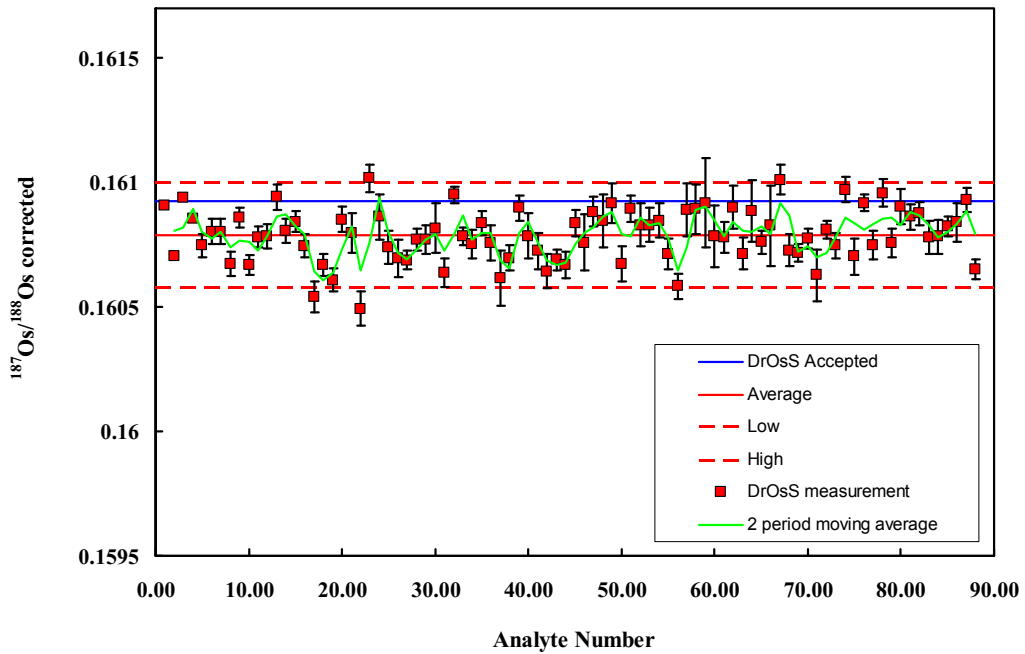


Figure 2.1 Tracking of DrOsS secondary standard used for instrument calibration over the course of this study.

#### ***2.4.5 Trace-element determinations***

Trace-element concentrations were determined for garnet and olivine by LA-ICPMS at the Arctic Resources Laboratory, University of Alberta, using a Resonetics Resolution LR50 193nm laser coupled to an Element 2XR ICPMS.

Spot sizes of 75 $\mu\text{m}$  were ablated at 10Hz repetition for 60 seconds with a laser energy of 120mJ and 11.4% attenuation. Concentrations were calculated with reference to the NIST612 glass standard using the Iolite data reduction program. The results for secondary standards (BIR-1G standard, and natural garnet megacrysts PN1, PN2) are presented in Appendix A2. For internal standardization, garnet trace element concentrations are normalized to calcium for REEs and silica for transition metals (Ni, Ti). Olivine trace element concentrations are normalized to Si.

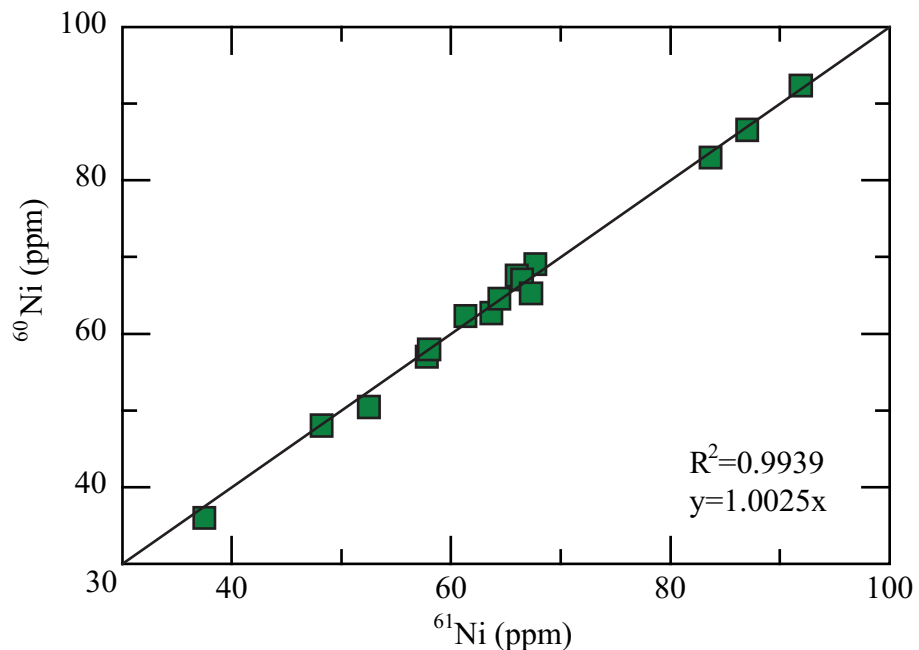


Figure 2.2 Comparison of measured  $^{61}\text{Ni}$  to  $^{60}\text{Ni}$  (ppm) using the Resonetics Resolution LR50 193nm laser coupled to an Element 2XR ICPMS compared to a 1:1 line.

## 2.5 Thermobarometry

The Nimis and Taylor (2000) single clinopyroxene method for estimating pressure and temperature is constrained by the compositional screening as defined by Grutter *et al.* (2009), and Ramsay & Tompkins (1994). P-T calculations were made using the PTEXL program developed by Thomas Köhler and updated by Thomas Stachel. Only grains proven to be stoichiometric were used for calculations. Grains deemed not from garnet peridotites or that failed to produce both pressure and temperature were omitted from further consideration.

Temperatures were also calculated using the Ni-in-garnet geothermometer, as calculated experimentally by Canil (1999). The 3000ppm Ni in olivine traditionally assumed in the temperature calculations is replaced by Ni measured from olivine in the same xenolith, where possible.

# CHAPTER 3: Results

## 3.1 Petrography

### 3.1.1 Central Victoria Island peridotites

Following the classification scheme for olivine-bearing xenoliths defined by Harte (1977), CVI peridotites are garnet lherzolites with coarse-grained olivines and an equant texture. Grain boundaries tend to be irregular to smoothly curved. In garnet-bearing samples, smaller pyrope garnets commonly occur in clusters or in somewhat linear arrays <12mm in length.

Petrographically, mantle xenoliths from central Victoria Island can be separated into two groups, group I and group II. Group I xenoliths display intense serpentinization: garnet is the only mineral to escape complete replacement. While serpentinized minerals are indistinguishable chemically, primary grain boundaries are highlighted by dark serpentine veining. Garnets are variable in size (<1-5mm, AVG = 1mm) and colour (dark red to light pink to medium purple). They display kelyphite rims (Figure 3.1B) and are mostly round: rarely do they display more irregular shapes. Grain boundaries tend to be irregular to smoothly curved. In garnet-bearing samples, smaller pyrope garnets commonly occur in clusters or in somewhat linear arrays <12mm in length. Secondary chromites, associated with recrystallization of the kelyphite alteration rims, are equant, euhedral, fine-grained (1-200 µm), and magnesium-rich.

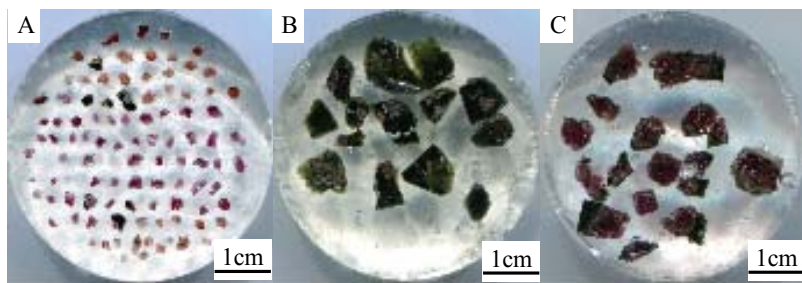


Figure 3.1 Garnet grain fragments in epoxy mounts. A: garnets display a range of colours from dark red to medium purple. B: rounded garnets with kelyphite rims in serpentinite. C: Average garnet grain size in xenoliths, unfragmented.

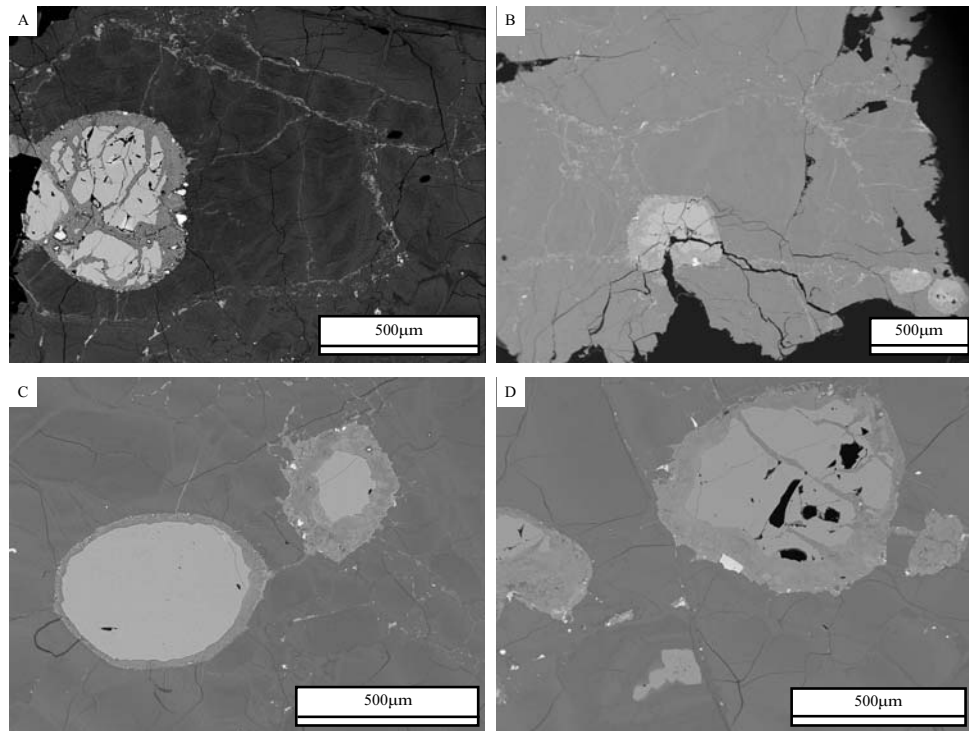


Figure 3.2 BSE images of garnet morphology for peridotite sample SnO-1. Pervasive serpentinization, kelyphite rims and equant euhedral chromites present in all images. Images A&B show alteration delineating primary grain boundaries. Garnet- light grey, chromites-bright white, darker grey-serpentine.

Group II xenoliths show more complex alteration, accounting for 16% of all CVI samples (n=6). Group II peridotites contain rare grains of fresh olivine: relics of larger grains were found and recovered for analysis, typically <100 µm in size. The pyroxenes have been extensively altered but parts of some grains still display primary grain boundaries and interference colours that distinguish them from olivine. Orthopyroxenes retain cleavage and exhibit strain, manifest as undulose extinction and deformation of cleavage. Garnets are on average larger than those of Group I (1-5mm, AVG=2mm) and are typically light pink to medium purple. Spinel are dark red-brown in colour, with straight grain boundaries, that are intergrown with olivine and orthopyroxenes, sometimes as inclusions. One sample, SnO-14, contains large, primary phlogopites that are irregular and commonly associated with spinels.

### ***3.1.2 Parry Peninsula peridotites***

The PP peridotites are fresh, coarse-equant lherzolites with curving, granoblastic grain boundaries. Strain is visible in thin section as undulose extinction and sub-grain formation. Strain is generally proportional to the degree of alteration. Spinel symplectite textures are present in association with orthopyroxene (Figure 3.3C).

Olivines from PP peridotites are coarse (0.5-10mm), exceptionally fresh, with vitreous surfaces, and range from light green to colourless. Some olivines contain inclusions of chromite. Alteration at grain boundaries occasionally results in a dirty appearance of the mineral when separated from the rock. The majority of

samples are slightly altered along fractures in the olivine, with smaller samples being more altered, displaying serpentine veins .

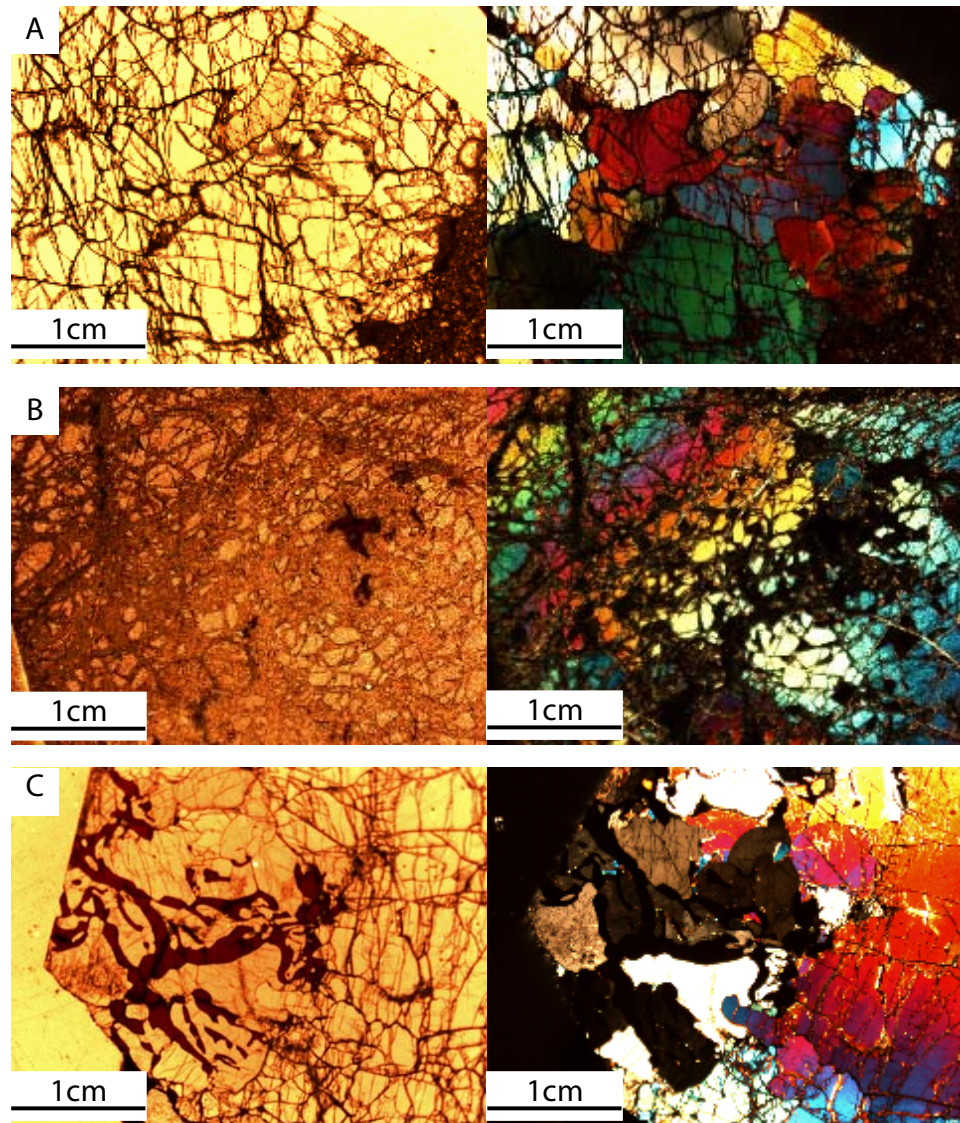


Figure 3.3 Parry Peninsula peridotite textures in plain polarized light (left) and crossed polars (right). A: fresh, coarse fractured olivine. B: altered olivine, original grain boundaries visible. C: large spinel symplectite texture with orthopyroxene



Figure 3.4 Parry Peninsula peridotite xenolith fragments showing fresh surfaces of olivine

Orthopyroxenes are tabular, light brown and on average 1mm in size. In thin section they display minor clinopyroxene exsolution. Clinopyroxenes (Cr-diopside), a minor phase in the peridotites, are irregular and can be found at grain boundaries (0.5-2mm) between olivine and orthopyroxene. They are typically found in association with irregular aluminous spinel grains (up to 1.5mm), that also display irregular grain shapes.

One PP peridotite has a 5-phase assemblage containing both garnet and spinel (Figure 3.5). Spinel-rich symplectites, likely replacing garnet, are visible in BSE in small zones (on average <1mm, with the exception of DB9B:75mm; Figure 3.3C).

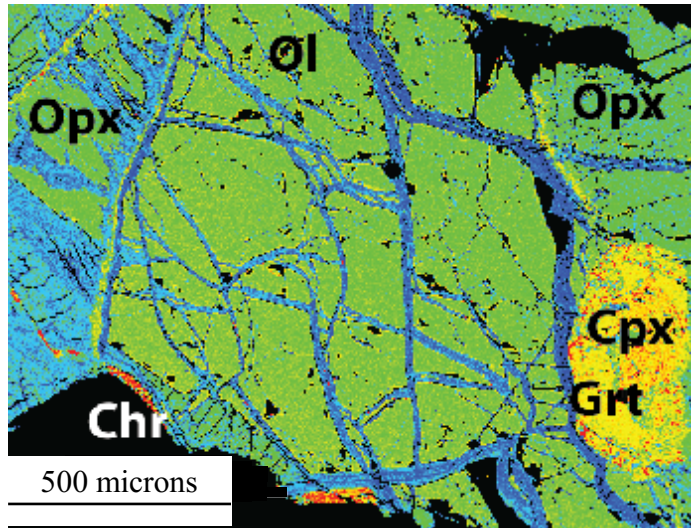


Figure 3.5 False coloured BSE images of Parry Peninsula peridotite sample DB2D displaying five phases. Garnet and clinopyroxene are not in equilibrium with each other. ol=olivine, opx=orthopyroxene, grt=garnet cpx=clinopyroxene, chr=chromite.

### 3.2 Mineral Chemistry

#### 3.2.1 Xenoliths

*Olivine:* Olivines from PP peridotites (Table 3.1) range in magnesium number ( $\text{MG\#} = [\text{Mg}/(\text{Mg}+\text{Fe})] * 100$ ) from 91.9 to 92.6 with a mean of  $92.2 \pm 0.22$  and median of 92.2 (Table 3.1; Figure 3.6). The CVI samples containing relic olivine display a range of MG# from 91.7 to 92.4 (mean= $91.9 \pm 0.27$ , median=91.9). The olivine compositions from both localities are comparable to the published olivine MG#s obtained from Archean peridotites of the central Slave craton (88-93, Kopylova *et al.*, 1999) and Kaapvaal craton ( $92.5 \pm 1.3$ , Pearson & Wittig, 2008). The modes in MG# are higher than those reported for the South African off-

craton peridotites from South African circum-cratonic Paleoproterozoic peridotite xenoliths ( $91.4 \pm 1.1$ , Janney *et al.*, 2010).

CaO contents for PP olivines (Table 3.1) range from below detection limit to 0.026 wt% (Figure 3.7), CVI olivines have higher CaO values, ranging from below detection limit to 0.07wt%. The NiO contents are relatively homogeneous for both suites (0.32-0.44 wt%, median=0.38wt%) and agree well with previously reported values for Slave craton olivines (0.39wt%; Kopylova *et al.*, 1999).

*Clinopyroxene:* Fresh Cr-diopsides are found only in the PP peridotites. They have a small compositional range with exceptionally high MG#s (95.4-96.2) with low TiO<sub>2</sub> (<0.03wt%) and NiO contents (up to 0.06 wt%). While the low TiO<sub>2</sub> concentrations are consistent with values reported for the Slave craton the MG#s are much higher (Figure 3.8).

*Orthopyroxene:* PP orthopyroxenes show similar trends in MG# (92.4-92.9) and minor oxides (TiO<sub>2</sub> up to 0.02wt%; NiO up to 0.09wt%) as the Cr-diopsides. They have low Cr<sub>2</sub>O<sub>3</sub> and CaO contents (mean=0.22wt% and median=0.27wt%, respectively). There is a relatively large range in aluminum contents across the suite (0.86 to 3.26wt% Al<sub>2</sub>O<sub>3</sub>). MG#s and Cr concentrations are consistent with previously reported contents for Slave craton orthopyroxenes, while CaO contents are lower. (Kopylova *et al.*, 1999).

Table 3.1 Major element compositions of representative grains, Parry Peninsula peridotites. Ol=olivine, Cpx=clinopyroxene, Opx=orthopyroxene, Grt=garnet, Sp=spinel

Phase Sample	Ol DB1A	Ol DB2D	Ol DB2E	Ol DB3A	Ol DB3C	Ol DB4B	Ol DB5C	Ol DB6A	Ol DB7B	Ol DB8A	Ol DB9B	Ol DB9C	Ol DB10A	Ol DB11A
<b>Major Element Oxide (wt%)</b>														
SiO <sub>2</sub>	41.25	40.98	40.63	41.15	40.93	40.48	41.15	40.54	41.69	39.51	39.92	40.82	41.35	40.70
TiO <sub>2</sub>	0.00	0.00	0.00	0.00	0.01	0.00	0.00	0.00	0.00	0.02	0.00	0.00	0.00	0.00
Al <sub>2</sub> O <sub>3</sub>	0.04	0.02	0.00	0.00	0.01	0.02	0.00	0.00	0.00	0.00	0.00	0.00	0.00	0.03
Cr <sub>2</sub> O <sub>3</sub>	0.01	0.02	0.00	0.00	0.00	0.02	0.02	0.00	0.00	0.00	0.07	0.00	0.00	0.01
V <sub>2</sub> O <sub>5</sub>	0.00	0.01	0.00	0.01	0.01	0.01	0.01	0.00	0.00	0.00	0.01	0.00	0.00	0.00
FeO	8.09	7.67	7.72	7.85	7.46	7.78	7.39	7.85	7.53	8.14	7.60	7.64	7.63	7.38
MnO	0.13	0.11	0.11	0.12	0.11	0.09	0.11	0.12	0.10	0.13	0.11	0.12	0.12	0.10
MgO	51.57	50.36	50.80	50.85	51.86	50.94	51.48	51.20	50.98	51.56	51.96	50.51	51.09	51.67
CaO	0.01	0.03	0.00	0.00	0.01	0.01	0.00	0.01	0.00	0.01	0.02	0.00	0.00	0.00
NiO	0.38	0.39	0.39	0.38	0.36	0.43	0.42	0.36	0.32	0.42	0.34	0.42	0.43	0.37
Na <sub>2</sub> O	0.00	0.01	0.00	0.00	0.00	0.00	0.01	0.00	0.00	0.00	0.00	0.00	0.00	0.00
K <sub>2</sub> O	0.00	0.00	0.00	0.00	0.00	0.00	0.00	0.00	0.00	0.00	0.01	0.00	0.00	0.01
Total	101.47	99.60	99.64	100.36	100.76	99.79	100.60	100.09	100.63	99.79	100.03	99.51	100.62	100.26
<b>Cations</b>														
Si	0.989	1.000	0.992	0.997	0.987	0.988	0.993	0.987	1.004	0.968	0.973	0.997	0.998	0.986
Ti	0.000	0.000	0.000	0.000	0.000	0.000	0.000	0.000	0.000	0.000	0.000	0.000	0.000	0.000
Al	0.001	0.001	0.000	0.000	0.000	0.001	0.000	0.000	0.000	0.000	0.000	0.000	0.000	0.001
Cr	0.000	0.000	0.000	0.000	0.000	0.000	0.000	0.000	0.000	0.000	0.001	0.000	0.000	0.000
V	0.000	0.000	0.000	0.000	0.000	0.000	0.000	0.000	0.000	0.000	0.000	0.000	0.000	0.000
Fe	0.162	0.156	0.158	0.159	0.150	0.159	0.149	0.160	0.152	0.167	0.155	0.156	0.154	0.150
Mn	0.003	0.002	0.002	0.003	0.002	0.002	0.002	0.003	0.002	0.003	0.002	0.003	0.002	0.002
Mg	1.843	1.832	1.849	1.836	1.865	1.853	1.853	1.857	1.831	1.884	1.888	1.839	1.839	1.867
Ca	0.000	0.001	0.000	0.000	0.000	0.000	0.000	0.000	0.000	0.000	0.000	0.000	0.000	0.000
Na	0.000	0.001	0.000	0.000	0.000	0.000	0.001	0.000	0.000	0.000	0.000	0.000	0.000	0.000
Ni	0.007	0.008	0.008	0.007	0.007	0.008	0.008	0.007	0.006	0.008	0.007	0.008	0.008	0.007
K	0.000	0.000	0.000	0.000	0.000	0.000	0.000	0.000	0.000	0.000	0.000	0.000	0.000	0.000
Total	3.006	3.000	3.008	3.003	3.012	3.012	3.007	3.014	2.996	3.031	3.028	3.003	3.002	3.013
<b>MG#</b>	91.9	92.1	92.1	92.0	92.5	92.1	92.5	92.1	92.4	91.9	92.4	92.2	92.3	92.6
<b>CR#</b>	22.2	44.0	-	-	2.1	46.1	84.7	100.0	-	0.0	100.0	-	0.0	12.8

Table 3.1 con't Ol=olivine, Cpx=clinopyroxene, Opx=orthopyroxene, Grt=garnet, Sp=spinel

Phase	Cpx Sample	Cpx DB1A	Cpx DB2D	Cpx DB3C	Cpx DB4B	Cpx DB5C	Cpx DB6A	Cpx DB7B	Cpx DB8A	Cpx DB9B	Cpx DB11A	Opx DB1A	Opx DB2D	Opx DB2E
<b>Major Element Oxide (wt%)</b>														
SiO <sub>2</sub>		55.69	54.40	54.58	54.33	54.10	54.40	54.72	53.65	54.33	54.37	55.68	57.84	57.07
TiO <sub>2</sub>		0.00	0.03	0.02	0.00	0.00	0.02	0.01	0.00	0.00	0.00	0.01	0.02	0.00
Al <sub>2</sub> O <sub>3</sub>		1.96	1.41	1.94	1.04	1.83	1.06	1.64	2.02	1.81	1.12	3.26	1.08	1.21
Cr <sub>2</sub> O <sub>3</sub>		0.56	0.80	0.79	0.30	0.59	0.32	0.57	0.53	0.81	0.66	0.52	0.21	0.33
V <sub>2</sub> O <sub>5</sub>		0.03	0.02	0.01	0.02	0.01	0.02	0.03	0.03	0.02	0.03	0.00	0.01	0.00
FeO		1.52	1.44	1.29	1.34	1.25	1.32	1.40	1.53	1.26	1.30	5.18	4.92	4.84
MnO		0.06	0.05	0.05	0.06	0.07	0.06	0.08	0.09	0.06	0.07	0.15	0.11	0.13
MgO		17.72	17.16	17.12	17.68	17.69	18.02	18.16	17.62	17.52	18.01	35.83	35.60	35.75
CaO		23.56	23.19	23.35	24.50	23.94	24.09	24.03	23.41	23.56	24.00	0.22	0.22	0.23
NiO		0.05	0.03	0.07	0.04	0.05	0.03	0.04	0.06	0.03	0.05	0.06	0.07	0.08
Na <sub>2</sub> O		0.66	0.71	0.83	0.29	0.48	0.29	0.41	0.72	0.69	0.45	0.02	0.01	0.00
K <sub>2</sub> O		0.00	0.00	0.01	0.01	0.00	0.00	0.01	0.01	0.00	0.01	0.00	0.00	0.00
Total		101.82	99.25	100.08	99.60	100.01	99.61	101.08	99.67	100.09	100.07	100.93	100.09	99.64
<b>Cations</b>														
Si		1.975	1.982	1.971	1.976	1.958	1.975	1.960	1.951	1.964	1.968	1.899	1.978	1.963
Ti		0.000	0.001	0.000	0.000	0.000	0.000	0.000	0.000	0.000	0.000	0.000	0.001	0.000
Al		0.082	0.061	0.082	0.045	0.078	0.045	0.069	0.086	0.077	0.048	0.131	0.044	0.049
Cr		0.016	0.023	0.023	0.009	0.017	0.009	0.016	0.015	0.023	0.019	0.014	0.006	0.009
V		0.001	0.001	0.000	0.000	0.000	0.001	0.001	0.001	0.000	0.001	0.000	0.000	0.000
Fe		0.045	0.044	0.039	0.041	0.038	0.040	0.042	0.047	0.038	0.039	0.148	0.141	0.139
Mn		0.002	0.002	0.002	0.002	0.002	0.002	0.002	0.003	0.002	0.002	0.004	0.003	0.004
Mg		0.937	0.931	0.922	0.959	0.954	0.976	0.970	0.955	0.944	0.972	1.822	1.814	1.833
Ca		0.895	0.905	0.904	0.955	0.929	0.937	0.922	0.912	0.912	0.931	0.008	0.008	0.008
Na		0.046	0.050	0.058	0.020	0.034	0.020	0.028	0.051	0.048	0.032	0.001	0.001	0.000
Ni		0.002	0.001	0.002	0.001	0.001	0.001	0.002	0.001	0.001	0.001	0.002	0.002	0.002
K		0.000	0.000	0.000	0.000	0.000	0.000	0.000	0.001	0.000	0.000	0.000	0.000	0.000
Total		3.999	4.000	4.004	4.007	4.011	4.006	4.011	4.023	4.010	4.013	4.029	3.997	4.008
<b>MG#</b>		95.4	95.5	95.9	95.9	96.2	96.1	95.9	95.4	96.1	96.1	92.5	92.8	92.9
<b>CR#</b>		16.1	27.6	21.5	16.3	17.7	16.6	18.8	15.1	23.1	28.1	9.7	11.7	15.6

Table 3.1 con't Ol=olivine, Cpx=clinopyroxene, Opx=orthopyroxene, Grt=garnet, Sp=spinel

Phase Sample	Opx DB3A	Opx DB3C	Opx DB4B	Opx DB5C	Opx DB6A	Opx DB7B	Opx DB8A	Opx DB9B	Opx DB10A	Opx DB11A	Grt DB2D
<b>Major Element Oxide (wt%)</b>											
SiO <sub>2</sub>	56.70	56.95	56.92	57.20	56.04	56.59	56.24	55.43	56.37	57.45	41.32
TiO <sub>2</sub>	0.02	0.00	0.02	0.00	0.02	0.00	0.02	0.00	0.00	0.01	0.02
Al <sub>2</sub> O <sub>3</sub>	2.24	2.07	1.59	1.73	1.49	1.77	1.95	2.25	2.19	0.86	22.60
Cr <sub>2</sub> O <sub>3</sub>	0.39	0.29	0.24	0.22	0.24	0.24	0.27	0.45	0.43	0.18	1.76
V <sub>2</sub> O <sub>5</sub>	0.01	0.00	0.01	0.01	0.02	0.04	0.01	0.02	0.01	0.01	0.01
FeO	5.06	4.91	5.10	4.84	5.13	5.21	5.18	5.03	4.92	4.90	7.98
MnO	0.12	0.14	0.12	0.14	0.16	0.14	0.13	0.15	0.15	0.14	0.54
MgO	35.49	35.53	35.58	35.84	35.94	35.57	35.97	35.78	35.04	36.03	20.45
CaO	0.19	0.34	0.18	0.18	0.20	0.24	0.23	0.41	0.70	0.21	5.34
NiO	0.07	0.07	0.07	0.08	0.07	0.03	0.10	0.05	0.09	0.07	0.00
Na <sub>2</sub> O	0.03	0.03	0.00	0.02	0.01	0.00	0.01	0.00	0.01	0.00	0.00
K <sub>2</sub> O	0.00	0.01	0.00	0.01	0.01	0.00	0.01	0.00	0.00	0.01	0.00
Total	100.30	100.34	99.85	100.28	99.32	99.84	100.11	99.56	99.91	99.86	100.02
<b>Cations</b>											
Si	1.940	1.947	1.956	1.954	1.940	1.946	1.932	1.916	1.939	1.971	2.950
Ti	0.000	0.000	0.000	0.000	0.000	0.000	0.001	0.000	0.000	0.000	0.001
Al	0.090	0.083	0.064	0.070	0.061	0.072	0.079	0.092	0.089	0.035	1.902
Cr	0.010	0.008	0.007	0.006	0.006	0.007	0.007	0.012	0.012	0.005	0.099
V	0.000	0.000	0.000	0.000	0.001	0.001	0.000	0.001	0.000	0.000	0.000
Fe	0.145	0.140	0.147	0.138	0.149	0.150	0.149	0.145	0.141	0.141	0.477
Mn	0.004	0.004	0.004	0.004	0.005	0.004	0.004	0.004	0.004	0.004	0.033
Mg	1.810	1.810	1.822	1.825	1.855	1.824	1.841	1.844	1.796	1.843	2.176
Ca	0.007	0.013	0.007	0.006	0.007	0.009	0.009	0.015	0.026	0.008	0.408
Na	0.002	0.002	0.000	0.001	0.001	0.000	0.001	0.000	0.001	0.000	0.000
Ni	0.002	0.002	0.002	0.002	0.002	0.001	0.003	0.001	0.002	0.002	0.000
K	0.000	0.000	0.000	0.000	0.000	0.000	0.000	0.000	0.000	0.001	0.000
Total	4.010	4.009	4.008	4.008	4.026	4.013	4.025	4.031	4.011	4.009	8.048
<b>MG#</b>	92.6	92.8	92.6	93.0	92.6	92.4	92.5	92.7	92.7	92.9	82.0
<b>CR#</b>	10.4	8.5	9.2	8.0	9.6	8.5	8.6	11.8	11.7	12.0	5.0

Table 3.1 con't Ol=olivine, Cpx=clinopyroxene, Opx=orthopyroxene, Grt=garnet, Sp=spinel

Phase Sample	Sp DB2D	Sp DB3C	Sp DB4B	Sp DB5C	Sp DB6A	Sp DB8A	Sp DB9B	Sp DB11A
<b>Major Element Oxide (wt%)</b>								
SiO <sub>2</sub>	0.03	0.02	0.03	0.04	0.02	0.03	0.04	0.03
TiO <sub>2</sub>	0.06	0.00	0.02	0.00	0.01	0.00	0.03	0.01
Al <sub>2</sub> O <sub>3</sub>	21.31	34.48	38.34	40.28	35.68	39.02	30.42	26.04
Cr <sub>2</sub> O <sub>3</sub>	48.43	35.72	29.73	28.65	33.42	30.28	40.52	45.04
V <sub>2</sub> O <sub>5</sub>	0.19	0.12	0.15	0.10	0.17	0.16	0.18	0.16
FeO	14.65	12.69	13.64	11.19	12.13	12.62	13.19	14.22
MnO	0.20	0.18	0.15	0.13	0.14	0.15	0.16	0.19
MgO	14.43	16.03	16.31	19.43	17.02	17.07	15.16	14.17
CaO	0.02	0.00	0.07	0.01	0.01	0.01	0.00	0.00
NiO	0.11	0.10	0.17	0.18	0.13	0.18	0.09	0.04
Na <sub>2</sub> O	0.01	0.00	0.01	0.01	0.00	0.02	0.06	0.01
K <sub>2</sub> O	0.00	0.00	0.00	0.00	0.00	0.01	0.03	0.00
Total	99.43	99.33	98.62	100.05	98.76	99.54	99.89	99.92
<b>Cations</b>								
Si	0.001	0.001	0.001	0.001	0.001	0.001	0.001	0.001
Ti	0.001	0.000	0.001	0.000	0.000	0.001	0.001	0.000
Al	0.771	1.175	0.771	1.308	1.208	1.297	1.053	0.923
Cr	1.176	0.817	1.176	0.624	0.759	0.675	0.941	1.071
V	0.005	0.003	0.005	0.002	0.004	0.004	0.004	0.004
Fe <sup>3+</sup>	0.044	0.004	0.044	0.064	0.027	0.024	0.002	0.000
Fe <sup>2+</sup>	0.332	0.303	0.332	0.194	0.264	0.273	0.322	0.358
Mn	0.005	0.004	0.005	0.003	0.003	0.004	0.004	0.005
Mg	0.661	0.691	0.661	0.798	0.729	0.718	0.664	0.636
Ca	0.001	0.000	0.001	0.000	0.000	0.000	0.000	0.000
Ni	0.003	0.002	0.003	0.004	0.003	0.004	0.002	0.001
Na	0.001	0.000	0.001	0.001	0.000	0.001	0.003	0.001
K	0.000	0.000	0.000	0.000	0.000	0.000	0.001	0.000
Total	3.000	3.000	3.000	3.000	3.000	3.000	3.000	3.000
MG#	63.7	69.3	68.1	75.6	71.4	70.7	67.2	64.0
CR#	60.4	41.0	34.2	32.3	38.6	34.2	47.2	53.7

Table 3.2 Major element compositions of representative grains, central Victoria Island peridotites. Grt= garnet, Ol=olivine, Sp= spinel

Phase Sample	Grt SnO-1	Grt SnO-5	Grt SnO-11	Grt SnO-12	Grt SnO-15	Grt SnO-17	Grt SnO-19	Grt SnO-20	Grt SnO-23	Grt SnO-24	Grt SnO-26	Grt SnO-27	Grt SnO-28	Grt SnO-29
<b>Major Element Oxide (wt%)</b>														
SiO <sub>2</sub>	41.34	41.15	40.85	41.03	41.67	41.45	41.84	41.79	41.27	41.25	41.27	41.17	41.84	41.36
TiO <sub>2</sub>	0.17	0.03	0.04	0.47	0.00	0.03	0.37	0.37	0.53	0.11	0.04	0.04	0.42	0.06
Al <sub>2</sub> O <sub>3</sub>	16.86	20.82	15.91	18.27	19.18	18.82	21.43	21.37	16.44	17.29	16.27	16.24	19.78	19.57
Cr <sub>2</sub> O <sub>3</sub>	8.58	4.26	9.32	5.87	5.41	5.75	2.15	2.17	8.41	7.94	8.73	8.96	4.23	4.77
V <sub>2</sub> O <sub>3</sub>	0.07	0.05	0.00	0.00	0.00	0.00	0.00	0.00	0.00	0.00	0.06	0.00	0.00	0.00
FeO	6.77	8.62	7.41	9.19	7.83	7.48	8.72	8.55	7.49	7.43	6.95	6.83	8.24	7.71
MnO	0.33	0.54	0.40	0.45	0.37	0.36	0.37	0.38	0.35	0.37	0.33	0.30	0.38	0.39
MgO	20.28	19.27	18.38	17.87	19.89	19.99	20.58	20.17	19.18	19.44	18.90	19.13	20.29	20.12
CaO	6.27	5.42	7.02	6.14	5.45	5.53	4.12	4.14	6.44	6.13	6.81	6.92	4.71	5.17
NiO	0.01	0.00	0.00	0.00	0.00	0.00	0.00	0.00	0.00	0.00	0.00	0.06	0.00	0.00
Na <sub>2</sub> O	0.02	0.02	0.00	0.07	0.00	0.00	0.09	0.08	0.05	0.04	0.00	0.00	0.05	0.03
K <sub>2</sub> O	0.01	0.01	0.00	0.00	0.00	0.00	0.00	0.00	0.00	0.00	0.00	0.00	0.00	0.00
Total	100.71	100.17	99.32	99.36	99.80	99.42	99.67	99.02	100.15	100.00	99.36	99.65	99.94	99.18
<b>Cations</b>														
Si	2.989	2.966	3.019	3.014	3.012	3.009	2.998	3.011	3.011	3.004	3.031	3.018	3.009	3.001
Ti	0.009	0.001	0.002	0.026	0.000	0.002	0.020	0.020	0.029	0.006	0.002	0.002	0.023	0.003
Al	1.437	1.768	1.386	1.582	1.634	1.610	1.810	1.815	1.414	1.484	1.408	1.403	1.677	1.674
Cr	0.490	0.243	0.544	0.341	0.309	0.330	0.122	0.124	0.485	0.457	0.507	0.519	0.240	0.274
V	0.003	0.002	0.000	0.000	0.000	0.000	0.000	0.000	0.000	0.000	0.003	0.000	0.000	0.000
Fe	0.409	0.520	0.458	0.565	0.473	0.454	0.523	0.515	0.457	0.453	0.427	0.419	0.496	0.468
Mn	0.020	0.033	0.025	0.028	0.023	0.022	0.023	0.023	0.022	0.023	0.021	0.019	0.023	0.024
Mg	2.186	2.070	2.025	1.957	2.143	2.163	2.198	2.166	2.086	2.111	2.069	2.091	2.175	2.176
Ca	0.486	0.419	0.556	0.483	0.422	0.430	0.316	0.320	0.503	0.478	0.536	0.544	0.363	0.402
Ni	0.001	0.000	0.000	0.000	0.000	0.000	0.000	0.000	0.000	0.000	0.000	0.004	0.000	0.000
Na	0.003	0.002	0.000	0.010	0.000	0.000	0.012	0.011	0.007	0.005	0.000	0.000	0.007	0.005
K	0.001	0.001	0.000	0.000	0.000	0.000	0.000	0.000	0.000	0.000	0.000	0.000	0.000	0.000
Total	8.034	8.024	8.014	8.004	8.016	8.020	8.022	8.005	8.014	8.021	8.004	8.018	8.013	8.025
MG#	84.2	79.9	81.6	77.6	81.9	82.6	80.8	80.8	82.0	82.3	82.9	83.3	81.4	82.3
CR#	25.4	12.1	28.2	17.7	15.9	17.0	6.3	6.4	25.5	23.6	26.5	27.0	12.5	14.1

Table 3.2 con't Grt= garnet, Ol=olivine, Sp= spinel

Phase Sample	Grt SnO-32	Grt SnO-33	Grt SnO-34	Grt SnO-35	Ol SnO-12	Ol SnO-24	Ol SnO-32	Ol SnO-33	Ol SnO-36	Phase Sample	Sp SnO-1	Sp SnO-5
<b>Major Element Oxide (wt%)</b>												
SiO <sub>2</sub>	41.46	41.50	41.85	42.06	40.61	40.93	40.85	40.86	40.72	SiO <sub>2</sub>	0.15	0.03
TiO <sub>2</sub>	0.00	0.27	0.15	0.64	0.00	0.04	0.00	0.00	0.00	TiO <sub>2</sub>	0.76	0.11
Al <sub>2</sub> O <sub>3</sub>	17.80	17.09	19.65	19.92	0.00	0.00	0.00	0.00	0.00	Al <sub>2</sub> O <sub>3</sub>	30.51	9.52
Cr <sub>2</sub> O <sub>3</sub>	7.54	7.39	5.03	3.49	0.05	0.00	0.04	0.03	0.00	Cr <sub>2</sub> O <sub>3</sub>	35.48	59.05
V <sub>2</sub> O <sub>5</sub>	0.00	0.00	0.00	0.04	0.00	0.00	0.00	0.00	0.00	V <sub>2</sub> O <sub>5</sub>	0.17	0.31
FeO	7.13	6.75	7.34	8.02	7.99	8.17	7.87	8.00	7.43	FeO	14.35	19.08
MnO	0.36	0.30	0.36	0.35	0.12	0.10	0.09	0.11	0.11	MnO	0.16	0.30
MgO	19.76	20.20	20.43	20.35	50.77	50.33	50.41	50.38	50.61	MgO	17.36	10.25
CaO	5.94	6.09	5.04	4.92	0.07	0.00	0.05	0.05	0.00	CaO	0.00	0.01
NiO	0.00	0.00	0.00	0.00	0.42	0.42	0.44	0.38	0.35	NiO	0.23	0.03
Na <sub>2</sub> O	0.00	0.00	0.04	0.05	0.00	0.00	0.00	0.00	0.00	Na <sub>2</sub> O	0.01	0.01
K <sub>2</sub> O	0.00	0.00	0.00	0.00	0.00	0.00	0.00	0.00	0.00	K <sub>2</sub> O	0.04	0.01
Total	99.99	99.59	99.89	99.84	100.02	99.99	99.75	99.82	99.22	Total	99.22	98.72
<b>Cations</b>												
Si	3.008	3.020	3.008	3.019	0.990	0.997	0.997	0.997	0.996	Si	0.004	0.001
Ti	0.000	0.015	0.008	0.034	0.000	0.001	0.000	0.000	0.000	Ti	0.017	0.003
Al	1.522	1.466	1.665	1.685	0.000	0.000	0.000	0.000	0.000	Al	1.046	0.375
Cr	0.432	0.425	0.286	0.198	0.001	0.000	0.001	0.001	0.000	Cr	0.816	1.559
V	0.000	0.000	0.000	0.002	0.000	0.000	0.000	0.000	0.000	V	0.004	0.008
Fe	0.433	0.411	0.441	0.481	0.163	0.166	0.161	0.163	0.152	Fe <sup>3+</sup>	0.094	0.051
Mn	0.022	0.019	0.022	0.021	0.002	0.002	0.002	0.002	0.002	Fe <sup>2+</sup>	0.255	0.482
Mg	2.137	2.191	2.189	2.178	1.844	1.828	1.833	1.832	1.846	Mn	0.004	0.008
Ca	0.462	0.475	0.388	0.378	0.002	0.000	0.001	0.001	0.000	Mg	0.753	0.511
Ni	0.000	0.000	0.000	0.000	0.008	0.008	0.009	0.007	0.007	Ca	0.000	0.000
Na	0.000	0.000	0.006	0.007	0.000	0.000	0.000	0.000	0.000	Ni	0.005	0.001
K	0.000	0.000	0.000	0.000	0.000	0.000	0.000	0.000	0.000	Na	0.001	0.001
Total	8.015	8.020	8.012	8.005	3.010	3.002	3.003	3.003	3.004	K	0.001	0.000
<b>MG#</b>	83.2	84.2	83.2	81.9	91.9	91.7	91.9	91.8	92.4	Total	3.00	3.00
<b>CR#</b>	22.1	22.5	14.7	10.5	100.0	-	100.0	100.0	-	<b>MG#</b>	68.3	48.9
										<b>CR#</b>	43.8	80.6

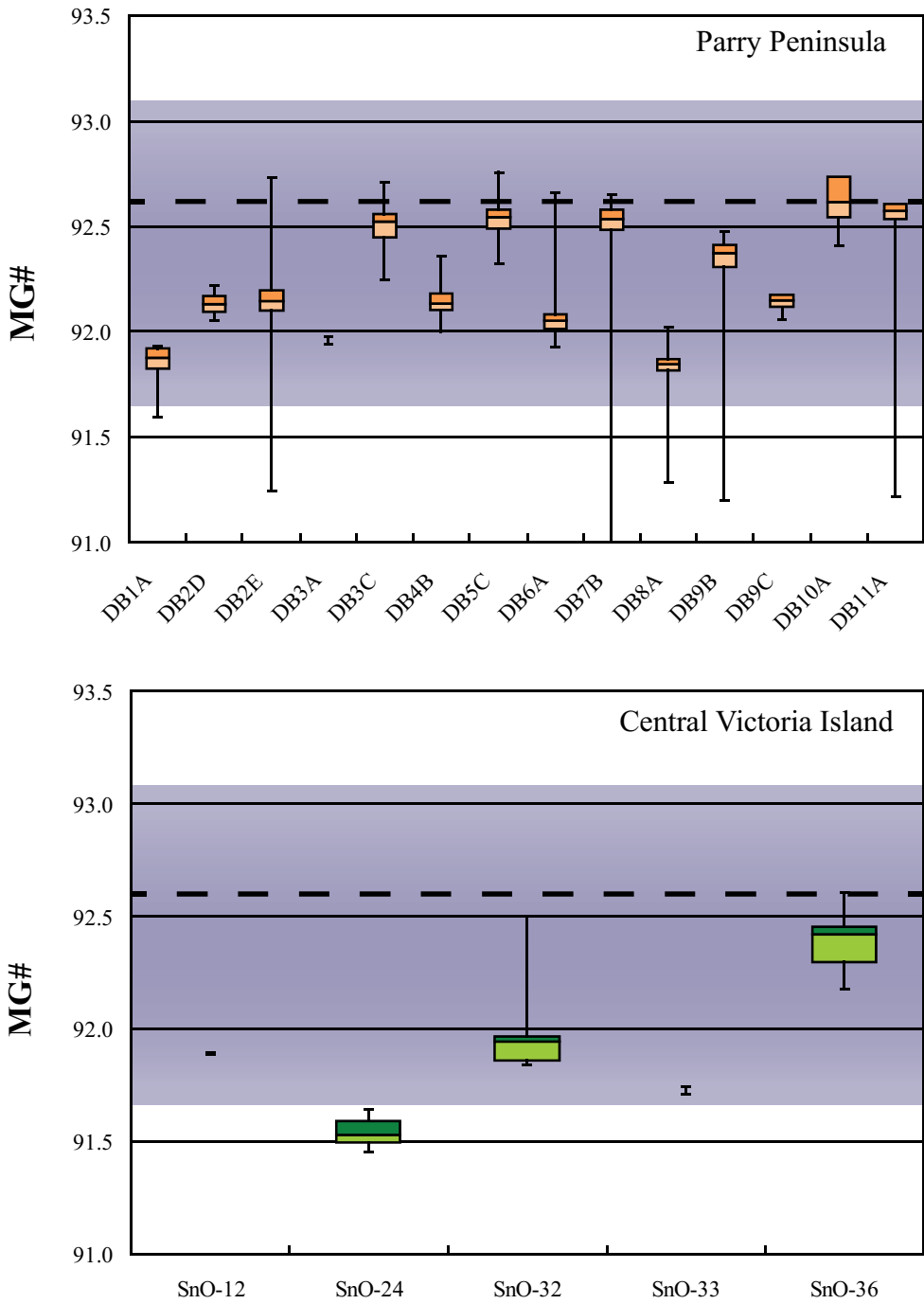


Figure 3.6 Olivine MG# for central Victoria Island and Parry Peninsula peridotite xenoliths. Boxes represent the median MG#  $\pm 25\%$  of data points using interquartile ranges. Extended lines show minimum and maximum values. The purple band is the range for global cratonic olivine MG#s and the bold dashed line for mean MG# of 92.6 from Pearson and Wittig, 2008.

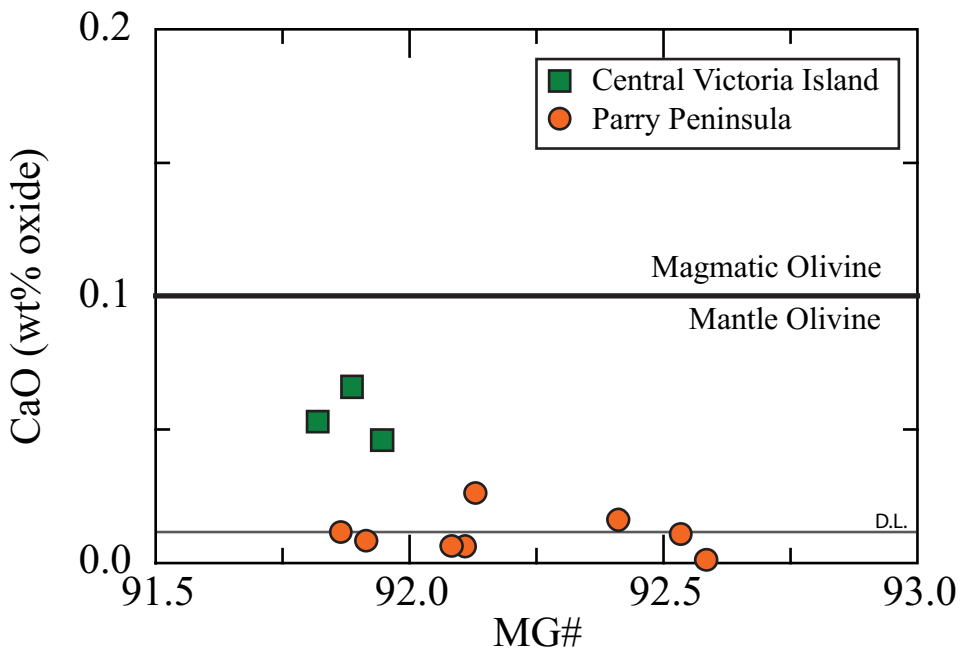


Figure 3.7 CaO (wt%) versus MG# for olivines. All samples from both suites have <0.1 wt% CaO suggesting mantle origin (Pearson and Wittig, 2014). D.L.= detection limit

*Garnet:* Garnets from the CVI xenoliths are chromium pyropes with  $\text{Cr}_2\text{O}_3$  contents of 2.15 to 9.32 wt% (mean=6.11 wt%, median=5.81 wt%) and CaO contents between 4.10 and 7.02 wt% (mean=5.68 wt%). Based on the criteria of Gurney (1984) and Grutter (2004), the vast majority of the garnets classify as calcic-lherzolitic and G9, respectively (Figure 3.9).  $\text{TiO}_2$  contents are variable within the suite (below detection limit to 0.64wt%, mean=0.13wt%), the MG#s are relatively high (78-84). Garnet trace-element analyses are reported in Section 3.3.

Garnets from the PP xenolith DB2B are pyropes with 1.76wt% Cr<sub>2</sub>O<sub>3</sub> and 5.34wt% CaO classifying as G9 (Grutter, 2004), or lherzolitic. A more complete garnet dataset for PP mantle garnets exists for heavy mineral till concentrate and is presented in Section 3.2.2 and Appendix A5.

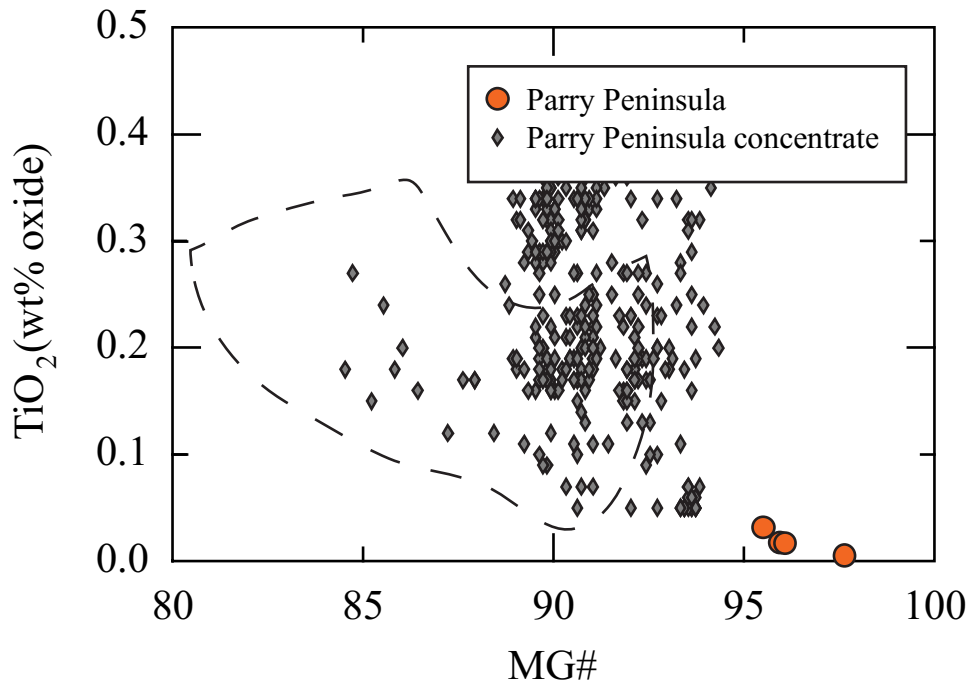


Figure 3.8 TiO<sub>2</sub> concentration versus MG# for clinopyroxene for Parry Peninsula. The dashed field is the central Slave cratonic field from Aulbach *et al.*, 2004.

Garnets from both the xenoliths and till concentrate have CaO and Cr<sub>2</sub>O<sub>3</sub> contents that are comparable to contents previously reported for cratonic garnets from the Slave craton, the Kaapvaal craton and circum-cratonic Kaapvaal sources (eg. Simon *et al.*, 2003; Gregoire *et al.*, 2003; Janney *et al.*, 2010).

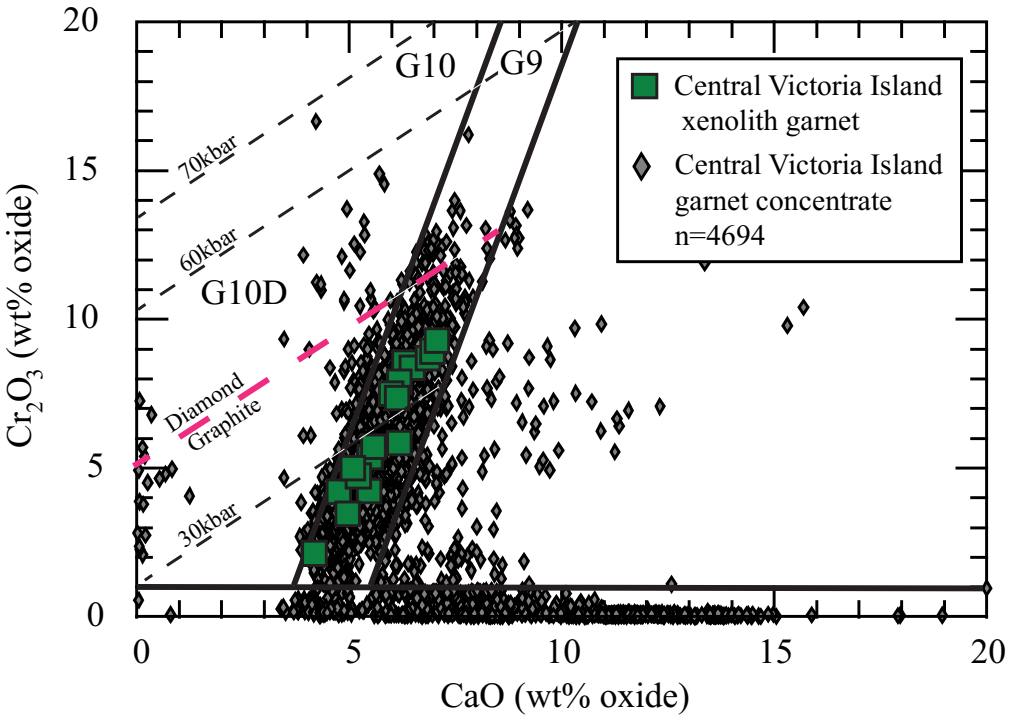


Figure 3.9. Covariance plot of CaO vs  $\text{Cr}_2\text{O}_3$  for xenolith garnets. A: Peridotitic garnets plotted with till concentrate from central Victoria Island. Fields for lherzolite (G9), harzburgite (G10) and diamond-bearing harzburgite (G10D), and isobars from Grutter *et al.* (2004). Pink dashed line is the graphite-diamond constraint. Positioning of the G10D field is constrained by MnO; low MnO can shift the diamond potential zone below the diamond-graphite transition.

*Spinel:* Two CVI peridotites were large enough to thin section and also retain material for later work. In sample SnO-1, chromites display a range of  $\text{Cr}_2\text{O}_3$  and  $\text{Al}_2\text{O}_3$  contents, 21.2 to 42.2 wt% and 22.6 to 44.1 wt%; respectively. Chromites from SnO-5 are much higher in  $\text{Cr}_2\text{O}_3$  (59.01-59.39 wt%) and lower in  $\text{Al}_2\text{O}_3$  (9.32-9.78 wt%). In both samples the spinels are euhedral and appear to be the result of alteration around garnet grains.

PP lherzolites have spinel grains that are irregular, anhedral and brown in thin section. While still chrome-rich (25.4-48.4 wt%  $\text{Cr}_2\text{O}_3$ , median=33.4 wt%) these

spinel have a high  $\text{Al}_2\text{O}_3$  content (21.31-40.28%). Spinel associated with the symplectite features are likely related to garnet breakdown.

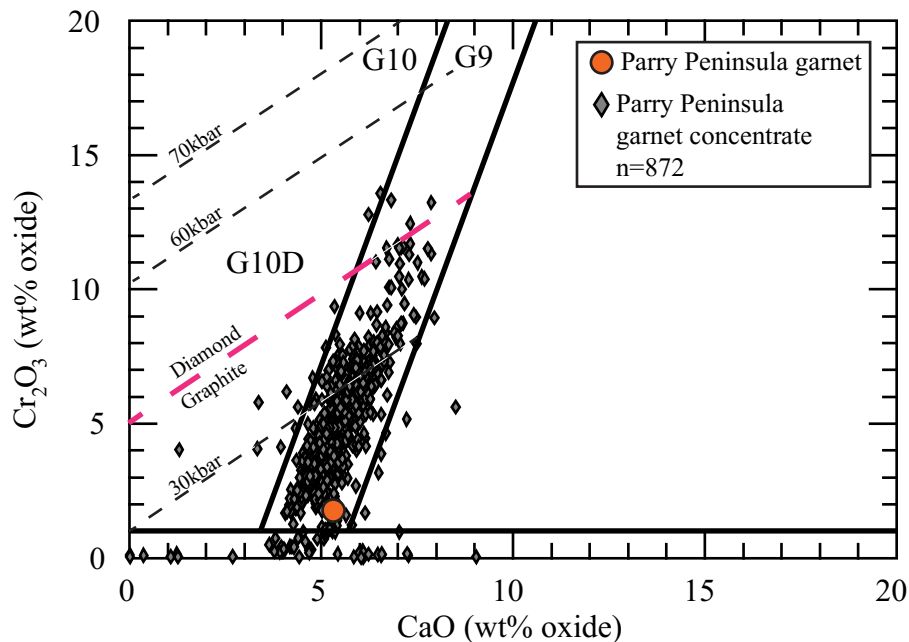


Figure 3.10 Covariance plot of  $\text{CaO}$  vs  $\text{Cr}_2\text{O}_3$  for xenolith garnets plotted with till concentrate from Parry Peninsula. Fields for lherzolite (G9), harzburgite (G10) and diamond-bearing harzburgite (G10D), and isobars from Grutter *et al.* (2004)). Pink dashed line is the graphite-diamond constraint. Positioning of the G10D field is constrained by  $\text{MnO}$ ; low  $\text{MnO}$  can shift the diamond potential zone below the diamond-graphite transition.

### 3.2.2 Concentrate Mineral Chemistry

Till mineral concentrate data acquired by EDS was provided along side mineral mounts by DeBeers Canada. Before using the EDS database, select grains were reanalyzed by WDS (Appendix A7) to check for accuracy of the EDS analyses. On average, EDS data and WDS data plot close to the 1:1 lines except for minor elements such as Na in pyroxene (Figure A7.2) which are systematically displaced to lower values in the EDS data. In general though, the close agreement

of WDS and EDS data for most major elements supports the use of the EDS data in an exploration context and for qualitative assessment with respect to the xenolith WDS data. Detailed comparisons of major element chemistry between WDS and EDS are provided in Appendix A7.

*Central Victoria Island till concentrate data*

Till concentrate data from the Snowy Owl kimberlite has been isolated from the CVI database to compare the xenolith suite from this intrusion with the associated concentrate. Snowy Owl kimberlite garnet concentrate displays a wide range of CaO contents, from 3.46 to 20 wt% with a median value of 5.48wt%. Cr<sub>2</sub>O<sub>3</sub> values are equally broad, ranging from 0.04 to 13.99 wt% (median 4.86 wt%). Lherzolitic compositions account for 82% of the data, only 0.9% of the garnets are harzburgitic (G10). Four grains (0.002% of the population) are classified as G10D, indicating a mantle with limited possible diamond potential.

The garnet concentrate data from till across the central Victoria Island kimberlite field mirrors this trend with regard to the peridotitic component (86%; 95% lherzolite to 5% harzburgite), but carries a strong eclogitic signature that accounts for 14% of the total grains. The greater eclogitic component may suggest that the different structural kimberlite trends (Snowy Owl, Blue Ice, Galaxy and King Eider) sample different mantle sources.

*Parry Peninsula till concentrate data*

Garnet till concentrate (n=872) from PP has a mean Cr<sub>2</sub>O<sub>3</sub> content of 4.66 wt% and a median of 4.37 wt%. Variation in CaO (0.37-9.04 wt%) relates to a mean value of 5.38 wt% and median of 5.37wt%. The concentrate data indicate a mantle lithosphere composition that is dominantly peridotitic (97% peridotite to 3% eclogite), with “lherzolitic” G9 garnets being the predominant garnet type. Garnets classified as G10D garnets account for significantly less than 1% of the dataset, with only 2 grains barely projecting into this compositional field.

Clinopyroxenes from till concentrate (n=524) have lower MG#s than the xenoliths (82-94) and much higher TiO<sub>2</sub> concentrations (0.01-0.42wt%, median and mean=0.21wt%). They appear broadly more cratonic in composition, resembling Slave craton clinopyroxene (Figure 3.8).

### **3.3 Garnet Trace-Element Chemistry**

#### ***3.3.1 Xenoliths***

Peridotitic garnets from central Victoria Island display high Ni contents (38-162ppm, median=65ppm) with more than 75% of the data clustering between 50-70ppm. In terms of REE, they display four distinct trace-element patterns (Figure 3.11). Type I garnets have very low LREE concentrations that increase to chondritic abundances through the MREEs, becoming ~10x chondritic in the HREEs. This pattern is typical for lherzolitic garnets (eg. Stachel et. al., 1998; Pearson *et al.*, 2003) and is accompanied by high Lu/Hf ((Lu/Hf)<sub>N</sub> up to 3, mean

2.25). Type II garnets have variable LREE abundances that are near chondritic, with decreasing concentrations from Nd to Tb but increasing to the HREE with chondritic concentrations towards Lu. Type IIIa garnets display a sinusoidal trend, with a peak within LREE around Sm and lower MREE and a minimum at Er. Such sinusoidal patterns are characterized as harzburgitic (eg. Shimizu & Richardson, 1987, Stachel *et al.*, 1998). ( $\text{Lu}/\text{Hf}$ )<sub>N</sub> in this groups can be <1 and have very low Hf concentrations. Type IIIb garnets have LREE patterns similar to Type IIIa in their marked increase from La to Nd and a negative slope of MREE, but the peak between Pr and Sm is not as pronounced as the Type II garnets. These REE patterns are exclusive to cratonic garnets (eg. Stachel et. al., 1998, Simon et. al. 2003).

### **3.3.2 Garnet Concentrate**

Trace-element concentrations were determined for 50 garnet concentrate grains from central Victoria Island kimberlites (Appendix A5). The Ni concentrations in the concentrate garnets are typically lower than those determined for the xenolith garnets (12-87 ppm, median=45 ppm). Using the same trace element pattern classification developed for the xenolith garnets, there is a strong bias towards the Iherzolitic, Type I garnet REE trend, accounting for 74% of the data. High ( $\text{Lu}/\text{Hf}$ )<sub>N</sub> ratios are recorded in the Type I garnet concentrate. Type IIIb garnet patterns (16%) are more common than both Type IIIa (8%) and Type II (2%).

Table 3.3 Garnet trace elements for central Victoria Island garnets. All measurements are in ppb. Ratios are normalized to chondrite using the values of McDonough and Sun (1995).

	<b>SnO-11</b>	<b>SnO-12</b>	<b>SnO-15</b>	<b>SnO-17</b>	<b>SnO-19</b>	<b>SnO-20</b>	<b>SnO-23</b>	<b>SnO-24</b>	<b>SnO-26</b>	<b>SnO-28</b>	<b>SnO-29</b>	<b>SnO-32</b>	<b>SnO-33</b>	<b>SnO-34</b>	<b>SnO-35</b>
<b>Ti</b>	240	1605	159	165	2492	2287	3387	555	301	2041	320	141	987	847	1181
<b>Ni60</b>	57.00	36.00	62.68	69.10	50.44	48.01	86.57	62.28	92.30	67.56	57.96	67.04	65.27	64.57	82.95
<b>Ni61</b>	57.80	37.50	63.70	67.70	52.50	48.20	87.00	61.30	91.90	66.00	58.00	66.50	67.30	64.40	83.70
<b>Sr</b>	1.19	0.65	0.03	0.43	0.15	0.20	0.96	0.39	0.10	0.36	0.28	0.22	0.18	0.18	0.49
<b>Y</b>	1.40	11.93	1.38	1.47	16.93	16.33	1.95	1.59	0.94	5.58	2.97	0.34	8.81	7.34	5.53
<b>Zr</b>	26.50	46.84	1.50	3.74	22.14	22.10	44.10	10.16	0.09	14.57	9.64	0.23	9.83	8.46	12.51
<b>Nb</b>	1.09	0.48	0.50	0.69	0.13	0.15	0.53	0.79	0.54	0.37	0.19	0.33	0.70	0.47	0.42
<b>Ba</b>	0.00	0.00	0.00	0.00	0.00	0.09	0.00	0.00	0.00	0.00	0.00	0.07	0.00	0.00	0.00
<b>La</b>	0.15	0.06	0.07	0.08	0.01	0.08	0.07	0.12	0.19	0.03	0.02	0.20	0.07	0.06	0.05
<b>Ce</b>	1.54	0.79	0.25	0.76	0.10	0.19	0.92	0.89	0.60	0.31	0.33	0.63	0.58	0.52	0.59
<b>Pr</b>	0.48	0.26	0.03	0.22	0.03	0.03	0.29	0.20	0.05	0.11	0.15	0.05	0.13	0.12	0.20
<b>Nd</b>	4.32	2.54	0.17	1.60	0.25	0.29	2.69	1.41	0.08	0.94	1.45	0.12	0.79	0.72	1.70
<b>Sm</b>	2.26	1.76	0.04	0.42	0.39	0.39	1.19	0.68	0.00	0.67	0.61	0.01	0.35	0.32	0.43
<b>Eu</b>	0.66	0.76	0.01	0.09	0.23	0.24	0.41	0.24	0.00	0.23	0.18	0.00	0.17	0.15	0.12
<b>Gd</b>	1.53	2.48	0.05	0.20	1.23	1.22	0.98	0.67	0.01	0.93	0.47	0.01	0.79	0.63	0.39
<b>Tb</b>	0.12	0.36	0.01	0.02	0.30	0.29	0.11	0.08	0.00	0.15	0.05	0.00	0.17	0.15	0.07
<b>Dy</b>	0.41	2.29	0.13	0.16	2.71	2.55	0.56	0.37	0.07	0.96	0.41	0.03	1.37	1.19	0.74
<b>Ho</b>	0.05	0.45	0.05	0.05	0.63	0.62	0.08	0.06	0.03	0.20	0.10	0.01	0.33	0.29	0.20
<b>Er</b>	0.13	1.25	0.22	0.23	2.14	1.96	0.18	0.17	0.15	0.69	0.41	0.04	1.06	0.95	0.74
<b>Tm</b>	0.02	0.17	0.04	0.05	0.30	0.29	0.03	0.02	0.03	0.11	0.07	0.01	0.16	0.15	0.13
<b>Yb</b>	0.21	1.26	0.44	0.51	2.31	2.14	0.32	0.24	0.38	0.89	0.63	0.14	1.29	1.09	1.09
<b>Lu</b>	0.05	0.18	0.08	0.09	0.34	0.29	0.07	0.06	0.08	0.16	0.12	0.03	0.21	0.18	0.18
<b>Hf</b>	0.68	1.05	0.04	0.09	0.47	0.50	0.85	0.23	0.00	0.31	0.20	0.00	0.28	0.25	0.25
<b>La/Yb</b>	0.47	0.03	0.11	0.11	0.00	0.03	0.16	0.33	0.33	0.02	0.02	0.93	0.04	0.04	0.03
<b>Lu/Hf</b>	0.29	0.72	8.59	3.95	2.98	2.43	0.33	1.01	-	2.13	2.46	26.81	3.04	2.99	2.96

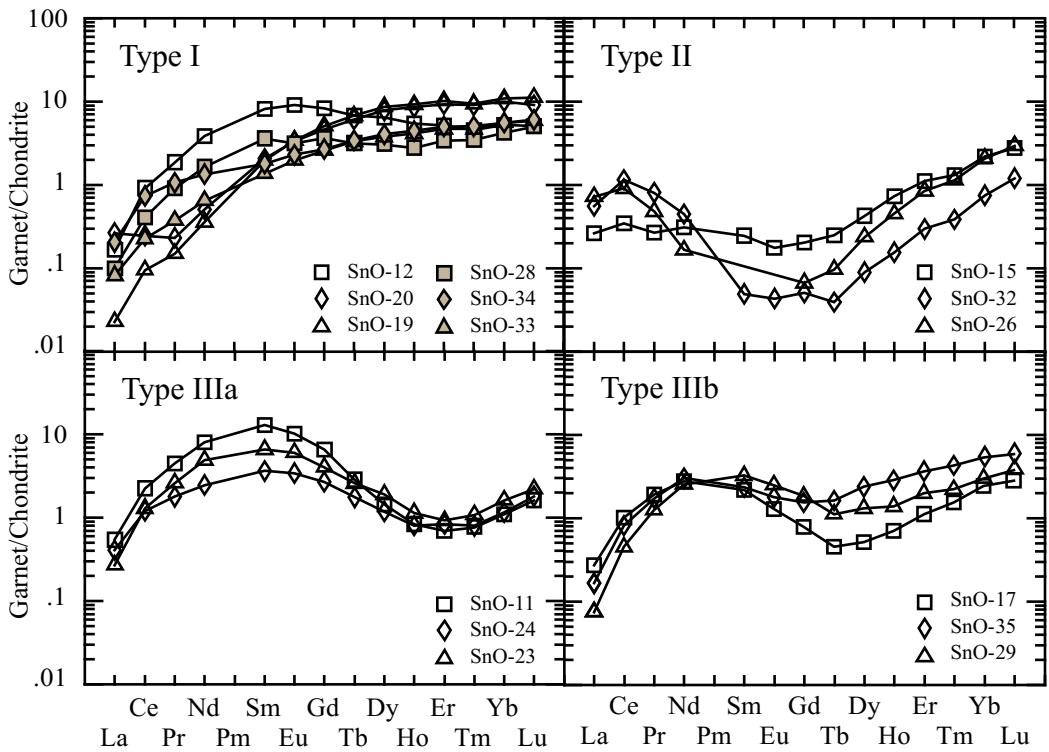


Figure 3.11 Chondrite-normalized rare earth element plots for garnets from Central Victoria Island peridotite xenoliths. Chondrite normalization values after McDonough and Sun, 1995. Type I lherzolitic, Type II depleted with LREE enrichment, Type III harzburgitic with variable re-enrichment.

### 3.4 Thermobarometry

#### 3.4.1 Ni-in-garnet thermometer

Nickel-in-garnet temperatures calculated using the methods of Canil (1999) and a median olivine Ni concentration of 3418 ppm was used for samples without relic olivine (Table 3.4). Multiple analyses on single garnet grains yielded identical  $T_{Ni}$  with a maximum of 40°C difference. Ni concentrations for garnet in peridotite xenoliths ranged from 45 to 95 ppm (median 65 ppm) corresponding to temperatures of 977 to 1273°C (median = 1074°C). Garnet concentrate produced

a slightly larger spread in Ni temperatures, ranging from 819 to 1273°C (median = 1030°C). The median garnet temperature for the concentrate garnets is within error of that for the garnet within the peridotite xenoliths.

Table 3.4 Representative nickel-in-garnet thermometer results from xenolith mineral separates for Central Victoria Island. Temperatures are given for a representative grain using measured Ni in olivine (in equilibrium with the garnet), or the median value for all olivines of 3418ppm. Garnet grains were selected that most accurately reflected the median temperature reported for the sample population. Mean temperatures are reported for all garnet separated from the xenolith with the number of grains analyzed being indicated by the “count” column.

Sample name	Representative analysis			Mean Temperature (°C)	Count
	Ni (ppm:Garnet)	Ni (ppm: Olivine)	Temperature (°C)		
SnO-11	58.8		1057	1054	4
SnO-12	47.0	3338	1018	1008	4
SnO-15	64.4		1076	1073	26
SnO-17	67.7		1087	1087	11
SnO-19	50.2		1026	1037	13
SnO-20	50.5		1027	1029	9
SnO-23	88.1		1144	1145	7
SnO-24	63.3	3497	1068	1070	60
SnO-26	98.4		1170	1187	10
SnO-28	67.0		1084	1084	9
SnO-29	58.0		1055	1055	3
SnO-32	66.2	3621	1070	1067	9
SnO-33	67.3		1091	1088	2
SnO-34	64.9	3328	1078	1098	9
SnO-35	80.8		1125	1126	10

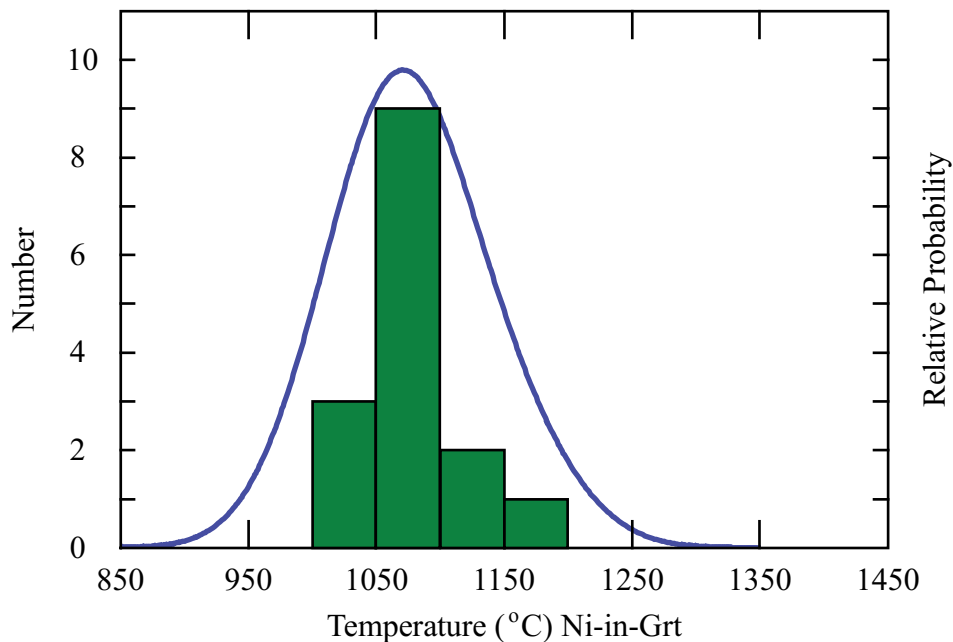


Figure 3.12 Probability density diagram and underlying histogram for Ni-in garnet temperatures from peridotites from the Snowy Owl kimberlite, central Victoria Island, using a single representative temperature for each xenolith. Bandwidth for pdf is 50°C.

### 3.4.2 Single Clinopyroxene Thermobarometer

For peridotites from the Parry Peninsula, fresh clinopyroxene data from the mantle xenoliths can be combined with that from indicator mineral databases to assess the thermal state of the lithosphere beneath that kimberlite field. Using the Nimis and Taylor (2000) single clinopyroxene thermobarometer, PP diopsides from give temperatures ranging between 621 to 839°C (median = 697°C) that correspond to pressures of 22 to 31kbars (median=26kbar; Table 3.5).

Clinopyroxene till concentrate grains from PP (n=352) give higher temperatures (813-1293°C, median=1079°C) and higher pressures (30-62kbars,

median=48kbars) (Appendix A5). Three clusters can be seen in the concentrate at 900°C and 35Kbar, 1100°C and 45-50Kbar and 1250°C and 40-50kbar.

Table 3.5 Temperatures and pressures for representative diopside grains for each Parry Peninsula peridotite, calculated using the Nimis and Taylor (2000) single clinopyroxene thermobarometer.

Sample	Temperature (°C)	Pressure (kbar)
DB1A	839	27
DB2D	765	31
DB3C	705	25
DB4B	621	24
DB5C	650	22
DB6A	660	25
DB7B	791	26
DB8A	669	22
DB9B	723	26
DB11A	689	31

CVI clinopyroxene grains recovered from till concentrate (n=196) show variation between different kimberlite structural trends. The two more central locations (King Eider and Blue Ice trends) have median values of 968°C and 57kbars, (n=1016). When plotted, data roughly agrees with a geotherm of 38mW/m<sup>2</sup>, previously produced Kolebaba *et al.* (2003) from a subset of the same data.

### 3.4.3 Estimating Pressures from Ni-temperatures

Due to the lack of coexisting phases required for many mineral thermobarometers, the CVI xenolith suite does not have independent barometry estimates. By using a reference geotherm produced using FITPLOT (Mather *et al.*, 2011) employing concentrate diopside, calculated Ni-in-garnet temperatures from CVI can be extrapolated to estimate depths of equilibrium. The CVI xenoliths garnet

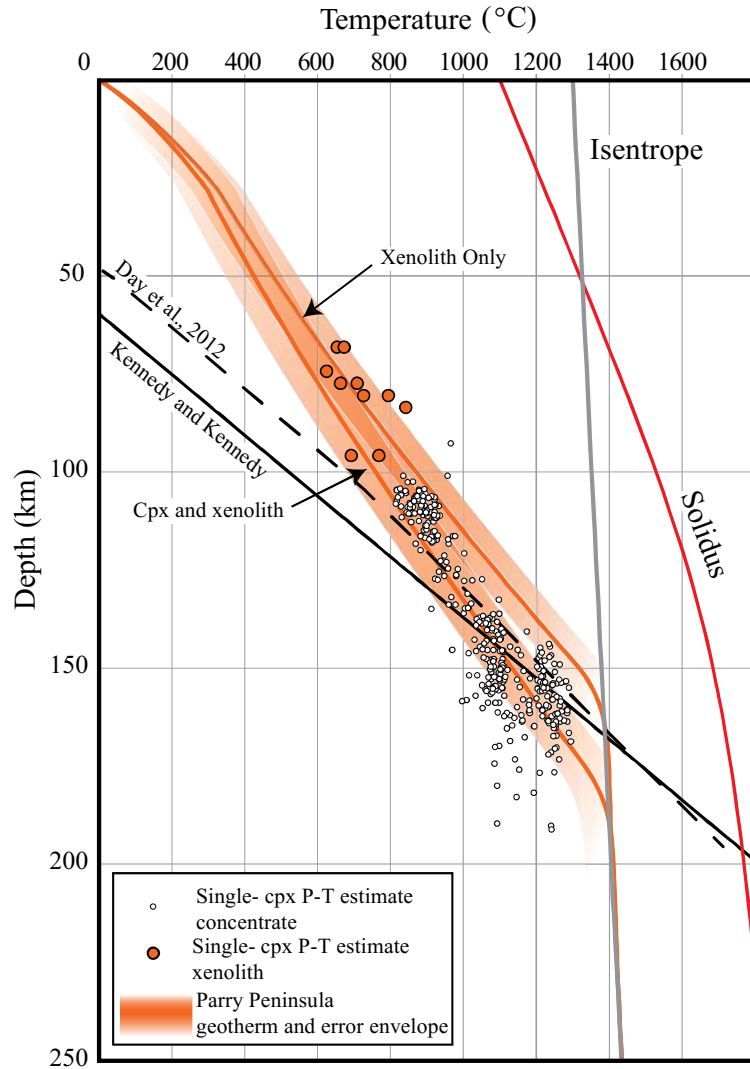


Figure 3.13 FITPLOT (Mather *et al.*, 2011) geotherms for Parry Peninsula. The graphite:diamond transition is delineated by the Kennedy and Kennedy line. Using thermobarometry from xenoliths only results in a geotherm with little diamondiferous mantle. These samples are not well equilibrated as displayed by petrography and by the volume of till concentrate that exist at much higher temperatures and pressures and therefore create a more steep geotherm, when combined with the xenoliths. For the concentrate only geotherm see Appendix A5. For crustal parameters used in FITPLOT see Appendix A6.

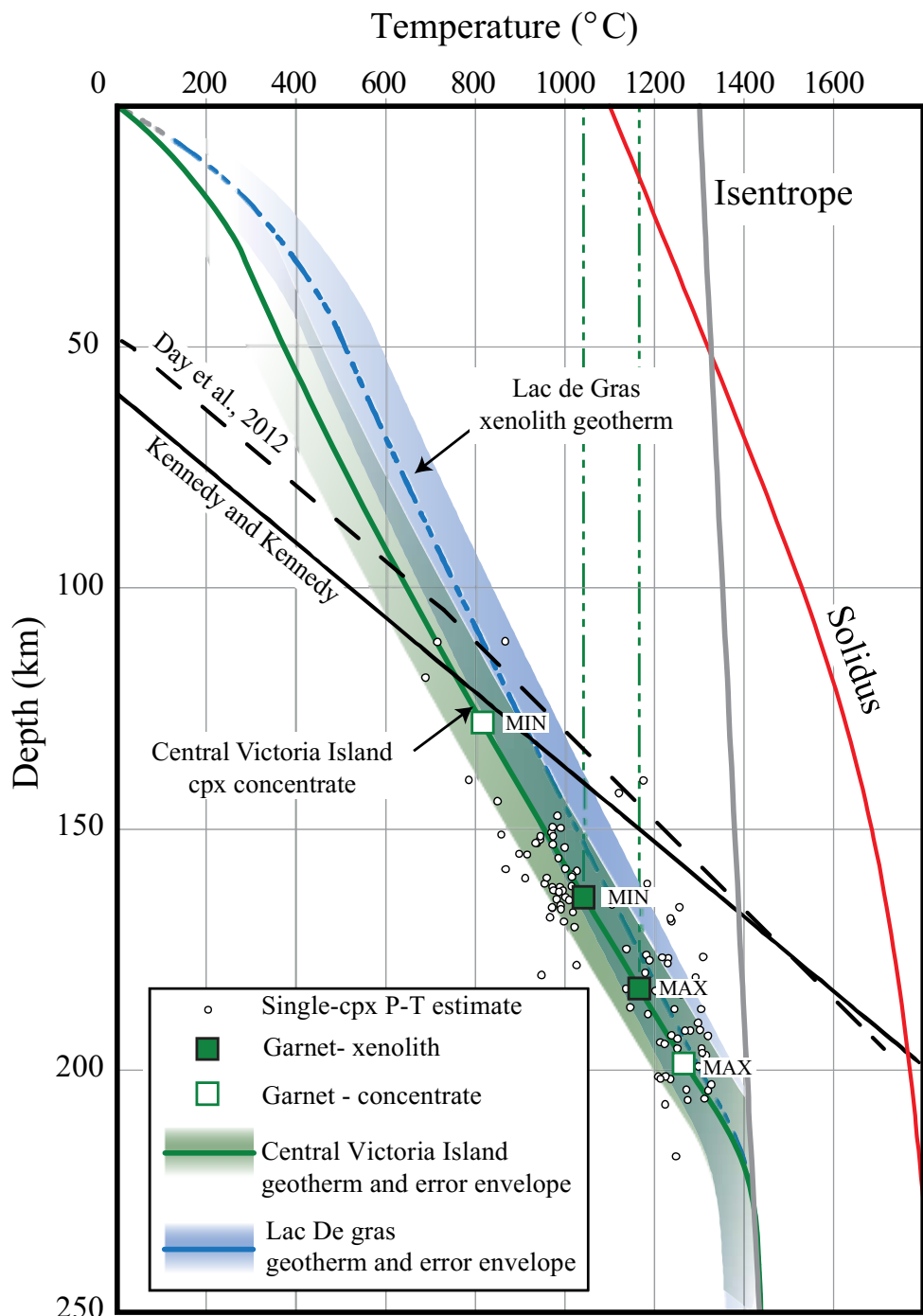


Figure 3.14 FITPLOT (Mather *et al.*, 2011) geotherm of central Victoria Island clinopyroxene till concentrate. Xenolith garnet temperatures defined from Ni-in-Garnet (Canil, 1999) are extrapolated down to the geotherm and suggest a depth range of ~165-185km. Garnet concentrate results in a larger depth range of ~130-200km. For a breakdown of central Victoria Island clinopyroxene concentrate by kimberlite trend see Appendix A5. For crustal parameters used in FITPLOT see Appendix A6.

temperatures result in equilibration depths of 165-185km.

Garnet till concentrate from Victoria Island displays a wider range of Ni contents and therefore temperatures, than the CVI xenoliths. Calculated temperatures extrapolate to depths of 120-200km (Figure 3.14).

### **3.5 Bulk Rock Major-Element Chemistry and Modal Mineralogy**

Parry Peninsula whole-rock peridotite MgO contents vary from 44.5 to 48.5 wt% whereas CVI peridotites have lower MgO contents over a larger range (37.7 to 46.7 wt%; Table 3.7). These ranges are comparable to both global cratonic (mean=  $46.2 \pm 2.9$  wt%, Pearson *et al.*, 2003) and Kaapvaal circum-cratonic peridotites (range 37 to 48wt% MgO; Janney *et al.*, 2010).

The CaO range for PP peridotites is very restricted (0.21-0.98 wt%), with a low median value of 0.61wt% that is similar to cratonic and circum-cratonic peridotites. The low bulk rock Al<sub>2</sub>O<sub>3</sub> of PP lherzolites (median=0.71wt%) is also comparable to cratonic and circum-cratonic peridotites and is lower than that measured in peridotites from Phanerozoic rifts in young tectonic terranes (see compilation in Pearson *et al.*, 2003 and Pearson & Wittig, 2014).

Table 3.6 Whole rock compositions from XRF for central Victoria Island and Parry Peninsula whole rock peridotites and modal mineralogy for Parry Peninsula peridotites

	SnO-12	SnO-14	SnO-15	SnO-17	SnO-19	SnO-20	SnO-21	SnO-24	SnO-26	SnO-27	SnO-28	SnO-29	SnO-32	SnO-33
<b>Major Element Oxides (wt%)</b>														
SiO <sub>2</sub>	46.94	35.94	43.49	44.33	43.20	44.18	45.68	45.69	43.75	45.08	44.83	41.84	43.98	42.47
TiO <sub>2</sub>	0.25	14.32	0.14	0.22	0.25	0.27	0.38	0.11	0.13	0.05	0.10	0.18	0.12	0.07
Al <sub>2</sub> O <sub>3</sub>	1.63	6.29	1.28	1.13	4.61	3.58	1.87	0.70	2.00	0.91	1.18	2.80	1.09	1.51
FeO*	8.83	7.76	8.91	8.69	9.03	8.64	8.31	7.89	8.50	8.26	8.94	8.21	8.29	8.24
MnO	0.21	0.62	0.10	0.09	0.12	0.42	0.18	0.17	0.08	0.07	0.09	0.10	0.11	0.10
MgO	37.74	28.36	41.89	44.48	41.70	40.89	39.10	40.69	44.06	45.12	44.23	43.25	45.29	46.75
CaO	3.86	1.48	3.92	0.70	0.65	1.58	3.27	4.33	1.17	0.31	0.45	3.33	0.62	0.61
Na <sub>2</sub> O	0.12	0.08	0.06	0.07	0.07	0.07	0.13	0.11	0.07	0.07	0.06	0.09	0.14	0.07
K <sub>2</sub> O	0.34	5.05	0.15	0.16	0.30	0.26	0.89	0.28	0.14	0.10	0.05	0.17	0.28	0.13
P <sub>2</sub> O <sub>5</sub>	0.08	0.10	0.07	0.13	0.07	0.11	0.18	0.04	0.10	0.04	0.05	0.03	0.08	0.04
Total	100	100	100	100	100	100	100	100	100	100	100	100	100	100
LOI	16.42	6.34	16.39	15.41	14.22	14.00	15.14	11.99	16.00	16.00	16.03	6.80	13.20	10.86
MG#	88.39	86.69	89.34	90.12	89.16	89.40	89.35	90.19	90.23	90.69	89.81	90.38	90.69	91.00
Mg/Si	1.04	1.02	1.24	1.29	1.25	1.19	1.10	1.15	1.30	1.29	1.27	1.33	1.33	1.42
Ca/Al	3.21	0.32	4.14	0.83	0.19	0.60	2.35	8.40	0.79	0.46	0.52	1.61	0.76	0.54
<b>Trace Element (ppm)</b>														
Sr	304	157	254	163	162	208	508	204	156	158	179	382	195	125
Zr	68	195	64	73	76	42	92	28	30	59	62	77	65	61
V	148	354	111	103	134	91	111	53	68	93	89	141	105	101
Ni	3966	2303	3325	3544	2495	3082	3233	3845	3420	3634	3678	6055	3032	3297
Cr	3857	3510	2582	2019	4216	3070	2187	2120	4260	3434	1952	7408	3123	4304
Co	201	88	103	30	76	99	40	111	91	59	73	115	69	82

Table 3.6 continued

	SnO-34	SnO-35	SnO-36	DB 1A	DB 2D	DB 3A	DB3C	DB 4B	DB 5C	DB 6A	DB 8A	DB 11A
<b>Major Element Oxides (wt%)</b>												
SiO <sub>2</sub>	44.28	44.04	44.17	42.86	43.50	42.45	43.88	46.41	44.30	43.27	42.69	44.08
TiO <sub>2</sub>	0.05	0.19	0.03	0.01	0.02	0.03	0.09	0.01	0.05	0.02	0.01	0.01
Al <sub>2</sub> O <sub>3</sub>	1.56	2.20	0.88	0.65	0.54	0.45	0.87	1.20	1.21	0.67	0.71	0.86
FeO*	8.11	9.43	7.49	7.65	7.29	7.86	7.37	6.73	7.03	7.40	7.80	7.35
MnO	0.08	0.14	0.11	0.13	0.12	0.11	0.12	0.12	0.11	0.13	0.13	0.12
MgO	45.24	41.95	46.27	48.12	47.72	48.53	46.42	44.51	46.75	47.46	47.97	47.23
CaO	0.56	1.61	0.69	0.52	0.72	0.34	0.98	0.88	0.40	0.94	0.61	0.21
Na <sub>2</sub> O	0.04	0.11	0.08	0.04	0.04	0.18	0.07	0.05	0.04	0.05	0.04	0.07
K <sub>2</sub> O	0.04	0.25	0.23	0.02	0.05	0.02	0.10	0.08	0.10	0.05	0.03	0.07
P <sub>2</sub> O <sub>5</sub>	0.03	0.07	0.04	0.01	0.01	0.02	0.09	0.01	0.02	0.01	0.01	0.00
Total	100	100	100	100	100	100	100	100	100	100	100	100
LOI	14.14	9.22	6.72	2.60	3.57	6.40	7.09	2.08	5.35	2.46	2.51	7.25
MG#	90.87	88.81	91.68	91.82	92.11	91.67	91.82	92.18	92.22	91.95	91.64	91.97
Mg/Si	1.32	1.23	1.35	1.45	1.42	1.48	1.36	1.24	1.36	1.42	1.45	1.38
Ca/Al	0.49	0.99	1.07	1.08	1.81	1.02	1.53	1.00	0.44	1.90	1.16	0.32
<b>Trace Element (ppm)</b>												
Sr	47	272	190	55	51	51	212	48	54	51	51	112
Zr	20	71	62	17	14	14	65	13	16	20	18	53
V	70	115	77	48	23	33	76	60	44	45	46	80
Ni	3463	2400	3165	2211	2899	3563	2476	2634	2230	2546	3159	2745
Cr	2887	3052	2617	2051	1534	983	2215	2812	3259	1555	1910	7065
Co	94	79	95	121	101	131	90	103	121	133	116	112
<b>Calculated Modes</b>												
%Ol				83.29	84.58	88.58	74.61	61.76	73.43	80.01	79.68	73.87
%Cpx				2.05	2.04	1.20	3.62	2.65	1.46	3.75	2.37	0.60
%Opx				13.21	12.49	8.76	19.30	34.25	23.24	15.67	17.67	23.81
%Sp				0.56	0.00	0.37	1.07	0.46	2.05	1.20	0.96	2.96
%Grt					0.88							
RSS				0.0	0.10	0.15	0.44	0.11	0.1	0.0	0.1	0.1

CaO is very variable in CVI xenoliths (range=0.31-4.33wt% CaO, median=1.17wt%) extending from values typical of cratonic peridotites (e.g., Pearson *et al.*, 2003) to much higher values. Most of the higher CaO contents, of around 4 wt% have significantly lower Al<sub>2</sub>O<sub>3</sub> concentrations that are more similar to typical cratonic peridotites (median=1.56wt%). High calcium concentrations are likely a result of carbonate crystallization resulting from kimberlite infiltration. This cause has been confirmed by thin section observation and by the observation of elevated bulk rock Sr contents (>200 ppm) in these samples (Fig. 3.15). The few samples with higher Al<sub>2</sub>O<sub>3</sub> (>3%) contain phlogopite.

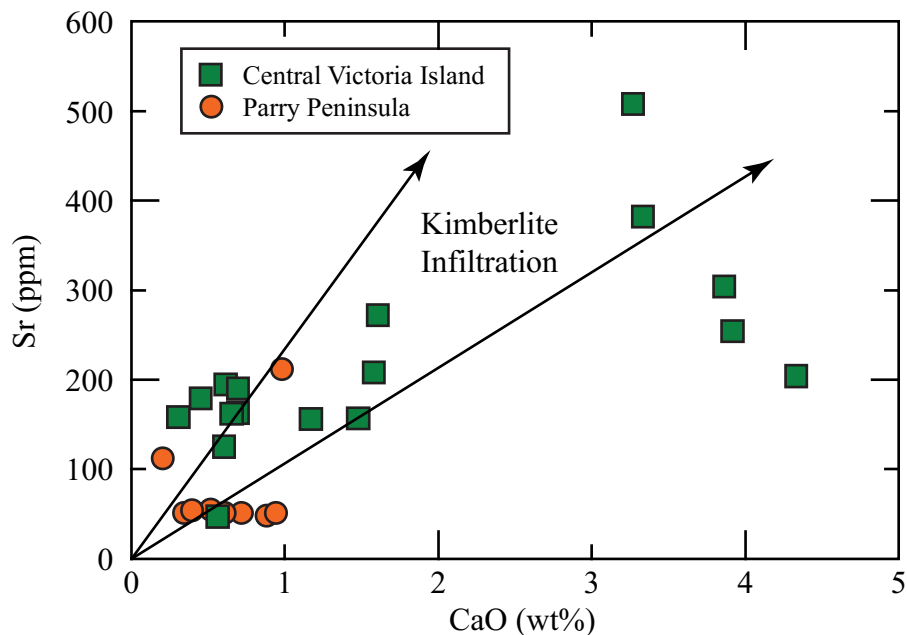


Figure 3.15 Bulk whole rock variation of CaO (wt%) and Sr (ppm) for Central Victoria Island and Parry Peninsula peridotite xenoliths. Kimberlite infiltration vectors indicated by arrows than span a range of Lac de Gras kimberlite compositions from Tappe *et al.* (2013).

Modal mineral proportions were calculated using whole rock compositions and the MINSQ program of Herrmann & Berry (2002). Representative mineral compositions for each PP xenolith were used for calculation to ensure accuracy. The resulting calculated modes for PP peridotites confirms petrological indications that the peridotites are olivine rich, with olivine abundances between 80 to 88% (Table 3.7). In contrast, modal orthopyroxene is low (9 to < 20%) with one exception (DB4B) ranging to 35% but generally higher than the least orthopyroxene-rich cratonic peridotites, typified by the North Atlantic craton (Wittig *et al.*, 2008). As expected from their low Al and Ca contents, modal clinopyroxene is very low (0.006 to 3.75%; Table 3.7). Spinel average <1% in the modes but are as high as 3% in one sample. No modes were calculated from CVI peridotites due to their highly altered state and the lack of fresh mineral compositions with the exception of garnet.

### **3.6 Re-Os Systematics**

#### ***3.6.1 Isotope Systematics***

Peridotites from central Victoria Island show a wide range of Re concentrations from 0.02 to 0.24 ppb, with a mean of 0.09 ppb and a median of 0.08 ppb. PP whole rock powders display a large variation of 0.004 to 0.50 ppb, with a mean of 0.08 ppb, and median of 0.02 ppb. The whole rocks have generally higher Re concentrations than the PP olivines (0.001-0.04 ppb, mean and median=0.01).

Os concentrations for CVI peridotites are variable (0.01-15.23ppb) but their mean value of 4.09ppb (omitting SnO-19; 15.23 ppb) and median of 3.73ppb are typical of those for residual peridotites. Peridotites from PP show a similar range in Os but with lower average Os concentrations (0.05-8.07ppb, mean=2.41ppb, median=1.22ppb). Hand-picked olivine separates for PP peridotites have lower contents (b.d.1 to 5.95ppb, mean=1.60ppb, median=0.62ppb). Overall, Os concentrations for whole rocks from both locations are broadly similar to those reported for the circum-cratonic Kaapvaal craton (2.3-3.6ppb, Janney *et al.*, 2010) and slightly below the mean Os concentration for the Kaapvaal mantle (4.6ppb, Carlson *et al.*, 1999). The  $^{187}\text{Re}/^{188}\text{Os}$  ratios for CVI peridotites (range= 0.0220-0.3144, mean=0.1524, median=0.1475; omitting SnO-5) are consistent with the means for Kaapvaal peridotites (0.11: Carlson *et al.*, 1999) and circum-cratonic Kaapvaal peridotites (0.25,0.16; Janney *et al.*, 2010). The PP  $^{187}\text{Re}/^{188}\text{Os}$  values are significantly lower for both whole rock peridotites (mean=0.263, median=0.08, omitting DB2D) and olivines (mean=0.06537, median=0.02844).

Peridotites from central Victoria Island have a range of Os isotopic compositions ( $^{187}\text{Os}/^{188}\text{Os} = 0.11089-0.12463$ ). The mean is dominated by the rare higher values, however the median  $^{187}\text{Os}/^{188}\text{Os}$  value of 0.11482 is more representative for the suite. The PP whole rock peridotites have a similar range in  $^{187}\text{Os}/^{188}\text{Os}$  (0.11185-0.11617) and a remarkably similar median value (0.11430). The olivines from the same PP peridotites have  $^{187}\text{Os}/^{188}\text{Os}$  values that range to slightly more

radiogenic values than their whole rocks (0.11186-0.12036) with a slightly higher median value (0.11471).

Table 3.7 Re-Os Isotopic systematics for Central Victoria Island peridotites, Parry Peninsula peridotites and their olivines.  $^{187}\text{Os}/^{188}\text{Os}$  uncertainty quoted of  $2\sigma$  (95%) level, internal precision. Model ages and  $\gamma_{\text{Os}}$  values calculated relative to average O-Chondrite,  $^{187}\text{Os}/^{188}\text{Os} = 0.1283$ ,  $^{187}\text{Re}/^{188}\text{Os} = 0.422$ . Eruptions ages for host kimberlites: CVI=271Ma and PP=270Ma. Model ages omitted from SnO-5 due to the large uncertainties.

Sample	Re (ppb)	Os (ppb)	$^{187}\text{Os}/^{188}\text{Os}$	$^{187}\text{Os}/^{188}\text{Os}$ uncertainty	T <sub>RD</sub> Age (Ma)	T <sub>RD</sub> Age (Ma) Re-corrected	T <sub>MA</sub> (Ma)	$^{187}\text{Re}/^{188}\text{Os}$	$\gamma_{\text{Os}} (\text{t})$
<b>Central Victoria Island Whole Rock</b>									
SnO-1	0.03	1.98	0.11303	0.00018	2132	2172	2528	0.0673	-11.9
SnO-5	0.02	0.01	0.11443	0.00406				7.0604	-10.8
SnO-12	0.08	2.42	0.11089	0.00021	2426	2516	3773	0.1538	-13.6
SnO-15	0.03	3.48	0.11560	0.00022	1779	1804	1974	0.0423	-9.9
SnO-17	0.24	2.56	0.12463	0.00025	520	791	-8688	0.4492	-2.9
SnO-19	0.11	15.23	0.11623	0.00035	1691	1712	1839	0.0343	-9.4
SnO-20	0.12	4.08	0.12045	0.00022	1105	1190	1653	0.1411	-6.1
SnO-21	0.07	3.88	0.11357	0.00018	2059	2107	2539	0.0812	-11.5
SnO-24	0.09	7.12	0.11378	0.00018	2030	2067	2377	0.0627	-11.3
SnO-26	0.06	0.96	0.11445	0.00027	1937	2123	7265	0.3144	-10.8
SnO-27	0.03	7.30	0.11475	0.00018	1896	1909	1999	0.0220	-10.6
SnO-28	0.07	5.00	0.11842	0.00021	1389	1432	1669	0.0716	-7.7
SnO-32	0.20	4.82	0.11395	0.00022	2006	2121	3682	0.1953	-11.2
SnO-33	0.19	3.73	0.11619	0.00022	1698	1844	4020	0.2472	-9.4
SnO-34	0.15	3.83	0.11481	0.00022	1888	1996	3298	0.1833	-10.5
SnO-35	0.09	2.76	0.12406	0.00070	600	695	953	0.1571	-3.3
SnO-36	0.02	0.44	0.11587	0.00030	1741	1869	3507	0.2156	-9.7
<b>Parry Peninsula Whole Rock</b>									
DB1A	0.019	1.64	0.11421	0.00021	1971	2004	2258	0.0545	-11.0
DB2D	0.016	0.05	0.11427	0.00063	1963	2794	-873	1.3938	-10.9
DB3A	0.505	8.07	0.11541	0.00035	1804	1985	6074	0.3011	-10.0
DB3C	0.004	0.57	0.11433	0.00028	1954	1975	2130	0.0356	-10.9
DB4B	0.017	4.37	0.11617	0.00020	1700	1711	1776	0.0182	-9.5
DB5C	0.022	0.59	0.11550	0.00033	1792	1900	3074	0.1786	-10.0
DB6A	0.010	3.16	0.11185	0.00022	2294	2302	2374	0.0145	-12.8
DB8A	0.017	0.80	0.11390	0.00021	2013	2075	2655	0.1038	-11.2
<b>Parry Peninsula Olivine</b>									
DB1Aol	0.028	0.51	0.12036	0.00136	1118	1282	3046	0.2696	-6.2
DB2Dol	0.009	0.00							
DB2Eol	0.011	1.98	0.11315	0.00018	2117	2133	2262	0.0275	-11.8
DB3Aol	0.001	0.66	0.11295	0.00018	2143	2148	2180	0.0073	-12.0
DB4Bol	0.039	5.95	0.11637	0.00017	1672	1691	1806	0.0317	-9.3
DB5Col	0.008	0.05							
DB6Aol	0.001	4.35	0.11186	0.00021	2293	2294	2299	0.0011	-12.8
DB8Aol	0.001	1.75	0.11488	0.00082	1879	1880	1886	0.0017	-10.5
DB9Col	0.018	0.58	0.11822	0.00020	1417	1509	2200	0.1520	-7.9
DB11Aol	0.001	0.16	0.11455	0.00024	1924	1942	2066	0.0293	-10.7

### 3.6.2 Model Ages

The macroscopic visual evidence and mineral chemistry evidence for kimberlite infiltration in the CVI and PP suites mean that Re-Os model ages, using measured

Re contents ( $T_{MA}$ ; Walker *et al.*, 1989) will give overestimates due to Re addition from the host kimberlite. We, therefore, employ  $T_{RD}$  ages, calculated assuming Re depletion at the time of melting.  $T_{RD}$  and  $T_{MA}$  ages agree within 500Ma (omitting those samples with impossible ages) for 69% of the CVI dataset and 66% for the PP peridotites.

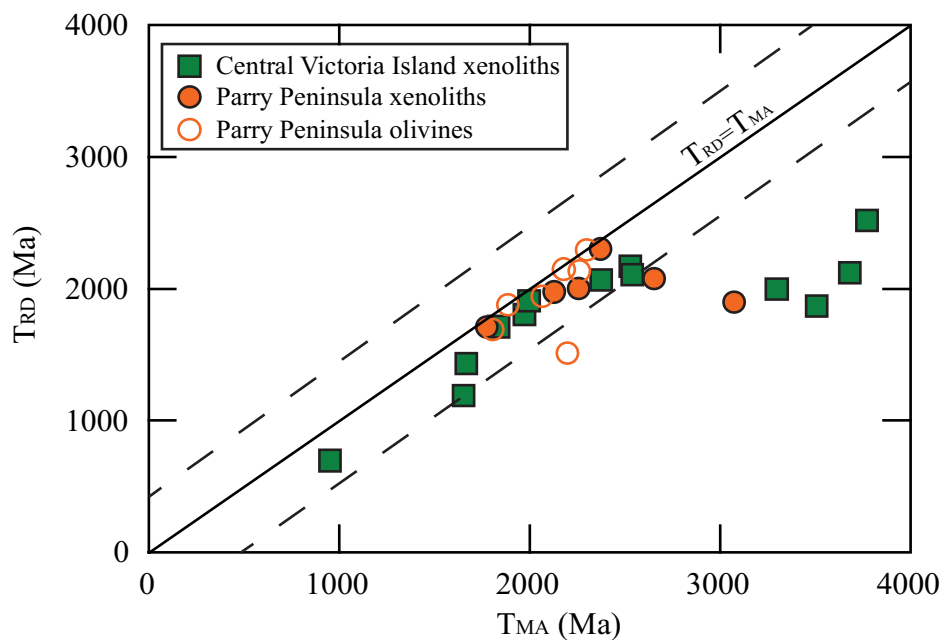


Figure 3.16  $T_{RD}$  versus  $T_{MA}$  model ages for central Victoria Island and Parry Peninsula peridotite xenoliths and olivines. Solid line indicates  $T_{RD}=T_{MA}$ . Dashed lines indicate  $\pm 500$ Ma deviation.

Os model depletion ages ( $T_{RD}$ ) have been corrected for measured Re, to the eruption age of the kimberlite, and correct to reasonable ages. Impossible ages (negative), ages greater than 4.6Ga and those with a large difference between the two methods clearly indicate samples that have undergone modification of their Re/Os ratios since initial depletion.

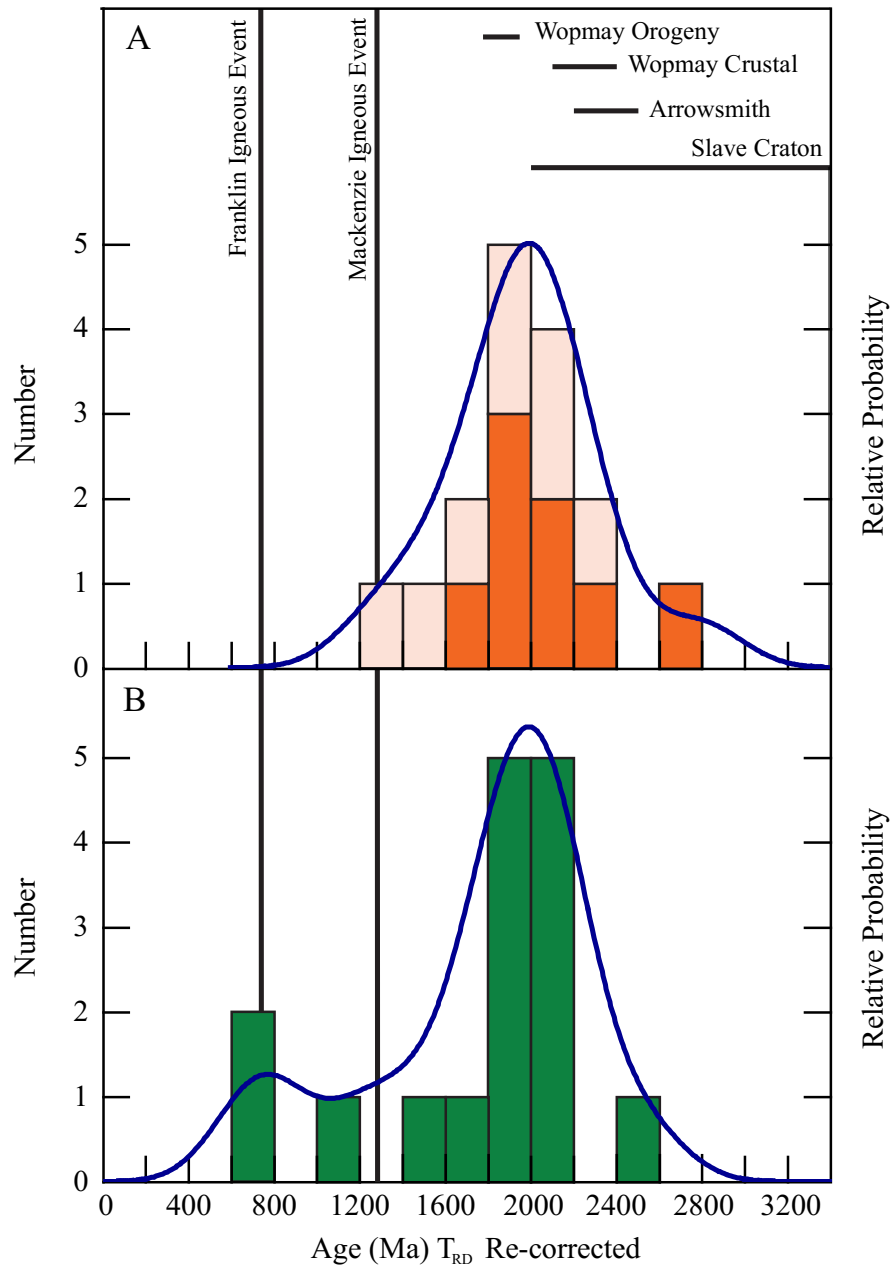


Figure 3.17 Probability density diagram of  $T_{RD}$  and histogram of model ages for A: Parry Peninsula whole rock peridotites (orange) and olivines (light orange) and B: central Victoria Island whole rock peridotites Plotted using a bandwidth of +/- 200Ma for the PDF curve. A: The suite is defined by a strong mode at ~1940Ma, variable dates below 1400Ma and no Archean ages. B: The peridotite suite is defined by a broad peak at ~2.0 Ga, and no Archean ages. Additional lines represent regional crustal events at their respective time intervals: Franklin dyke swarm, Mackenzie dyke swarm, Wopmay orogeny, Arrowsmith orogeny and the Slave craton.

CVI whole rock peridotites are defined by a prominent  $T_{RD}$  model age peak at ~2.0 Ga (Figure 3.17).  $T_{RD}$  ages for PP whole rock peridotites define the same age mode at around 2.0 Ga (Figure 3.17).  $T_{RD}$  model ages for PP olivines are more variable and more likely to report younger and/or impossible ages. Agreement between whole rock and olivine analyses from the same xenolith occurs for four of five samples (within 200Ma). One sample (DB1Aol) shows a larger deviation (780Ma) between whole rock and olivine, with the olivine having a more radiogenic  $^{187}\text{Os}/^{188}\text{Os}$  than the whole rock, at the lower end of the olivine Os contents (~0.5 ppb). This indicates that this particular olivine may have trapped some radiogenic metasomatic sulfide, in contrast to the higher Os content olivines whose low Re/Os indicate that they may have trapped either chromite or unradiogenic low Re/Os sulfides.

### 3.7 Platinum Group Elements

The CVI peridotites fall into four broad whole rock PGE trends on chondrite normalized PGE plots (extended to include Re) that broadly correlate with  $T_{RD}$  ages (Figure 3.18). Trend I displays a depletion in Pt with modest depletions in Pd and Re. All samples within this trend have  $T_{RD}$  ages of 1844 to 2123Ma, bracketing the probability density peak. Trend II is roughly flat from Os to Pd with more enrichment in Pd than Re. With the exception of SnO-34 (1996Ma), these peridotites encompass the five youngest  $T_{RD}$  ages (695-1712Ma). Trend III has very depleted Pt with Pd with lower levels of Re depletion. This trend is also

characterized by lower Os concentrations when compared to Ir such that  $\text{Os}_n/\text{Ir}_n \ll 1$ . Group IV has Os/Ir slightly  $> 1$  with systematic depletions of Pt and especially Pd, accompanied by a “kick” upwards in Re. These patterns reflect samples close to the main age mode and within the model age range of Trend I (1902-2121 Ma).

For PP peridotites, PGE trends also show four distinct trends. Trend I and Trend II are divided on the basis of  $\text{Os}_N$  relative abundance to  $\text{Ir}_N$ . DB5C is the only sample that records a significant Pt-depletion. All samples exhibit Pd depletion relative to Ir and Os with some being much more Pd-depleted than circum-cratonic peridotites from southern Africa (Figure 3.19). The majority of olivine PGE patterns are characterized by having very low Pd (bdl) with variable enrichment in Re (Figure 3.20). In a similar manner to the whole-rock peridotites, the olivines can be classified on the basis of their relative Os/Ir inter-element fractionation. Unique features include DB1Aol having a positive slope from Os to Pt; DB3Aol having significantly more Pd and Pt than other olivines, resembling more the Trend 1 PP whole rocks and DB2Dol having very low concentrations of all PGEs, with Os at blank levels. Hence while some of the olivine I-PGE abundances approach those of whole-rocks, none of the P-PGE (Pt or Pd) are close except for one sample (DB3A ol).

Table 3.8 PGE concentrations for central Victoria Island whole rock xenoliths, Parry Peninsula whole rock xenoliths and Parry Peninsula Olivines. Ratios are normalized to chondrite using the values of McDonough and Sun (1995).

Sample name	Os (ppb)	$\pm$	Ir (ppb)	$\pm$	Pt (ppb)	$\pm$	Pd (ppb)	$\pm$	Re (ppb)	$\pm$	(Pd/Ir) <sub>N</sub>	(Pt/Ir) <sub>N</sub>
<b>Central Victoria Island whole rock</b>												
SnO-1	2.0	0.30	9.42	1.99	11.39	1.34	9.89	1.48	0.03	0.01	0.87	0.54
SnO-5	0.01	0.00	0.04	0.00	0.22	0.00	0.02	0.00	0.02	0.01	0.53	2.60
SnO-12	2.42	0.36	2.46	0.24	1.29	0.05	0.54	0.08	0.08	0.03	0.18	0.24
SnO-15	3.48	0.52	4.42	0.54	4.98	0.33	1.76	0.26	0.03	0.01	0.33	0.51
SnO-17	2.56	0.38	2.99	0.26	8.51	0.85	5.41	0.81	0.24	0.10	1.50	1.28
SnO-19	15.2	2.29	4.72	0.90	7.81	1.15	6.16	0.92	0.11	0.04	1.08	0.74
SnO-20	4.08	0.61	3.45	0.51	5.14	0.55	4.00	0.60	0.12	0.05	0.96	0.67
SnO-21	3.88	0.58	3.92	0.65	2.91	0.23	1.25	0.19	0.07	0.03	0.26	0.33
SnO-24	7.12	1.07	6.89	1.55	6.66	0.86	1.21	0.18	0.09	0.03	0.15	0.44
SnO-26	0.96	0.14	1.75	0.16	0.69	0.02	0.81	0.12	0.06	0.04	0.38	0.18
SnO-27	7.30	1.10	6.37	1.72	7.60	1.27	0.13	0.02	0.03	0.02	0.02	0.54
SnO-28	5.00	0.75	4.85	0.95	6.31	0.79	4.91	0.74	0.07	0.03	0.84	0.59
SnO-32	4.82	0.72	4.42	1.05	5.79	0.90	0.24	0.04	0.20	0.18	0.04	0.59
SnO-33	3.73	0.56	3.48	0.60	5.96	0.77	1.42	0.21	0.19	0.10	0.34	0.77
SnO-34	3.83	0.57	3.91	0.68	4.50	0.47	3.66	0.55	0.15	0.09	0.77	0.52
SnO-35	2.76	0.41	2.50	0.16	4.87	0.35	3.21	0.48	0.09	0.03	1.06	0.88
SnO-36	0.44	0.07	2.27	0.26	0.08	0.00	0.06	0.01	0.02	0.01	0.02	0.02
<b>Parry Peninsula Whole Rock</b>												
DB1A	1.64	0.25	1.13	0.08	2.57	0.18	bdl	-	0.019	0.01	0.016	1.02
DB2D	0.05	0.01	0.34	0.01	0.13	0.00	bdl	-	0.016	0.01	0.002	0.17
DB3A	8.07	1.21	3.27	0.59	2.24	0.20	0.619	0.62	0.505	0.49	0.156	0.31
DB3C	0.57	0.09	2.23	0.21	0.44	0.01	0.335	0.33	0.004	0.01	0.124	0.09
DB4B	4.37	0.66	3.30	0.41	2.48	0.14	bdl	-	0.017	0.01	0.020	0.34
DB5C	0.59	0.09	0.63	0.03	0.08	0.00	0.099	0.10	0.022	0.01	0.130	0.06
DB6A	3.16	0.47	1.52	0.06	2.23	0.07	0.115	0.00	0.010	0.01	0.063	0.66
DB8A	0.80	0.12	3.80	0.55	5.03	0.53	bdl	-	0.017	0.01	0.009	0.60
DB11A	0.02	0.00	0.02	0.00	0.05	0.00	bdl	-	0.012	0.01	1.905	1.10
<b>Parry Peninsula Olivine</b>												
DB1Aol	0.51	0.08	0.65	0.23	1.95	0.87	bdl	-	0.028	0.13	0.001	1.36
DB2Dol	0.00	0.00	0.00	0.00	0.07	0.00	bdl	-	0.009	0.07	0.360	13.2
DB2Eol	1.98	0.30	2.57	4.72	0.46	0.07	bdl	-	0.011	0.61	0.000	0.08
DB3Aol	0.66	0.10	1.48	1.96	1.04	0.37	bdl	-	0.001	0.14	0.082	0.32
DB4Bol	5.95	0.89	0.82	0.35	0.59	0.11	bdl	-	0.039	0.05	0.001	0.33
DB5Col	0.05	0.01	0.02	0.00	0.07	0.01	bdl	-	0.008	0.11	0.046	1.83
DB6Aol	4.35	0.65	2.21	24.7	1.58	1.40	bdl	-	0.001	0.38	0.000	0.32
DB8Aol	1.75	0.26	1.48	1.55	1.50	1.15	bdl	-	0.001	0.30	0.001	0.46
DB9Col	0.58	0.09	0.21	0.04	0.39	0.06	bdl	-	0.018	0.05	0.004	0.83
DB11Aol	0.16	0.02	0.22	0.02	0.07	0.00	bdl	-	0.001	0.00	0.004	0.14

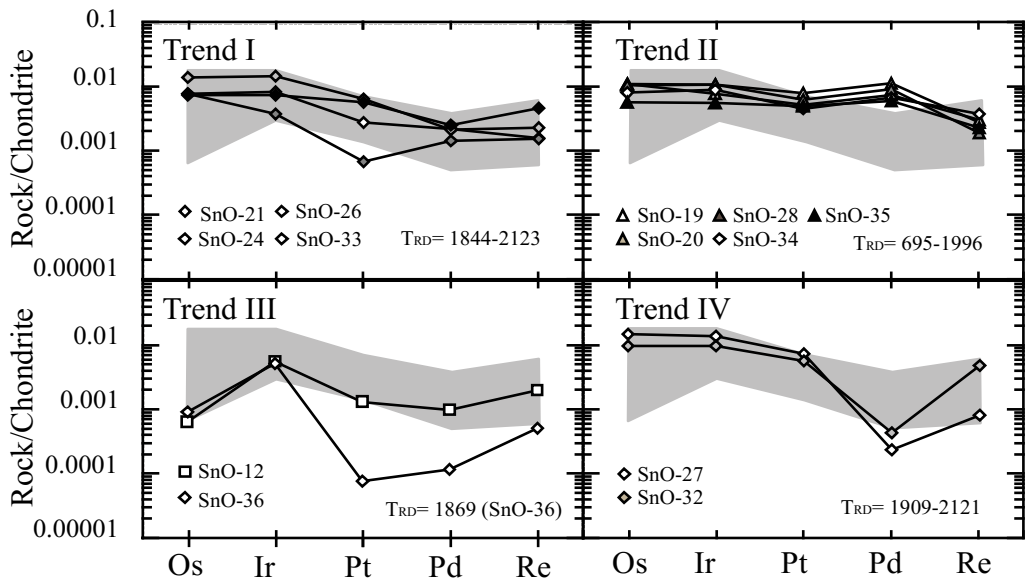


Figure 3.18 Chondrite-normalized central Victoria Island peridotite PGE patterns. Square: >2500Ma, diamond: 1800-2500Ma, Triangle: <1800Ma, circle: undetermined. The grey field indicates the range of composition of circum-cratonic peridotites from southern Africa (Janney *et al.*, 2010). Normalization values from McDonough and Sun, 1995.

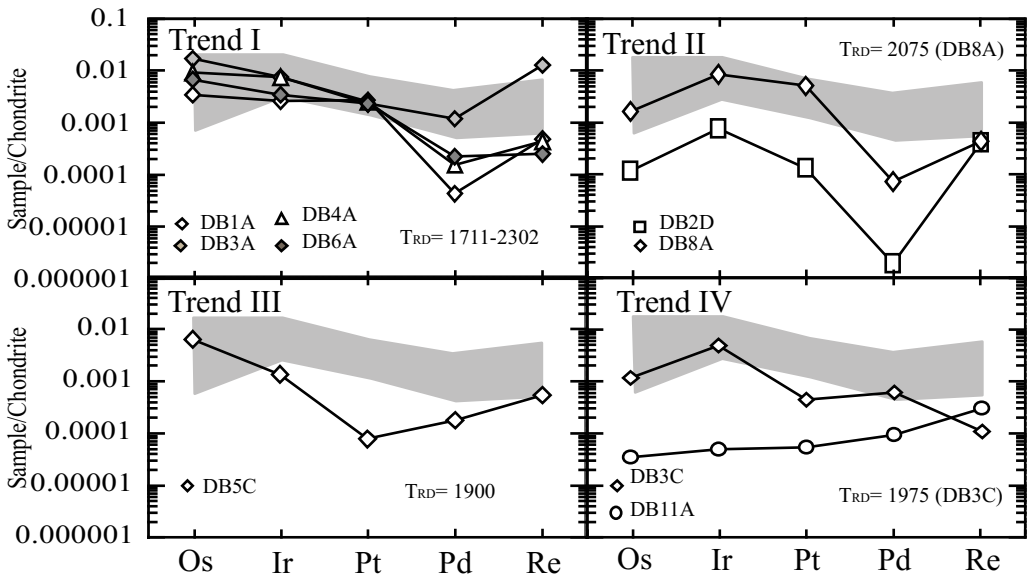


Figure 3.19 Chondrite-normalized Parry Peninsula whole rock peridotite PGE patterns. Square: >2500Ma, diamond: 1800-2500Ma, Triangle: <1800Ma, circle: undetermined. The grey field indicates the range of composition of off-craton peridotites from southern Africa (Janney *et al.*, 2010). Normalization values from McDonough and Sun, 1995.

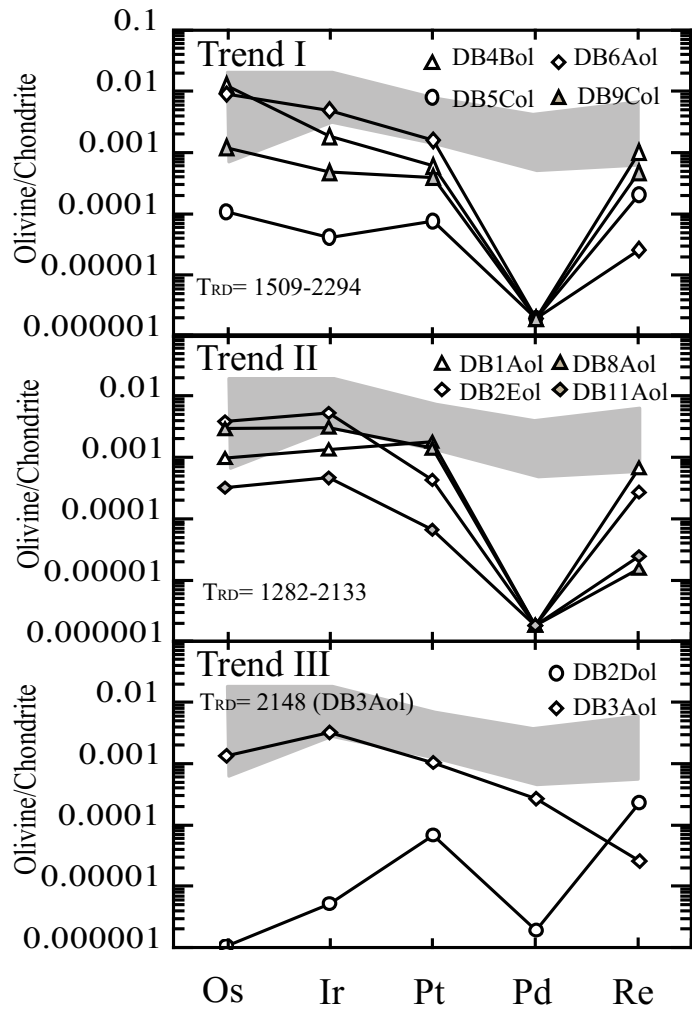


Figure 3.20 Chondrite-normalized Parry Peninsula olivine PGE patterns. Square: >2500Ma, diamond: 1800-2500Ma, Triangle: <1800Ma, circle: undetermined. The grey field indicates the range of composition of off-craton peridotites from southern Africa (Janney *et al.*, 2010). Normalization values from McDonough and Sun, 1995.

## CHAPTER 4: Discussion

### 4.1 Metasomatic interactions

#### 4.1.1 Bulk-rock compositions

Samples from both peridotite suites display signs of metasomatic interaction with a variety of components, that have modified their compositions. Before evaluating the primary causes of compositional variation such as melt depletion, it is important to understand the extent of these metasomatic interactions. It is clear from the bulk-rock variation in Al and Ca that samples have experienced contamination/interaction with both kimberlite (which has a wide range of Ca/Al ratios: Figure 4.1) and phlogopite addition (which may be the result of early kimberlite interaction), driving some CVI bulk rocks to anomalously high Al<sub>2</sub>O<sub>3</sub> (3.5 to 4.5 wt%) at low CaO (<2 wt %; Figure 4.1). The removal of these samples (Figure 4.1B) results in a dataset that lies close to the overall cratonic peridotite melt extraction trend.

#### 4.1.2 Garnet trace-elements

Chemical modification of the peridotites is evident from their complex garnet REE patterns. The CVI Trend I REE patterns (Figure 3.11) with positive sloped LREEs and flat, enriched MREEs-HREEs are "typical" lherzolite patterns and are associated with melt metasomatism (Stachel *et al.*, 2004). Burgess and Harte (2004) suggest that percolating melts rise upwards through the mantle and

crystallize garnets at the base of the lithosphere at high temperatures. This process should also impart higher FeO and Ti in the garnets, which is evident from Figure 4.2. In particular, nearly all CVI garnets from this study with  $\text{Ti} > 1000 \text{ ppm}$  display a lherzolitic REE trend. The increase in Ti and Fe is accompanied by decreasing LREE/HREE fractionation seen in the  $(\text{Sm}/\text{Dy})$  values and this signature is typical of silicate melt metasomatism seen in cratonic garnet peridotites (e.g., Simon *et al.*, 2007).

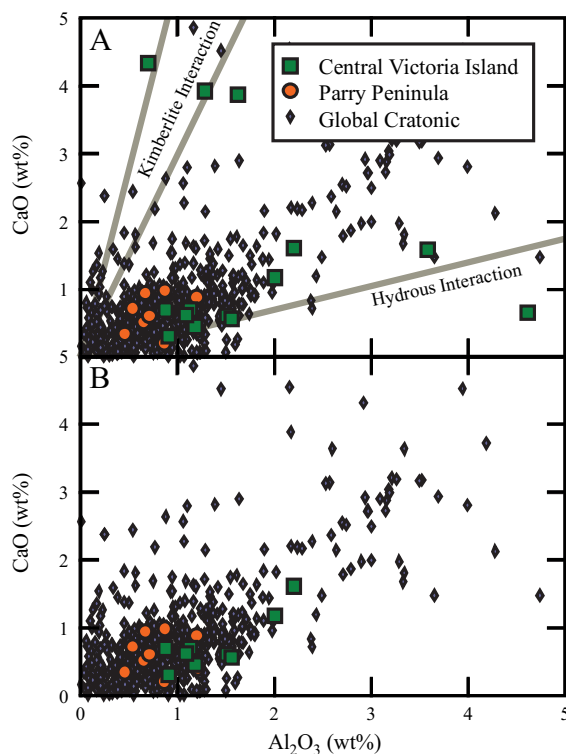


Figure 4.1 Bulk rock CaO (wt%) versus bulk rock  $\text{Al}_2\text{O}_3$  (wt%). A: sub-vertical vectors in the direction of kimberlite composition (high Ti, low Ti; Kjarsgaard *et al.*, 2009), sub-horizontal vector for phlogopite. B: Data filtered for sampled with anomalous Ca and or Al. Global cratonic peridotite data set from Pearson *et al.*, 2004.

The majority of the CVI peridotitic garnets display re-enrichment of LREEs (type II-III, Figure 3.11) producing sinusoidal patterns generally affiliated with

harzburgitic compositions (Stachel *et al.*, 1989). Stachel *et al.* (1998) and Klein-BenDavid and Pearson (2009) propose that the sinusoidal harzburgitic garnet signatures represent reactions involving diamond-forming fluids. Type IIIa and IIIb garnets show enrichment to different degrees, possibly due to different intensities of metasomatism by the same fluid or metasomatism by separate diamond-forming fluids of different compositions. It should be noted that all CVI garnets occur within the lherzolitic field on Ca-Cr plots and are classed as lherzolitic in terms of their bulk-rock mineral modes, therefore, these signatures are most likely inherited. SnO-23 retains a harzburgitic REE signature but the high Ti contents suggest that the sample may have undergone melt metasomatism more characteristic of lherzolites.

The vast majority of the REE patterns from the till concentrate dataset show Trend I lherzolitic garnet signatures. This and the dominant lherzolitic classification on the Cr-Ca plot (Figure 3.9) suggests that mantle under central Victoria Island is dominated by lherzolites.

The elevated Ti contents of most of the garnets are not reflected in their Zr and Y contents, which remain low and in the “depleted” field of Griffin *et al.* (1999b). Nonetheless, there are 2 distinct trends evident, one defined by increasing Zr and Y and another by increasing Zr at relatively constant Y (Figure 4.3), that are consistent with the “silicate melt” enrichment and hydrous enrichment vectors

defined by Griffin *et al.* (1999b). These trends evolve away from exceptionally depleted garnet compositions.

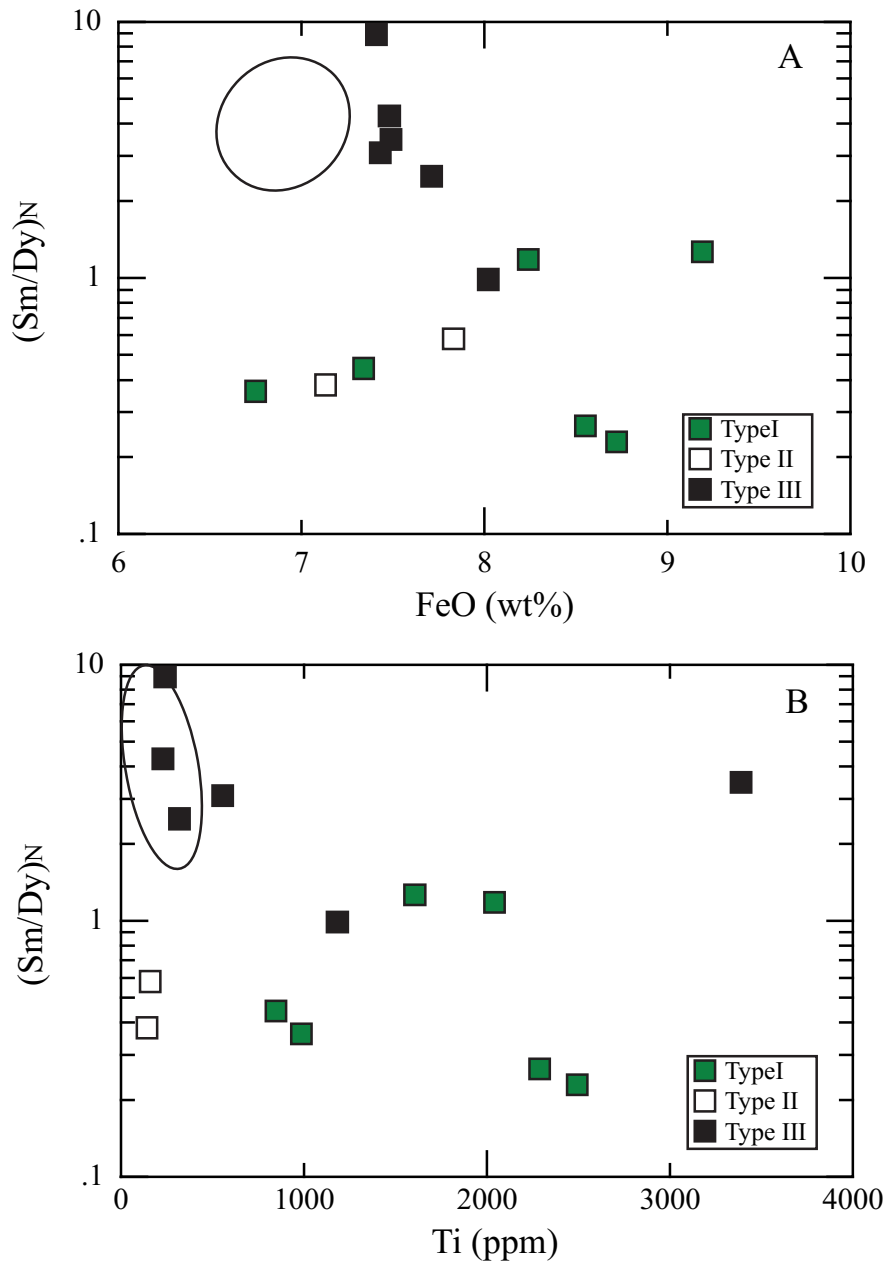


Figure 4.2 A:  $(\text{Sm}/\text{Dy})_N$  vs FeO (wt%) for central Victoria Island garnets. B:  $(\text{Sm}/\text{Dy})_N$  vs  $\text{TiO}_2$  (wt%) for central Victoria Island garnet. Type I lherzolitic, Type II depleted with LREE enrichment, Type III harzburgitic with variable re-enrichment. Fields indicate harzburgitic signatures from Simon *et al.*, 2007. Ti and FeO increase in garnets that have experienced metasomatism.

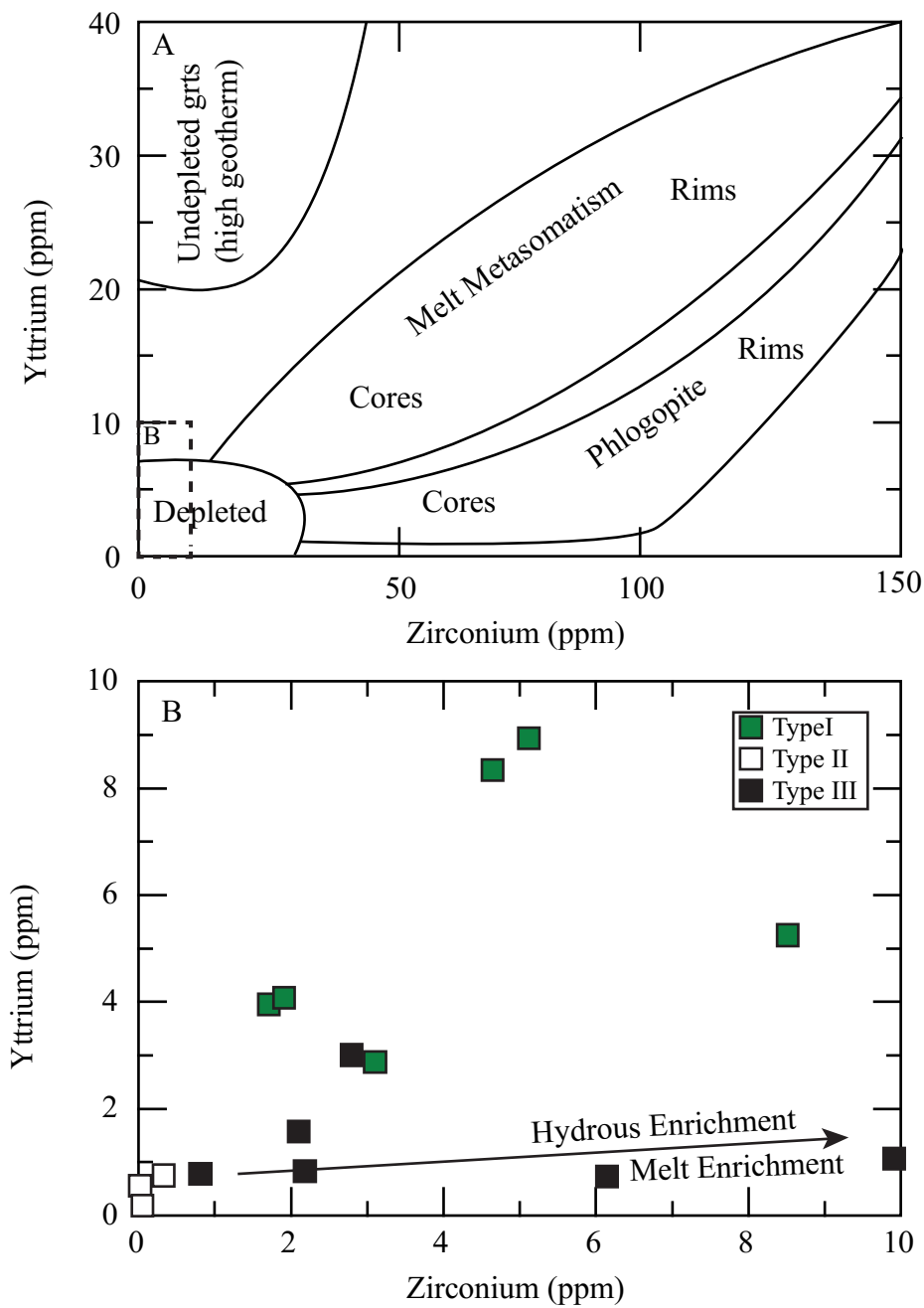


Figure 4.3 Co-variation of yttrium and zirconium for central Victoria Island mantle garnets. A: Fields of depleted and undepleted protoliths with metasomatic processes. Dashed line outlines area enhanced in B. Fields after Griffin *et al.*, 1999b. B:CVI peridotite garnets by garnet trace-element type. Garnets with  $Y < 10$  ppm mainly occur in Archean mantle. Hydrous and melt enrichment are indistinguishable at such low Zirconium values.

## 4.2 Melt Depletion

### 4.2.1 Mineral Chemistry and Major-Element Evidence

A primary objective of this study is to ascertain the affinities of the lithospheric mantle in the areas studied to cratonic mantle, in order to address the issue of whether either of the two areas represent extensions of the Slave craton or newly recognized cratonic mantle keels. Peridotite xenoliths analyzed in this study have a number of characteristic features of Archean cratonic CLM, in particular, the signature of the effects of very large extents of melt depletion, that is expressed in terms of their mineral and bulk-rock, major-element chemistry.

Once the effects of metasomatic infiltration have been accounted for, the generally low Ca and Al contents ( $\sim 1$  wt %) of both the CVI and PP peridotite samples and their position on the cratonic peridotite global trend (Figure 4.1) is an obvious indication of high degrees of melt extraction, i.e., these rocks represent refractory residual compositions.

The inference of extensive melt depletion in both sample suites is reflected in their olivine chemistry. Olivine compositions (CaO and MG#) for the PP peridotites are within the range reported for typical cratonic mantle. While Archean CLM has a pronounced mode of Fo<sub>92.6</sub> (Pearson and Wittig, 2008), PP olivines are slightly less magnesian at Fo<sub>92.2±0.22</sub>; (Figure 4.4) and more closely resemble the marginally lower Fo contents (average: Fo<sub>92.2</sub>) more typical of

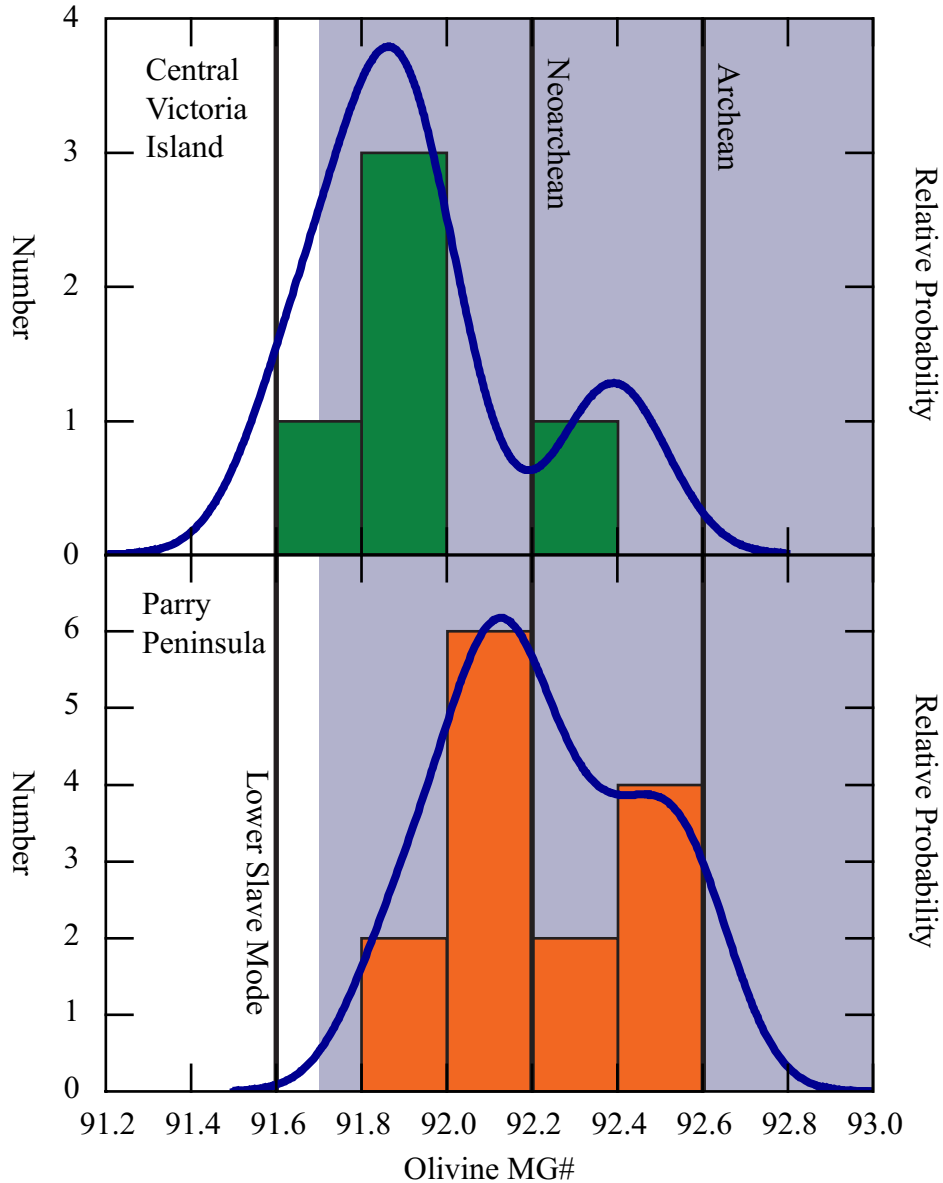


Figure 4.4 Histograms of Olivine MG# for central Victoria Island and Parry Peninsula. The blue field represents the range of cratonic mantle olivine. Lines are the modes in MG# for Archean and Neoarchean olivines from Irvine *et al.* (2003) & A. Luguet *et al.*, 2009); Lower Slave mode from Pearson and Wittig, 2008. PDF bandwidth is 0.25 for CVI and 0.23 for PP.

olivine from Neoarchean peridotitic lithosphere such as that beneath Somerset Island (Rae craton; Irvine *et al.*, 2003) and the Argyle diamond mine (marginal to the Kimberley Craton, Australia; Luguet *et al.*, 2009). In contrast, olivine from

CVI peridotites have a mode at somewhat lower MG# ( $\text{Fo}_{91.9\pm0.3}$ ). However, even this composition is within the range shown by cratonic and circum-cratonic peridotites (Figure 4.4), lying between the two modes at  $\text{Fo}_{92.6}$  and  $\text{Fo}_{91.6}$  defined by peridotites from the Slave craton. All the high MG# olivines from both PP and CVI are consistent with an origin via high degrees of partial melting (26 to 40%) of fertile mantle (Figure 4.5), irrespective of the depth of melting.

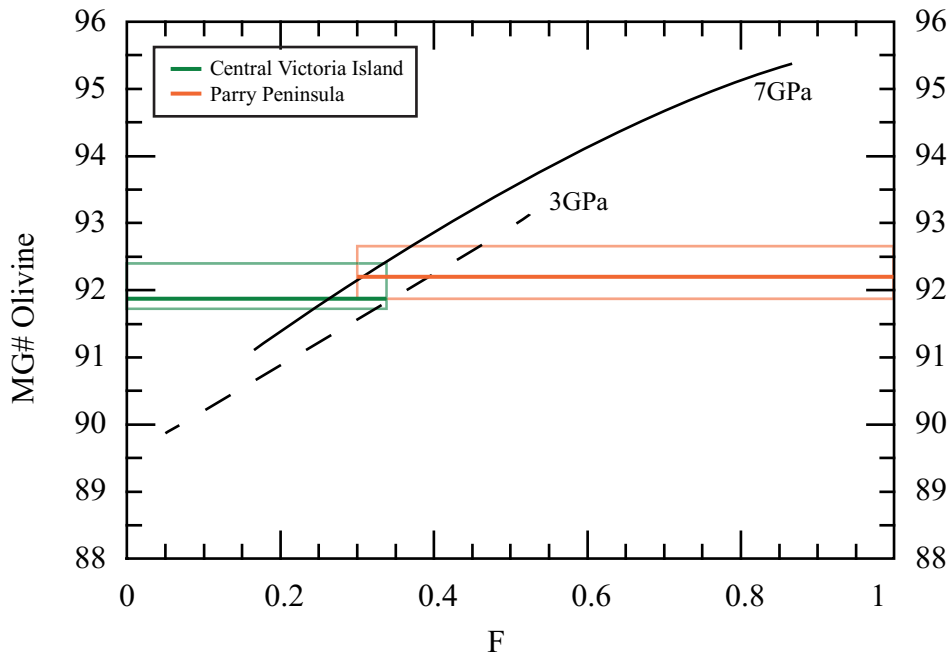


Figure 4.5 Olivine MG# vs. melt fraction for residual peridotites. Pressure curves for 3 and 7 GPa melting from summary in Pearson & Wittig (2008). Median and ranges for olivine MG# are extrapolated to the pressure curves to derive approximate melt fractions, which show some pressure dependency. Peridotites from both CVI and PP suites indicate residual peridotite formation at high degrees of melting > 25% to 40%.

The effects of extensive melt removal are also reflected in the chemistry of spinels within the CVI peridotites, with high CR#, low  $\text{TiO}_2$  and low  $\text{Fe}^{3+}$  being consistent with extensive melt removal. PP spinels have similarly low  $\text{Fe}^{3+}$  and

$\text{TiO}_2$ , but more moderate Cr#s, consistent with their equilibration within the spinel-facies. Barnes and Roeder (2001) outline trends for spinel formation based on their  $\text{Fe}^{3+}$ -Cr-Al relationships. PP spinels plot parallel to the CrAl trend, also referred to as the mantle residue trend (Figure 4.6), with extremely low  $\text{Fe}^{3+}$ .

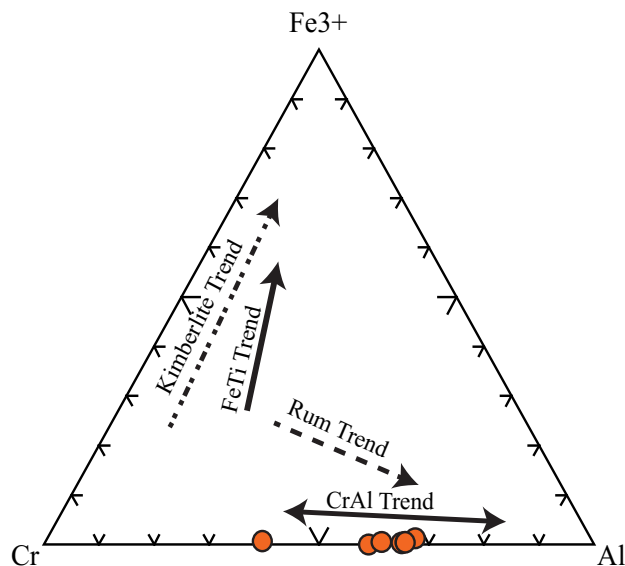


Figure 4.6 Spinel Tri-plot of  $\text{Fe}^{3+}$ -Cr-Al. PP spinels plot parallel to the Cr-Al or “mantle trend” indicating formation from depleted mantle. All trends from Barnes and Roeder (2001).

Garnet geochemistry from the two peridotite suites reflects, to some extent, their common history of extensive melt depletion. While the CVI peridotite garnets plot well into the lherzolite zone (G9) of a Cr-Ca plot (Figure 3.9), some of the concentrate garnets plot well into the G10 “sub-calcic” field, with  $\text{Cr}_2\text{O}_3$  contents of >15 wt%. Such high-Cr garnets primarily reflect their great depth of equilibration. However, experimental melting studies combined with Cr/Al partitioning arguments indicate that it is only possible to make such high-Cr, low-

Ca garnets from residues that have experienced very extensive melt removal in the spinel-facies followed by metamorphic reaction to form high-Cr, low-Ca garnets (Stachel *et al.*, 1998). A subset of the CVI peridotite garnets exhibit typical cratonic harzburgitic REE signatures (Type III, Figure 3.11). These CVI garnets have very low Y and Zr (<10ppm; Figure 4.3), a signature mainly associated with unmetasomatized, highly depleted, mantle beneath Archean terranes (Griffin *et al.*, 1999a) and indicative of extensive melt depletion in the absence of garnet (Canil, 2004).

#### **4.2.2 PGE Evidence**

Increasing degrees of melt extraction from Primitive Mantle induces a systematic change in the inter-element fractionation of the PGEs (e.g., Pearson *et al.*, 2004). This results in more melt-depleted samples having lower P-PGE (Pt, Pd) and Re concentrations, due to their lower compatibility during melting, while I-PGE concentrations increase slightly due to their compatibility. This transformation from relatively flat, un-fractionated chondrite-normalized PGE patterns in residues from moderate degrees of melting (5 to 10%) to patterns showing striking depletions in P-PGEs relative to IPGEs occurs when base-metal sulfide-monosulfide solid solutions breakdown as sulfur is removed into the melt and the P-PGEs become incompatible (Pearson *et al.*, 2004; Aulbach *et al.*, in press). The most extreme examples of such fractionations are observed in cratonic peridotites which are typically residues form in excess of 30% melt extraction, at which point all sulfur in the bulk rock should have been extracted into the melt (Pearson *et al.*,

2004). As such, low P-PGE/I-PGE ratios are good indicators of a) extensive melt depletion in peridotites and b) a cratonic origin for the peridotites, although a few localities in the modern Earth have produced PGE patterns with extreme P-PGE depletions (e.g., Liu *et al.*, 2015).

All of the PP whole rock peridotites have very low Pd (some below limits of detection; Figure 3.20), indicating extremes of melt depletion, well past the level of sulfide-out ( $F \sim 25\%$ , depending on the exact melting model used; Pearson *et al.*, 2004). As Pd does not form alloys on sulfide breakdown (Mungall & Brenan, 2015) then Pd becomes very incompatible at high melt fractions. Thus, the  $<1$  ppb Pd concentrations in the PP peridotites are a very clear indication of high levels of melt depletion. Some CVI peridotites also have very low Pd concentrations ( $<0.5$  ppb) and confirm their refractory nature. Interestingly, the behavior of Ir differs between the two peridotite suites. Ir concentrations in CVI peridotites scatter around the model melt extraction curve that assumes Ir alloy formation upon sulfide breakdown (Figure 4.7). In contrast, the PP peridotites have Ir concentrations that are systematically low compared with those expected if Ir alloy remains stable (Figure 4.7). The lower Ir concentrations, at very low bulk rock  $\text{Al}_2\text{O}_3$ , can only be achieved if Ir alloy solubility in the melt is increased at high melt fractions, for example via increased  $f\text{O}_2$  (Mungall & Brenan, 2015; Aulbach *et al.*, in press). This difference in the behavior of Ir may indicate a fundamental difference in oxygen fugacity in the melting environment of the two mantle locations.

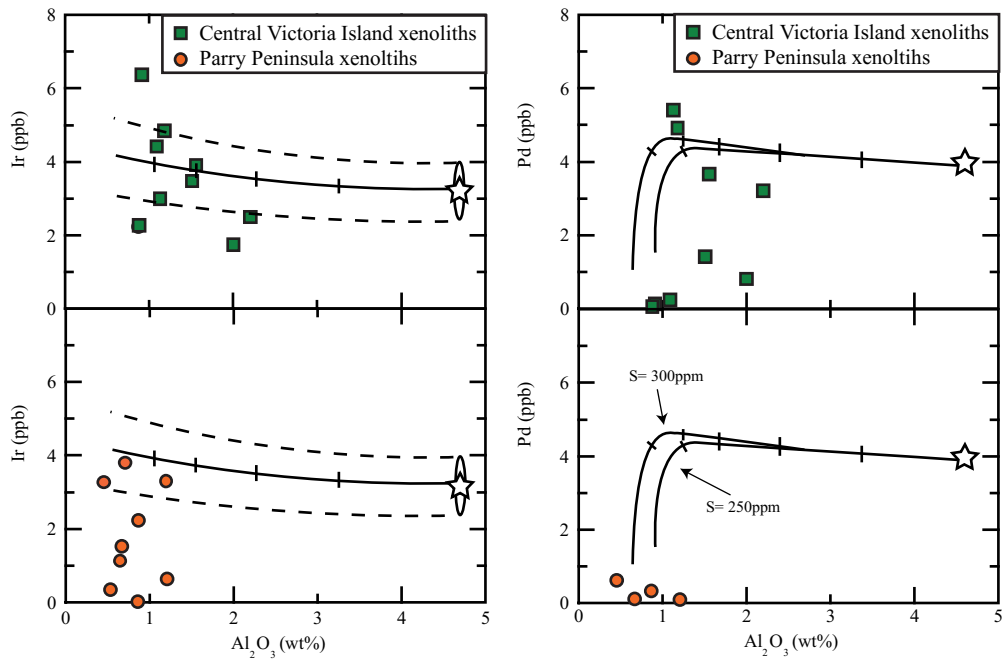


Figure 4.7 Variation of bulk rock Ir and Pd with  $\text{Al}_2\text{O}_3$ . Curves from Pearson *et al.* (2004) model the expected variation in Ir and Pd within mantle residue experiencing progressive melt extraction from a primitive mantle source (star symbol). Tick marks indicate 5% melting increments. The dotted line on the Ir melting trends illustrate the effect of increasing or decreasing the primitive mantle Ir content to represent mantle heterogeneity. The two solid trends marked on the Pd melting trends indicate the effect of varying the source S content between 300 and 250 ppm.

The very low Pd concentrations of many of the CVI and PP peridotites translate into low Pd/Ir and Pt/Ir values, despite the low Ir of some PP samples. Global cratonic peridotites have median Pd/Ir of 0.2 (chondrite normalized Pd/Ir = 0.29) and median Pt/Ir of 0.4 (chondrite-normalized Pt/Ir of 0.43) that are well below 1.0 and indicate significant melt depletion (Pearson *et al.*, 2004; Aulbach *et al.*, in press). All the PP peridotites have  $(\text{Pd}/\text{Ir})_n$  ratios below the median value for cratonic peridotites (Figure 4.8), as expected from the very P-PGE depleted PGE patterns.

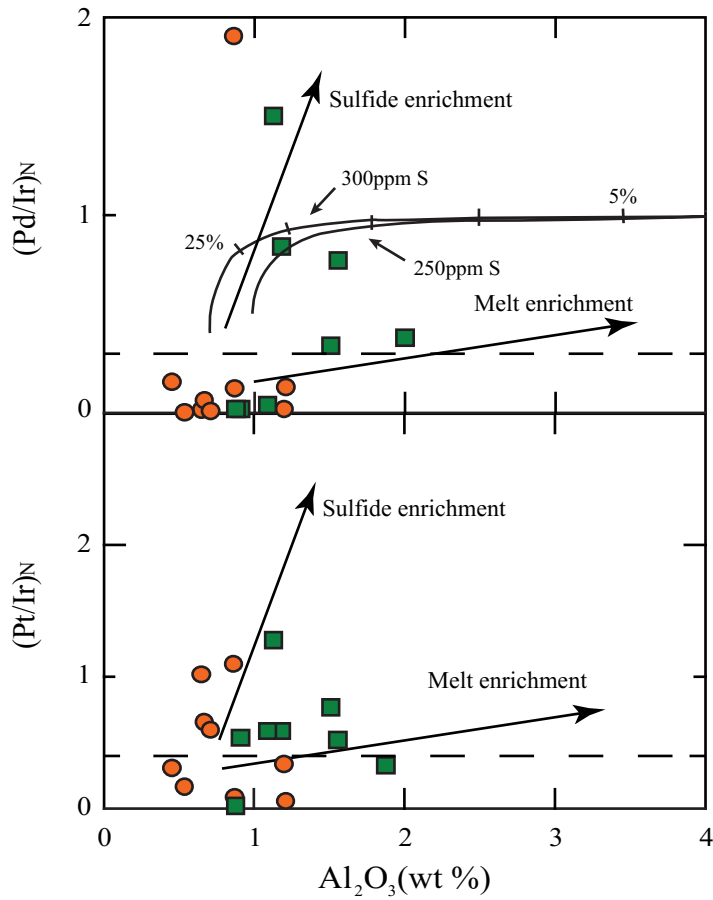


Figure 4.8 Co-variation plots of normalized  $\text{Pd}/\text{Ir}$  and  $\text{Pt}/\text{Ir}$  versus  $\text{Al}_2\text{O}_3$ . Curves on upper plot are the trends expected for progressive melting by 5% increments for mantle peridotite at different sulfur contents (Pearson *et al.*, 2004). Primitive mantle values are off graph to the right. Dashed lines are the median values for global cratonic peridotite (Pearson *et al.*, 2004).

This geochemical signature is consistent with the significant melt depletion indicated by the mineral and whole rock chemistry of these rocks. Their  $(\text{Pt}/\text{Ir})_n$  values are also generally lower than median cratonic mantle and all but one samples are lower than chondritic. The CVI peridotites do not indicate quite the same level of melt depletion in their  $\text{Pd}/\text{Ir}$  ratios as the PP peridotites, but 14 of 18 samples have sub-chondritic  $(\text{Pd}/\text{Ir})_n$  and 9 of these samples have  $(\text{Pd}/\text{Ir})_n$  ratios close to, or below the median cratonic value. Similarly, over half the CVI

peridotites scatter around or have lower  $(\text{Pt}/\text{Ir})_{\text{n}}$  than the median value for cratonic peridotites. Hence, the highly siderophile element systematics of the CVI peridotites are also consistent with an origin via high levels of melt depletion.

#### ***4.2.3 Metasomatic disturbance of PGEs***

Some effects of metasomatic disturbance are evident in the PGE patterns of the CVI and PP peridotites, although these effects are perhaps less prominent than in many kimberlite-born xenolith suites. A few samples from both peridotite suites have  $(\text{Pt}/\text{Ir})_{\text{N}}$  and/or  $(\text{Pd}/\text{Ir})_{\text{N}}$  above unity (Fig. 4.9), at very low bulk rock  $\text{Al}_2\text{O}_3$  values, of around 1 wt% (Figure 4.8). At such low Al contents melting should have substantially lowered both Pt/Ir and Pd/Ir considerably and thus the suprachondritic ratios of these samples must reflect addition of P-PGEs via sulfide metasomatism, without significant enrichment in Al that would otherwise accompany a silicate melt enrichment event.

In the CVI peridotites, depleted Pt values in the normalized PGE patterns are accompanied by higher Pd and Re abundances indicating enrichment (Trends I and III). CVI Trend II PGEs have a significant Pd enrichment, resulting in  $\text{Pd} > \text{Ir}$ . Trend IV retains a much lower Pd signature with enriched Re. These post-depletion enrichments point to different events that have variably metasomatically influenced the mantle lithosphere beneath CVI. The fact that bulk rock Al remains low indicates that the enrichment processes involved either dominantly sulfide melt, or kimberlite. The very low bulk rock Al in uncontaminated primary

kimberlite melts (e.g., Kjarsgaard *et al.*, 2009) means that PGEs could be enriched with little effect on Al.

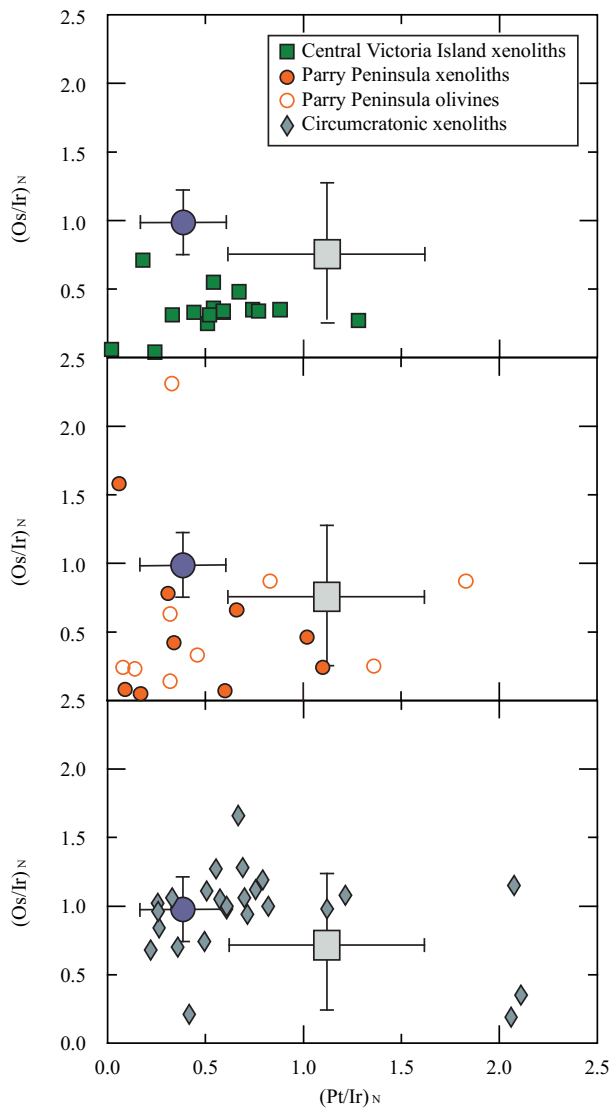


Figure 4.9  $(\text{Os/Ir})_N$  versus  $(\text{Pt/Ir})_N$  for central Victoria Island, Parry Peninsula and circum-cratonic peridotites. Circum-cratonic data from Aulbach *et al.* (in press). Circle with error bars represents the mean and 1SD for cratonic peridotites; square with error bars represents the mean and 1SD for off-craton peridotites.

PP whole rock peridotites have positive Re kinks, but show considerably lower degrees of Pd enrichment when compared to CVI.

How does this metasomatism affect Os isotope ratios? The group of very low Pd/Ir normalized ratios of PP whole rocks and olivines at relatively constant Os isotope ratios (Figure 4.10) and at varying but sub-chondritic Pt/Ir indicates that this data trend is dominated by depletion with perhaps elevation of Pt/Ir due to metasomatism in the samples with Pt/Ir >0.5. Alternatively, the relatively high Pt/Ir, at very low Pd/Ir and low Al, could result from Pt-alloy saturation right through the melting interval of these peridotites.

In contrast, the CVI P-PGE/I-PGE versus Os isotope trends show both depletion and metasomatic trends. The sub-horizontal trend of variable Pd/Ir and Pt/Ir at relatively constant  $^{187}\text{Os}/^{188}\text{Os}$  (Figure 4.10), could be due to depletion lowering Pd/Ir such that at Pd/Ir values of ~0.5, there is virtually no Re remaining and hence  $T_{RD} \sim T_{MA}$ . Above normalized Pd/Ir and Pt/Ir ratios of ~ 0.5 the CVI trends tend to increase in  $^{187}\text{Os}/^{188}\text{Os}$  indicating coeval addition of radiogenic Os, or at least the introduction of Re followed by in-growth of radiogenic Os. These trends are consistent with the addition of kimberlitic-related metasomatic agents into residues circa 2 Ga old, close to the Jurassic age of kimberlite eruption.

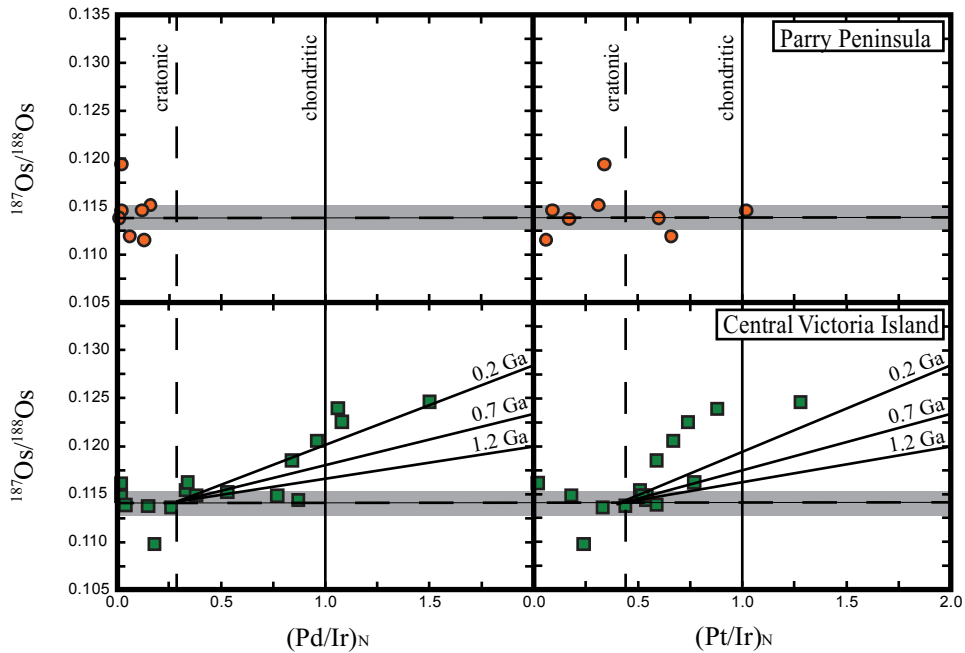


Figure 4.10 Variation of  $^{187}\text{Os}/^{188}\text{Os}$  isotopic ratios with  $(\text{Pd}/\text{Ir})_{\text{N}}$  and  $(\text{Pt}/\text{Ir})_{\text{N}}$ . Low PGE ratios indicate high degrees of depletion. The dashed horizontal line indicates the  $^{187}\text{Os}/^{188}\text{Os}$  ratio related to a 2.0 Ga formation event with the field representing normal mantle heterogeneity. Vertical dashed lines indicate median values for cratonic peridotites in normalized Pd/Ir and Pt/Ir space (Pearson *et al.*, 2004 and Aulbach *et al.*, in press). Inclined trends in CVI peridotites are likely the result of metasomatism and late alteration. Expected trends of alteration of 2.0 Ga cratonic lithosphere by events at 1.2 Ga, 0.7 Ga and 0.2 Ga (Mackenzie age, Franklin age, and kimberlite age; respectively).

### 4.3 Depletion Age and Lithosphere Formation in the Context of Regional Geology

The above discussion indicates that the highly siderophile element systematics of the PP peridotites and a significant part of the CVI peridotites are dominated by melt depletion. This means that the timing of melt depletion should be reflected in the Os isotope ratios at the large melt-fractions necessary to generate the

refractory bulk Al and olivine compositions of these peridotite suites (Figure 4.5). Nonetheless, because of the apparent Re enrichments evident in the normalized PGE patterns in both suites, we choose to use the  $T_{RD}$  age, which although a minimum age, should be close to the actual melting age for large melt-fraction residues, so long as the Re-enrichment was relatively recent (Figure 4.11).

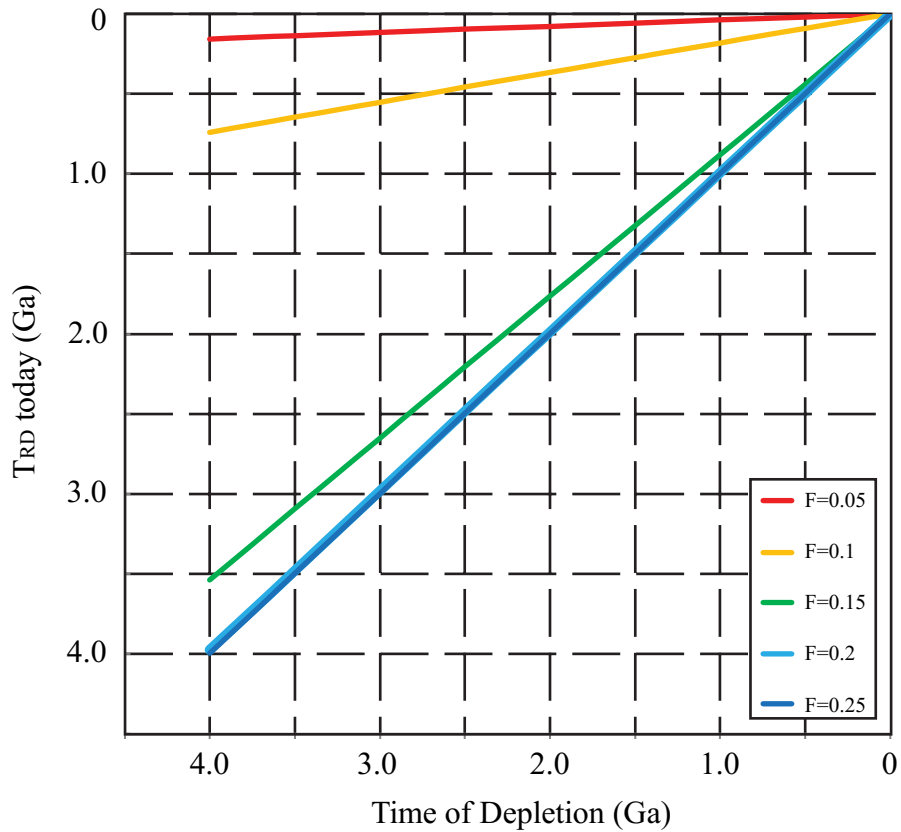


Figure 4.11 Calculated  $T_{RD}$  model age versus actual age of melting for varying degrees of melt removal from peridotite starting with Primitive Upper Mantle (PUM) – like composition. Model age lines diverge from 1:1 time lines when melting extents diverge from those necessary to quantitatively remove Re from the melting residue. Re depletion versus melt fraction derived from melt modeling presented in Aulbach *et al.* (in press). Figure modified from Czas *et al.* (in prep). Samples with > 25% melt removal produce  $T_{RD}$  ages that are indistinguishable from the actual melting age.

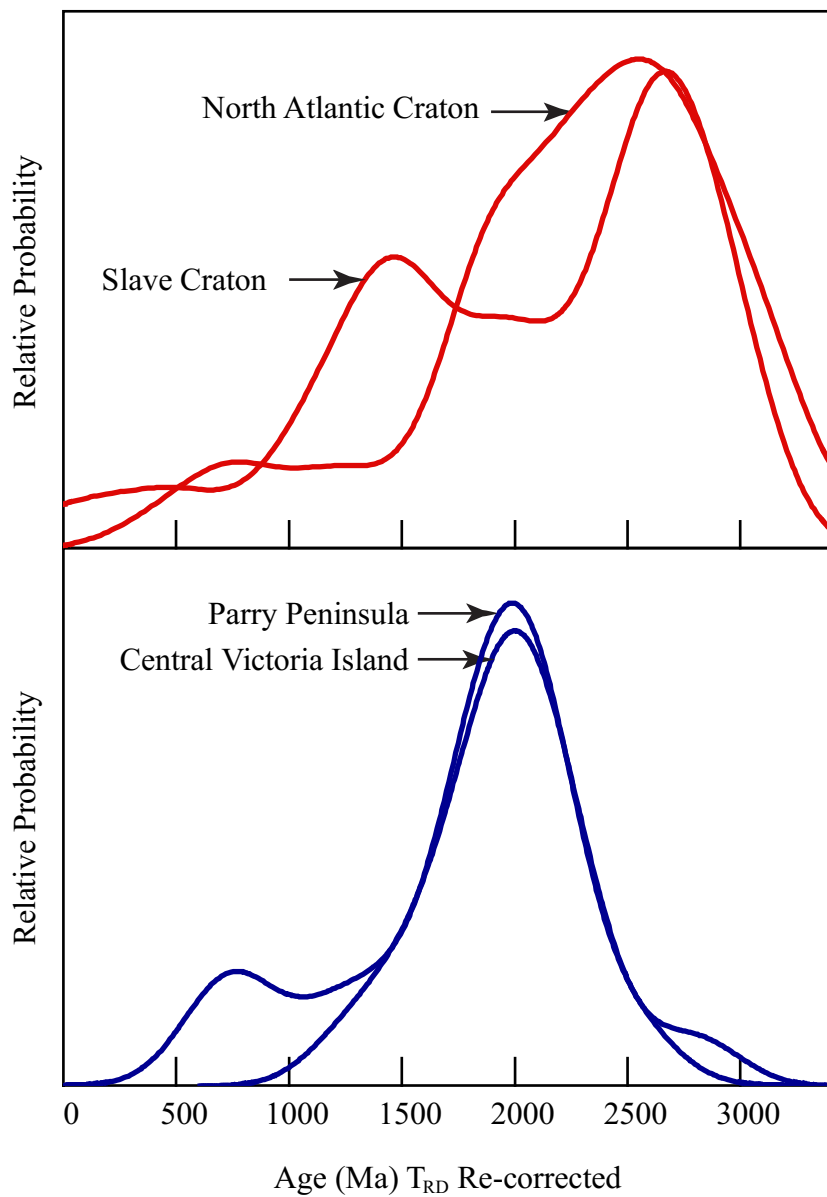


Figure 4.12 Probability density plot for  $T_{RD}$  model ages of central Victoria Island and Parry Peninsula peridotites using a uniform bandwidth of 0.2Ga, compared to the North Atlantic Craton (NAC) and the Slave Craton (Wittig *et al.*, 2010; Mather, 2012). Numbers of sample for NAC=127, Slave Craton=105, PP=15, CVI=15.

As such, the age of depletion should equate to the age of the formation of lithospheric mantle beneath the two regions being considered, because in both cases, the melt-fraction extracted was clearly large.

The PP peridotite whole rock  $T_{RD}$  model ages cluster between  $\sim$ 1700 and 2400 Ma with one higher measurement ( $\sim$ 2800) that could reflect mantle heterogeneity at the time of melting. The olivines show similar maximum ages but include a few younger ages ( $\sim$ 1280 to 2300 Ma). There is a very clear mode in the distribution of ages at  $\sim$  2 Ga (Figure 4.12).

The CVI peridotite  $T_{RD}$  model ages vary from  $\sim$ 700 to 2200 Ma, with a pronounced mode that is identical in age ( $\sim$ 2 Ga) to the PP peridotites. No systematic age-depth relations are observed if ages are mapped on to depths estimated from extrapolation to garnet Ni temperatures to a geotherm (See Appendix A8). From the arguments detailed above, such clustered Re depletion ages in highly depleted rocks indicate that the main lithosphere-forming event in the PP and CVI sample suites occurred at circa 2 Ga. Because of the imprecision in our knowledge of the mantle Os evolution curve, the uncertainty on this age is  $\sim$  0.2 Ga, so in term of the regional geology of the NWT and Nunavut, the age modes broadly overlap the 2.4 to 2.1 Ga crustal Nd model ages in the Wopmay orogeny (Bowring & Podosek, 1989) as well as the events of the main Wopmay orogeny (1.91 -1.85 Ga), collision of the Hottah arc terranes ( $\sim$ 1.91 Ga) and subsequent Great Bear arc evolution (1.88-1.86Ga; Hoffman, 1989). All of these events are related to lateral accretion. It is possible that the highly depleted bulk rock compositions developed during mantle melting associated with hydrous metasomatism in any of the various arc systems, as has been suggested for some Archean lithosphere (e.g., Simon *et al.*, 2007; Pearson & Wittig, 2008). The

melting products of these events are no longer evident in the geological record. The Wopmay orogeny is a distinct major crustal event in the region (1.89-1.84Ga; Cook, 2011) and the magmatic products may be hidden at depth.

The first-order implications of the age modes for both these regions are that:

- i) there was essentially no extant Archean lithosphere mantle beneath either area at the time of kimberlite eruption in the Jurassic;
- ii) the lithosphere beneath the Parry Peninsula, as represented by the xenoliths we analyzed, shows no evidence of a cratonic origin, hence the “Mackenzie Craton” hypothesized by some on the basis of diamondiferous kimberlites alone (e.g., Davies & Davies, 2103) is not substantiated. Nor do the new data substantiate the claim that the mantle beneath the PP may be a portion of Slave cratonic mantle, laterally offset hundreds of km to the NW (Davies & Davies, 2013). The diamondiferous mantle must be of younger age;
- iii) while there may be minor evidence for Archean crust in central Victoria Island, there is no clear evidence for Archean lithosphere and at least, meaning that the mantle beneath this region is unlikely to be a northerly extension of the Slave craton (e.g., Bleeker, 2003). More likely, the mantle beneath central Victoria Island could be a northeasterly extension of the depleted mantle produced during the Wopmay/Great Bear arc activity.

There are a number of younger Re depletion ages, primarily associated with the samples showing elevated Pd/Ir and Pt/Ir in both regions. These ages are in the

range of 700-1500Ma. The three youngest peridotites display garnet REE patterns that are distinct from the rest of the suite (Trend IIIb- moderately enriched LEE) and peak at ~800Ma. These ages most likely represent lithospheric disturbances during the major basaltic magmatism associated with the Mackenzie (1.27 Ga; LeCheminant & Heaman, 1989) and Franklin (723 Ma; Heaman *et al.*, 1992) LIP events and the ages are mixtures of new, more radiogenic Os introduced at that time along with depleted 2 Ga osmium signatures from the pre-existing lithosphere.

The highly depleted bulk compositions of both CVI and PP peridotite suites, that were apparently generated at 2 Ga, demonstrate that the Archean is not the only period in Earth history that saw the generation of highly depleted melt residues. The PP peridotite suite, which shows much less disturbed bulk compositions than the CVI suite, is more similar to the olivine-rich highly refractory compositions of the North Atlantic craton exemplified by peridotite xenoliths from West and East Greenland (Figure 4.13).

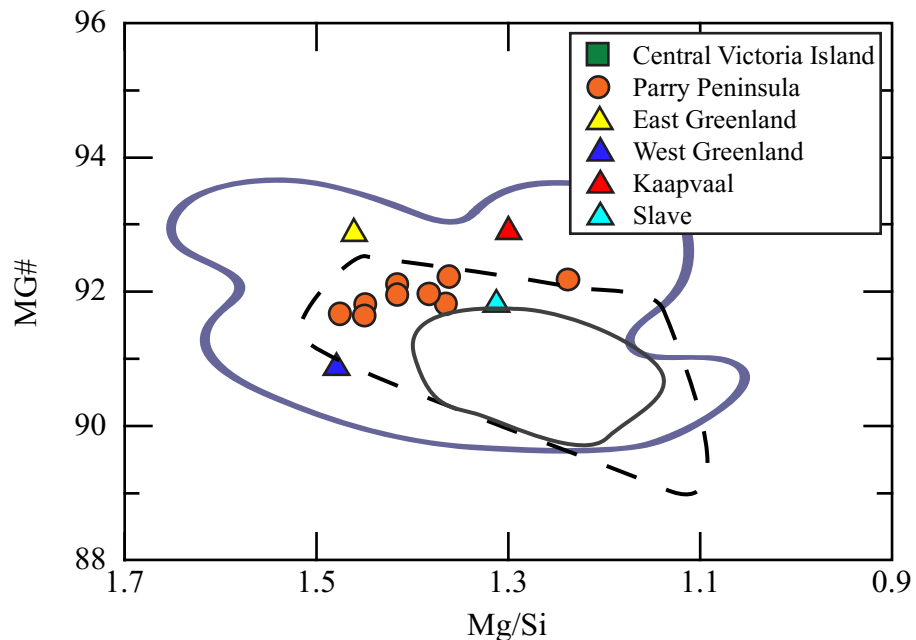


Figure 4.13 Whole rock MG# versus Mg/Si ratios. The blue line outlines cratonic values (compiled from Pearson *et al.*, 2004), dashed line outlines Somerset Island values (Pearson *et al.*, 2004) and grey line outlines Namibian values (Boyd *et al.*, 2004). PP Mg/Si increases towards East and West Greenland compositions with a MG# between the two terranes. Mg/Si is used to assess the volume of orthopyroxene present in the peridotite. PP displays consistently higher MG# than circum-cratonic lithosphere from South Africa and Somerset Island.

#### 4.4 Thermal Structure of the Lithosphere and Diamond Potential of the Parry Peninsula and Central Victoria Island

Diamond-bearing kimberlites, containing macro-diamonds to 0.74 carat have been found in the central Victoria Island kimberlite field (Diamonds North press statement, <http://www.marketwired.com/press-release/DIAMONDS-NORTH-Shifts-Focus-on-Victoria-Island-577294.htm>). In addition, diamonds have been found in till samples from the Parry Peninsula and are interpreted to be proximally derived (<http://www.darnleybay.com/projects/default.htm>) and

kimberlites have been drilled which yielded the peridotite xenoliths for this study. Hence, diamonds appear to be present at depth in the lithosphere beneath both regions, raising questions about the thermal structure of their lithospheric roots at the time of kimberlite eruption. The lithospheric mantle beneath Parry Peninsula and central Victoria Island is shown to be likely of Paleoproterozoic age, rather than Archean. While it has been widely accepted that there are thermal differences between cratonic and circum-cratonic lithosphere in the South African Kaapvaal craton and surrounding mobile belts (MacGregor, 1975; Boyd & Gurney, 1986), more recent work has shown that in fact the mantle geotherms until close to the time of kimberlite eruption were broadly similar on and around the craton (Boyd *et al.*, 2004; Mather *et al.*, 2011; Janney *et al.*, 2011). The main difference in the xenolith-derived geotherms in southern Africa seems to be recent evidence for thinning associated with a localized basal thermal disturbance that did not have time to re-equilibrate the shallower portions of the mantle geotherm.

Hasterok & Chapman (2011) recognize these typical higher temperatures can be applied to the Wopmay orogeny, whose mantle may underlie both the regions we have studied; however, they suggest the high observed crustal heat flow is balanced by a high heat generation within the crust and, that as such, the mantle beneath the Wopmay terrane is probably more consistent with a shield geotherm. This conclusion is validated by the discussion below.

#### ***4.4.1 Central Victoria Island***

CVI concentrate data is dominated by lherzolitic garnets but has a significant number of harzburgitic and eclogitic garnet mantle sources as well (Figure 3.9). CVI concentrate grain analyses indicate greater sampling of garnets from both higher and lower temperatures when compared to the xenolith suite (Figure 3.14, Figure 4.14), but with the same temperature mode as the garnets from xenoliths at ~1050°C, indicating the bulk of kimberlite is sampling a similar region of the lithosphere, but with a greater depth range. This main sampling mode, when projected to depth, is within the diamond stability field and extending to depths of at least 180 km (Figure 3.14), explaining the occurrence of diamonds within the Victoria Island kimberlites. The available clinopyroxene data on which the geotherm is modeled, indicates the presence of a deep cool craton-like geotherm beneath this region in the Jurassic, albeit one existing in Paleoproterozoic mantle. This geotherm had clearly relaxed from any potential thermal disturbance associated with the Mackenzie and Franklin LIP events at 1.27 Ga and 723 Ma, consistent with a thermal time-constant for thick lithospheric mantle of only two- to three hundred Ma (Jaupart & Marechal, 2011). This low level of disturbance is also indicated by the relative scarcity of Mackenzie and Franklin ages in the Os isotope signatures.

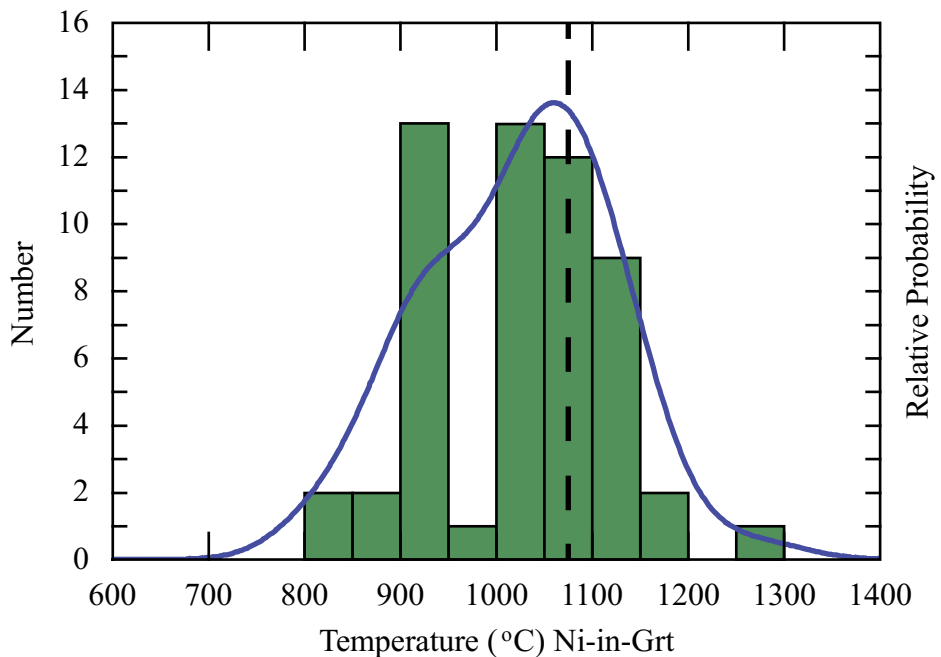


Figure 4.14 Probability density diagram of Ni-in-garnet temperatures for garnet till concentrate from central Victoria Island. Pdf bin size=50°C. The dashed line represents the median value of central Victoria Island xenolith garnets.

On a local scale, clinopyroxene till concentrate collected from different kimberlites on Victoria Island indicates a marked evolution of deeper lithosphere in the northern portion of Victoria Island that thins to the south (Figure A5.1).

#### 4.4.2 Parry Peninsula

The preservation of various silicate minerals and textures in the fresh PP xenolith suite provides more robust geothermobarometry constraints for the xenoliths than that available for CVI. However, PP xenoliths appear to be relatively shallow in origin (~75-100 km), from a restricted depth zone, with textural features common in samples equilibrating at or near the garnet-spinel transition zone. This phase transition will be deepened in such very depleted rocks because of the higher bulk

Cr-number extending the stability field of Cr-spinel relative to garnet. More meaningful data can be gleaned from the PP clinopyroxene concentrate data, which shows three clusters in P-T space that may indicate zones of continental lithospheric mantle beneath Parry Peninsula at depths greater than those recorded by the xenoliths. These grains indicate lithospheric mantle extending well into the diamond stability field, slightly warmer than the central Victoria Island mantle. This observation agrees with the finding of diamonds in multiple pipes by Darnley Bay Resources and indicates diamondiferous source material beneath at least a portion of Parry Peninsula.

Both localities, well away from the boundaries of any cratons, are clearly underlain by mantle with significant diamond potential, despite the Paleoproterozoic age of the mantle lithosphere. Observation of their garnet chemistry on a Ca-Cr plot indicates rather little lithosphere being sampled that is of the G10D composition (Figure 3.9, Figure 3.10), thought to be most prospective for harzburgitic diamonds (Gurney, 1984). However, it should be noted that the major Cullinan diamond deposit on the Kaapvaal craton has a dominantly Paleoproterozoic mantle (Carlson *et al.*, 1999) and diamonds of either lherzolitic or eclogitic paragenesis.

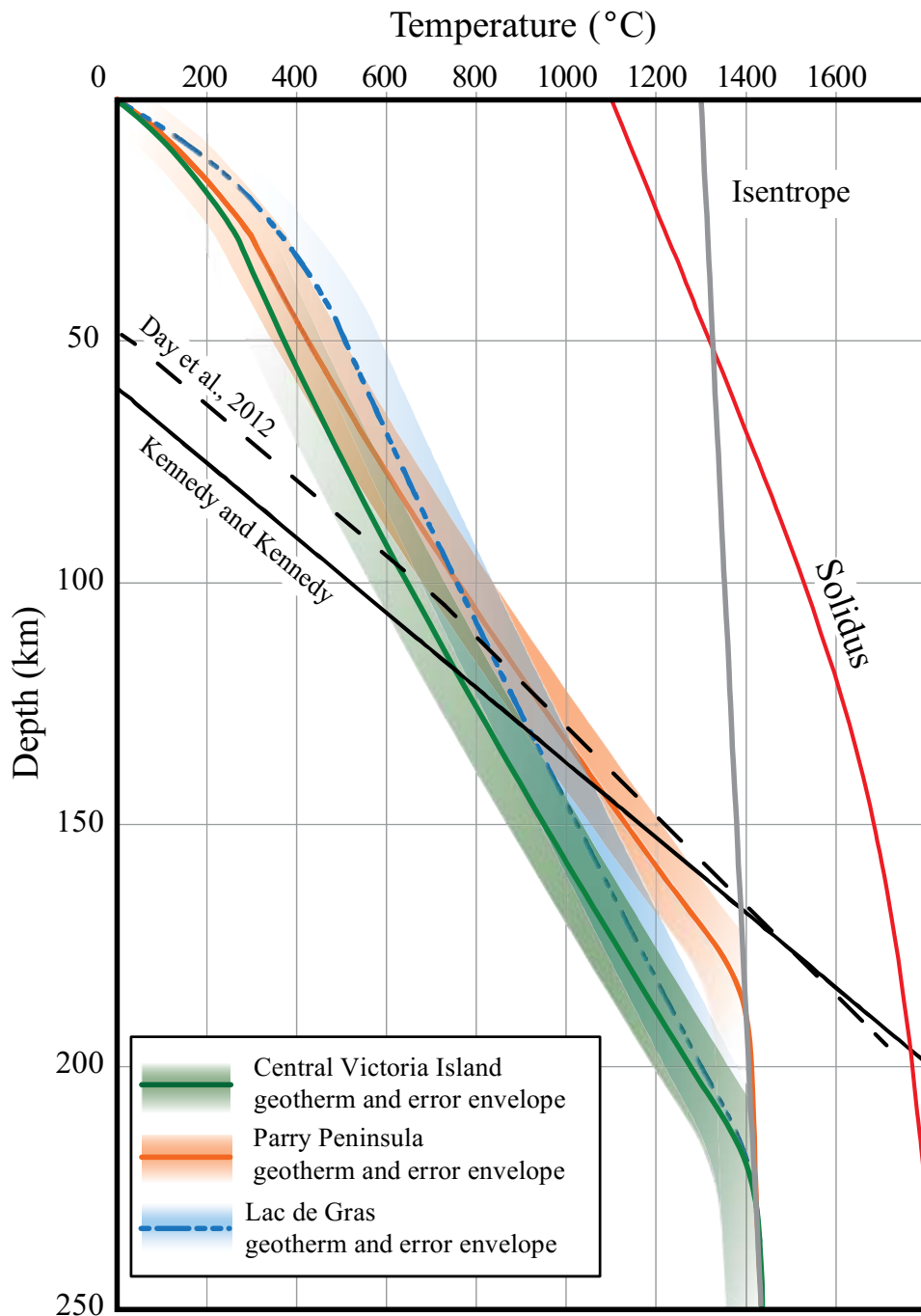


Figure 4.15 FITPLOT (Mather *et al.*, 2011) geotherms using xenoliths from Central Victoria Island, Parry Peninsula and Lac de Gras. CVI data projects a steep geotherm with lithosphere >125km that is potentially diamond stable. The geotherm at PP is much shallower, suggesting that the lithosphere is <150km thick and has less diamond potential. However, a geotherm derived from clinopyroxene concentrate is steeper than that of the xenoliths and (Appendix A5).

## CHAPTER 5: Conclusions

The relatively fresh peridotites from the Parry Peninsula have mineral chemical (high olivine MG# ~ 92.5) and bulk rock (very low bulk Al<sub>2</sub>O<sub>3</sub> contents) that are consistent with the presence of highly depleted peridotite beneath the region, similar in geochemical character to typical cratonic peridotites. Strong alteration of the Victoria Island peridotite xenoliths precludes olivine analysis but bulk rock compositions also show Al<sub>2</sub>O<sub>3</sub> contents (< 1wt%) consistent with significant melt depletion, hinting at the possible presence of cratonic mantle.

Geotherms constructed from single clinopyroxene thermobarometry on xenoliths and concentrate grains confirm that the lithospheric root in both locations extends into the diamond stability field (Central Victoria Island 120-215km; Parry Peninsula = 145-185km), consistent with the presence of diamonds in kimberlites from both areas.

Coupled Re-Os isotope and PGE analyses of 8 peridotites from the Parry Peninsula and 17 from Victoria Island reveal no compelling evidence for an Archean age for the mantle lithosphere beneath either locations. Instead, prominent modes in the Re depletion ages reveal the influence of a circa 2.0 Ga mantle event during the formation of mantle lithosphere at both locations. In both peridotite suites, the samples with circa 2 Ga (+/- 0.2 Ga) Re-depletion ages have very low Pd/Ir and Pt/Ir, indicative of extreme melt depletion freezing in the Os

isotopic composition at this time. Trends to higher Pt/Ir and Pd/Ir and more radiogenic Os isotopic compositions probably reflect metasomatic disturbance of the Re-Os system rather than melt depletion because bulk rock Al and olivine MG# do not co-vary, as would be expected for melt depletion trends.

Surprisingly, there is little direct indication of the affects of the 1.27 Ga Mackenzie large igneous event in the mantle at either location. A minor Franklin over-print is evident in Central Victoria Island.

Some Parry Peninsula peridotites hint at slightly older (~2.3-2.5 Ga) ages that overlap with the Arrowsmith orogeny and Hottah Terrane ages. Other samples at that location, and the majority of the Central Victoria Island samples are more broadly coincident with the arc-like magmatism in the 1.88 to 1.86 Ga Great Bear Arc sequence. The age data suggest that the bulk of the lithospheric mantle beneath these two regions is post-Archean, forming between ~2.3 and 1.8 Ga, probably during the Great-Bear Arc/Wopmay event. The mantle beneath Central Victoria Island may be a northeasterly continuation of depleted lithosphere produced by water-fluxed melting during the Wopmay orogeny. Due to the extreme melt fraction, traditional arc signatures are removed in the residue.

The presence of a diamondiferous mantle root that was generated largely in the Paleoproterozoic era is part of the growing body of evidence for diamond generation in mantle roots stabilized after the Archean.

## **5.1 Future Work**

### ***5.1.1 Central Victoria Island***

As this study utilized approximately half of xenolith samples recovered from the Snowy Owl kimberlite, analysis of the complete collection may provide either new insights in to the region or support and confirm the conclusions drawn in this study. In particular, as sample sizes are relatively small for the remainder of the samples, acquiring 1g of sample for isotopic analysis is likely impractical. As such those samples could be used to extend the petrographic characterization of the xenoliths, as well as increase the population size of Ni measurements for thermometry.

Recent seismic studies (eg. Shaeffer & Lebodev, 2015) suggest that Central Victoria Island may be underpinned by some of the thickest lithospheric mantle in all of North America. Our preliminary geotherm results indicate that the lithosphere here is no thicker than that beneath the Central Slave craton (Figure 4.15). Increasing the P-T constraints with more analyses of grains covering an extended P-T range will help to better define the geotherms. Both the FITPLOT geotherm approach and the large-scale seismic tomography rely on a good understanding of the crustal heat production and thickness in a given area. Neither of these factors are as well constrained as we might like. New small-scale seismic

studies to better understand the thickness and composition of the crust will greatly aid the refinement of mantle thickness estimates in this area.

Xenolith samples recovered with fresh silicates (olivine, clinopyroxene, orthopyroxene) would constrain a much more accurate geotherm through multiple geothermobarometers, along with providing more information on mantle conditions through olivine MG#, olivine Ca concentrations etc. Additionally samples collected from the northern kimberlite trends would be more likely to sample greater depths as indicated by concentrate collected in these areas, and would provide a broader understanding of the SCLM beneath Victoria Island. Sampling the mantle over greater depths with xenoliths would allow the construction of a lithospheric stratigraphy and compositional profile that could be compared to the layered structure of the Central Slave craton.

### ***5.1.2 Parry Peninsula***

PP xenolith samples for this study come from the shallow spinel-garnet transition zone of the lithospheric mantle. Clinopyroxene concentrate data, along with the occurrence of diamonds, supports the presence of a much deeper mantle source. Recovery of xenolith peridotites for greater depths, to allow more accurate geotherm estimation, would be very important for evaluation of the property as a diamond reserve.

Additional samples with the presence of garnet would significantly contribute to the understanding of the composition of the SCLM. Garnet chemistry would indicate if the mantle is lherzolite or harzburgite rich, as well as confirm diamond potential.

Concentrate mineral data collected at drill target sites in 2009 will become publicly available in 2019 and will greatly expand the dataset for the area.

Additional samples from the Parry Peninsula area as well as from the Dharma kimberlite to the West, would assist in better mapping of the lithospheric mantle and addressing the question of whether the Hottah and Wopmay terranes are the products of “thin-skinned” tectonic thrusting of Proterozoic crust over Archean lithosphere, or whether there was a significant generation of deep mantle lithosphere in the Paleoproterozoic, as the data from this thesis indicates.

## References

- Ackermann, S., Kunz, M., Armbruster, T., Schefer, J., and Hanni, H., 2005, Cation distribution in a Fe-bearing K-feldspar from Itrongay, Madagascar. A combined neutron- and X-ray single crystal diffraction study: Lawrence Berkeley National Laboratory.
- Armstrong, J.T., 1995, A package of correction programs for the Quantitative electron microbeam X-ray analysis of thick polished materials, thin films, and particles: Microbeam Analysis, v. 4, p. 177-200.
- Aulbach, S., Mungall, J., and Pearson, D.G., *in press*, Distribution and processing of highly siderophile elements in cratonic mantle lithosphere: Reviews in Geochemistry and Mineralogy.
- Baragar, W.R.A., Ernst, R.E., Hulbert, L., and Peterson, T., 1996, Longitudinal geochemical variation in the Mackenzie dyke swarm, Northwestern Canadian shield: Journal of Petrology, v. 37, p. 317-359.
- Barnes, S.J., and Roeder, P.L., 2001, The range of spinel compositions in terrestrial mafic and ultramafic rocks: Journal of Petrology, v. 42, p. 2279-2302.
- Bleeker, W., 2003, The late Archean record: a puzzle in ca. 35 pieces: Lithos, v. 71, p. 99-134.
- Boone, G.M., and Fernandez, L.A., 1971, Phenocrystic olivines from the eastern Azores: Mineralogical Magazine, v. 38, p. 165-78.
- Bowring, S.A., and Podosek, F.A., 1989, Nd isotopic evidence from Wopmay Orogen for 2.0-2.4 Ga crust in western North America: Earth and Planetary Science Letters, v. 94, p. 217-230.
- Boyd, F.R., and Gurney, J.J., 1986, Diamonds and the African lithosphere: Science, v. 232, p. 472-477.
- Boyd, F.R., and Mertzman, S.A., 1987, Composition and structure of the Kaapvaal lithosphere, southern Africa, *in* Mysen, B.O., ed., Magmatic Processes: Physicochemical Principles: University Park, PA The Geochemical Society.
- Boyd, F.R., Pearson, D.G., Hoal, B.G., Nixon, P.H., Kingston, M.J., and Mertzman, S.A., 2004, Garnet lherzolites from Louwrensia, Namibia: bulk composition and P/T relations: Lithos, v. 77, p. 573-592.

- Burgess, S.R., and Harte, B., 2004, Tracing lithospheric evolution through the analysis of heterogeneous G9/G10 garnets in peridotite xenoliths II: REE Chemistry: *Journal of Petrology*, v. 45, p. 609-633.
- Campbell, F.H.A., 1981, Stratigraphy and tectono-depositional relationships of the Proterozoic rocks of Hadley Bay, Northern Victoria Island, district of Franklin, Current Research, Volume Paper 81-1A, Geological Survey of Canada, p. 15-22.
- Canil, D., 1999, The Ni-in-garnet geothermometer: calibration at natural abundances: *Contributions to Mineral Petrology*, v. 136, p. 240-246.
- , 2004, Mildly incompatible elements in peridotites and the origins of mantle lithosphere: *Lithos*, v. 77, p. 375-393.
- Carlson, R.W., Pearson, D.G., Boyd, F.R., Shirey, S.B., Irvine, G., Menzies, A.H., and Gurney, J.J., 1999, Re-Os systematics of lithosphere peridotites: implications for lithospheric formation and preservation, *in* Gurney, J.J., Gurney, J.L., Pascoe, M.D., and Richardson, S.H., eds., Proceedings of the Seventh International Kimberlite Conference: Cape Town, South Africa, Red Roof Design, p. 99-108.
- Cook, F.A., 2011, Multiple arc development in the Paleoproterozoic Wopmay Orogen, Northwest Canada, *in* Brown, D., and Ryan, P.D., eds., Arc-Continent Collision, Volume Frontiers in Earth Science, p. 403-427.
- Darnley Bay Resources Limited, 2013, Darnley Bay Resources Limited-Project History, <http://www.darnleybay.com/projects/default.htm>.
- Davies, R., and Davies, A.W., 2013, Zone of Anomalous Mantle, *in* Pearson, D.G., ed., Proceedings of 10th International Kimberlite Conference, Volume 2, Special Issue of the Journal of the Geological Society of India, p. 143-156. Diamonds North press statement, 2006, DIAMONDS NORTH Shifts Focus on Victoria Island, <http://www.marketwired.com/press-release/DIAMONDS-NORTH-Shifts-Focus-on-Victoria-Island-577294.htm>.
- Gregoire, M., Bell, D.R., and Le Roex, A.P., 2003, Garnet lherzolites from the Kaapvaal craton (South Africa): Trace Element evidence for a metasomatic history: *Journal of Petrology*, v. 44, p. 629-657.
- Griffin, W.L., Fisher, N.I., Friedman, J., Ryan, C.G., and O'Reilly, S.Y., 1999a, Cr-pyrope garnets in the lithospheric mantle : I. Compositional systematics and relations to tectonic settings: *Journal of Petrology*, v. 40, p. 679-704.

- Griffin, W.L., Shee, S.R., Ryan, C.G., Win, T.T., and Wyatt, B.A., 1999b, Harzburgite to lherzolite and back again: metasomatic processes in ultramafic xenoliths from Wesselton kimberlite, Kimberley, South Africa: Contributions to Mineral Petrology, v. 134, p. 232-250.
- Grutter, H., 2009, Pyroxene xenocryst geotherms: Techniques and application: Lithos, v. 112S, p. 1167-1178.
- Grutter, H., Gurney, J.J., Menzies, A.H., and Winter, F., 2004, An updated classification scheme for mantle-derived garnet, for use by diamond explorers: Lithos, v. 77, p. 841-857.
- Gurney, J.J., 1984, A correlation between garnets and diamonds, in Glover, J.E., and Harris, P.G., eds., Kimberlite occurrence and origins: a Basis for Conceptual Models in Exploration: University of Western Australia, Geology Department and University Extension, Publication 8, p. 143-166.
- Harte, B., 1977, Rock nomenclature with particular relation to deformation and recrystallization textures in olivine-bearing xenoliths: Journal of Geology, v. 85, p. 279-288.
- Hasterok, D., and Chapman, D.S., 2011, Heat production and geotherms for the continental lithosphere: Earth and Planetary Science Letters, v. 307, p. 59-70.
- Heaman, L.M., Kjarsgaard, B.A., and Creaser, R.A., 2003, The timing of kimberlite magmatism in North America: implications for global kimberlite genesis and diamond exploration: Lithos, v. 71, p. 153-184.
- Heaman, L.M., LeCheminant, A.N., and Rainbird, R.H., 1992, Nature and timing of the Franklin igneous events, Canada: Implications for a late Proterozoic mantle plume and the break-up of Laurentia: Earth and Planetary Science Letters, v. 109, p. 117-131.
- Herrmann, W., and Berry, R.F., 2002, MINSQ-a least squares spreadsheet method for calculating mineral proportions from whole rock major element analysis: Geochemistry: Exploration, Environment, Analysis, v. 2, p. 361-368.
- Hoffman, P.F., 1989, Precambrian geology and tectonic history of North America, The Geology of North America, Volume A The geology of North America- An overview, The Geological Society of America, p. 447-512.
- Hornal, R.W., Sobczak, L.W., Burke, W.E.F., and Stephens, L.E., 1970, Preliminary results of gravity surveys of the Mackenzie Basin and

Beaufort Sea, Gravity map surveys, Earth Physics, Department of Energy, Mines and Resources, Ottawa.

Irvine, G.J., Pearson, D.G., Kjarsgaard, B.A., Carlson, R.W., Kopylova, M.G., and Dreibus, G., 2003, A Re-Os isotope and PGE study of kimberlite-derived peridotite xenoliths from Somerset Island and a comparison to the Slave and Kaapvaal cratons: *Lithos*, v. 71, p. 461-488.

Jackson, V.A., van Breemen, O., Ootes, L., Bleeker, W., Bennett, V., Davis, W.J., Ketchum, J.W.F., and Smar, L., 2013, U-Pb zircon ages and field relationships of Archean basement and Proterozoic intrusions, south-central Wopmay Orogen, NWT: implications for tectonic assignments: *Canadian Journal of Earth Science*, v. 50, p. 979-1006.

Janney, P.E., Shirey, S.B., Carlson, R.W., Pearson, D.G., Bell, D.R., Le Roex, A.P., Ishikawa, A., Nixon, P.H., and Boyd, F.R., 2010, Age, composition and thermal characteristics of South African off-craton mantle lithosphere: Evidence for a multi-stage history: *Journal of Petrology*, v. 51, p. 1849-1890.

Jaroswich, E., 2002, Smithsonian microbeam standards: *Journal of Research of the National Institute of Standards and Technology*, v. 170, p. 681-685

Jaupart, C., and Marechal, J.-C., 2011, Heat Generation and Transport in the Earth: Cambridge, UK, Cambridge University Press, 477 p.

Kahlert, B., 2002, in Heaman, L.M., Kjarsgaard, B.A., and Creaser, R.A., 2003, The timing of kimberlite magmatism in North America: implications for global kimberlite genesis and diamond exploration: *Lithos*, v. 71, p. 153-184.

Kjarsgaard, B.A., Pearson, D.G., Tappe, S., Nowell, G.M., and Dowall, D.P., 2009, Geochemistry of hypabyssal kimberlites from Lac de Gras, Canada: Comparisons to a global database and applications to the parent magma problem: *Lithos*, v. 112S, p. 236-248.

Klein-BenDavid, O., and Pearson, D.G., 2009, Origins of subcalcic garnets and their relation to diamond forming fluids - Case studies from Ekati (NWT-Canada) and Murowa (Zimbabwe): *Geochimica et Cosmochimica Acta*, v. 73, p. 837-855.

Kohler, 1994, PTEXL program, University of Alberta.

Kolebaba, M., Read, G., Kahlert, B., and Kelsch, D., 2003, Diamondiferous kimberlites on Victoria Island, Canada, a northern extension of the Slave

Craton, 8th International Kimberlite Conference, Volume Extended  
Abstracts: Victoria, Canada, p. 308.

Kopylova, M.G., Russell, J.K., and Cookenboo, H., 1999, Petrology of Peridotite and Pyroxenite Xenoliths from the Jericho Kimberlite: Implications for the Thermal State of the Mantle beneath the Slave Craton, Northern Canada: Journal of Petrology, v. 40, p. 79-104.

LeCheminant, A.N., and Heaman, L.M., 1989, Mackenzie igneous events, Canada: Middle Proterozoic hotspot magmatism associated with ocean opening: Earth and Planetary Science Letters, v. 96, p. 38-48.

Liu, J., Scott, J.M., Matrin, C.E., and Pearson, D.G., 2015, The longevity of Archean mantle residues in the convecting upper mantle and their role in young continent formation: Earth and Planetary Science Letters, v. 424, p. 109-118.

Luguet, A., Jaques, A.L., Pearson, D.G., Smith, C.B., Bulanova, G.P., Roffey, S.L., Rayner, M.J., and Lorand, J.-P., 2009, An integrated petrological, geochemical and Re-Os isotope study of peridotite xenoliths from the Argyle lamproite, Western Australia and implications for cratonic diamonds: Lithos, v. 112 Supplement 2, p. 1096-1108.

Luguet, A., Nowell, G.M., and Pearson, D.G., 2008,  $^{184}\text{Os}/^{188}\text{Os}$  and  $^{186}\text{Os}/^{188}\text{Os}$  measurements by Negative Thermal Ionisation Mass Spectrometry (N-TIMS): Effects of interfering element and mass fractionation corrections on data accuracy and precision: Chemical Geology, v. 248, p. 342-362.

MacGregor, I.D., 1975, Petrologic and thermal structure of the upper mantle beneath South Africa in the Cretaceous: Physics and Chemistry of the Earth, v. 9.

Mather, K.A., 2012, A xenolith-based lithospheric transect of the Slave Craton, NWT, Canada, Durham University.

Mather, K.A., Pearson, D.G., McKenzie, D., Kjarsgaard, B.A., and Priestley, K., 2011, Constraints on the depth and thermal history of cratonic lithosphere from peridotite xenoliths, xenocrysts and seismology: Lithos, v. 125, p. 729-742.

McDonough, W.F., and Sun, S.S., 1995, The composition of the Earth: Chemical Geology, v. 120, p. 223-253.

Mungall, J.E., and Brennan, J.M., 2014, Partitioning of platinum-group elements and Au between sulfide liquid and basalt and the origins of mantle-crust

- formation of the chalcophile elements: *Geochimica et Cosmochimica Acta*, v. 125, p. 265-289.
- Nimis, T., and Taylor, W.R., 2000, Single-clinopyroxene Thermobarometry for garnet peridotites. Part I. Calibration and testing of a Cr-in-Cpx barometer and an enstatite-in-Cpx thermometer.: *Contributions to Mineral Petrology*, v. 139, p. 541-554.
- Ootes, L., Davis, W.J., Jackson, V.A., and Van Breemen, O., 2015, Chronostratigraphy of the Hottah terrane and Great Bear magmatic zone of Wopmay Orogen, Canada, and exploration of a terrane translation model: *Canadian Journal of Earth Science*, v. 52, p. 1062-1092.
- Pearson, D.G., Canil, D., and Shirey, S.B., 2003, 2.05 Mantle samples included in volcanic rocks: xenoliths and diamonds, *in* Holland, H.D., and Turekian, K.K., eds., *Treatise on Geochemistry* Oxford, Elsevier, p. 169-253.
- Pearson, D.G., Carlson, R.W., Shirey, S.B., Boyd, F.R., and Nixon, P.H., 1995, Stabilization of Archean lithospheric mantle: A Re-Os isotope study of peridotite xenoliths from the Kaapvaal craton: *Earth and Planetary Science Letters*, v. 134, p. 341-357.
- Pearson, D.G., Irving, G.J., Ionov, D.A., Boyd, F.R., and Dreibus, G., 2004, Re-Os isotope systematics and platinum group element fractionation during mantle melt extraction: a study of massif and xenolith peridotite suites: *Chemical Geology*, v. 208, p. 29-59.
- Pearson, D.G., Mather, K.A., Ishikawa, A., and Kjarsgaard, B.A., 2012, Origin and evolution of cratonic roots, *in* Pearson, D.G., ed., *Proceedings of 10th International Kimberlite Conference*: Bangalore, Special Issue of the *Journal of the Geological Society of India*.
- Pearson, D.G., and Wittig, N., 2008, Formation of Archaean continental lithosphere and its diamonds: the root of the problem: *Journal of the Geological Society*, London, v. 165, p. 895-914.
- , 2014, The formation and evolution of cratonic mantle lithosphere—Evidence from mantle xenoliths: *The Mantle and Core, Treatise on Geochemistry*, v. 3, p. 225-292.
- Pearson, D.G., and Woodland, S.J., 2000, Solvent extraction/anion exchange separation and determination of PGEs (Os, Ir,Pt, Pd, Ru) and Re-Os isotopes in geological samples by isotope dilution ICP-MS: *Chemical Geology*, v. 165, p. 87-107.

- Pilkington, M., and Saltus, R.W., 2009, The Mackenzie River magnetic anomaly, Yukon and Northwest Territories, Canada - evidence for Early Proterozoic magmatic arc crust at the edge of the North American craton: *Tectonophysics*, v. 478.
- Potts, P.J., 1992, A Handbook of Silicate Rock Analysis: New York City, New York, Springer.
- Rainbird, R.H., Jefferson, C.W., Hildebrand, R.S., and Worth, J.K., 1994, The Shaler Supergroup and revision of Neoproterozoic stratigraphy in the Amundsen Basin, Northwest Territories, Current Research 1994-C, Geological Survey of Canada, p. 61-70.
- Rainbird, R.H., LeCheminant, A.N., and Laywer, J.I., 1996, The Duke of York and related Neoproterozoic inliers of southern Victoria Island, District of Franklin, Northwest Territories, Current Research 1996-E, Geological Survey of Canada, p. 125-134.
- Ramsay, R.R., and Tompkins, L.A., 1994, The geology, heavy mineral concentrate mineralogy, and diamond prospectivity of the Boa Esperança and Cana Verde pipes, Corrego D'Anta, Minas Gerais, Brazil.: Companhia de Pesquisa de Recursos Minerais, v. CPRM Special Publication 1B Jan/94, p. 329–345.
- Reford, S.W., 2010, Exploring for minerals and diamonds at Darnley Bay, NT - A reality in 2010, Darnley Bay Resources Ltd.
- Rudnick, R.L., and Walker, R.J., 2009, Interpreting ages from Re-Os isotopes in peridotites: *Lithos*, v. 112, Supplement 2, p. 1083-1095.
- Schaeffer, A.J., and Lebedev, S., 2014, Imaging the North American continent using waveform inversion of global and USArray data: *Earth and Planetary Science Letters*, v. 402, p. 26-41.
- Shimizu, N., and Richardson, S.H., 1987, Trace element abundance patterns of garnet inclusions in peridotite-suite diamonds: *Geochimica et Cosmochimica Acta*, v. 21, p. 755-758.
- Simon, N.S.C., Carlson, R.W., Pearson, D.G., and Davies, G.R., 2007, The origin and evolution of Kaapvaal cratonic lithospheric mantle: *Journal of Petrology*, v. 48, p. 589-625.
- Simon, N.S.C., Irving, G.J., Davies, G.R., Pearson, D.G., and Carlson, R.W., 2003, The origin of garnet and clinopyroxene in “depleted” Kaapvaal peridotites: *Lithos*, v. 71, p. 289-322.

- Stacey, R.A., 1971, Interpretation of the gravity anomaly at Darnley Bay, N.W.T.: Canadian Journal of Earth Science, v. 8, p. 1037-1042.
- Stachel, T., Aulbach, S., Brey, G.P., Harris, J.W., Leost, I., Tappert, R., and Viljoen, K.S., 2004, The trace element composition of silicate inclusions in diamonds: a review: *Lithos*, v. 77, p. 1-19.
- Stachel, T., Viljoen, K.S., Brey, G., and Harris, J.W., 1998, Metasomatic processes in lherzolitic and harzburgitic domains of diamondiferous lithospheric mantle: REE in garnets from xenoliths and inclusions in diamonds: *Earth and Planetary Science Letters*, v. 159, p. 1-12.
- Tappe, S., Pearson, D.G., Kjarsgaard, B.A., Nowell, G.M., and Dowall, D.P., 2013, Mantle transition zone input to kimberlite magmatism near a subduction zone: origin of anomalous Nd–Hf isotope systematics at Lac de Gras, Canada: *Earth and Planetary Science Letters*, v. 371, p. 235-251.
- Thorsteinsson, R., and Tozer, E.T., 1962, Banks, Victoria and Stefansson Islands, Arctic Archipelago, Memoirs 330, Geological Survey of Canada, p. 85.
- Vielzeuf, D., Champenois, M., Valley, J.W., Brunet, F., and Devidal, J.L., 2005, SIMS analysis of oxygen isotopes: Matrix effects on Fe-Mg-Ca garnets: *Chemical Geology*, v. 223, p. 208-226.
- Walker, R.J., Carlson, R.W., Shirey, S.B., and Boyd, F.R., 1989, Os, Sr, Nd and Pb isotope systematics of southern African peridotite xenoliths: Implications for the chemical evolution of subcontinental mantle: *Geochimica et Cosmochimica Acta*, v. 53, p. 1583-1595.
- Wittig, N., Pearson, D.G., Webb, M., Ottley, C.J., Irvine, G.J., Kopylova, M.G., Jensen, S.M., and Nowell, G.M., 2008b, Origin of cratonic lithospheric mantle roots: a geochemical study from the North Atlantic craton, West Greenland: *Earth and Planetary Science Letters*, v. 274, p. 24-33.
- Yorath, C.J., Balkwill, T.P., and Klassen, R.W., 1968, Franklin Bay - Malloch Hill District of Mackenzie, Geological Survey of Canada.

## **APPENDICES**

<b>Appendix A1</b> Sample and Data Sources.....	<b>101</b>
<b>Appendix A2</b> Standards and Reproducibility.....	<b>105</b>
<b>Appendix A3</b> Petrography .....	<b>107</b>
<b>Appendix A4</b> Garnet Repeatability .....	<b>127</b>
<b>Appendix A5</b> Concentrate Data.....	<b>128</b>
<b>Appendix A6</b> Thermobarometry.....	<b>133</b>
<b>Appendix A7</b> Central Victoria Island mineral grain re-analysis ....	<b>138</b>
<b>Appendix A8</b> Model ages .....	<b>154</b>

## Appendix A1 Sample and Data Sources

Table A1.1 Central Victoria Island kimberlites UTM NAD83 zone 10

Kimberlite	Easting	Northing	Field	This Project
Apollo	562263	7863942	Blue Ice	
Arctic Tern	576926	7785359	Snowy Owl	
Blizzard	549261	7842159	King Eider	
Carina	537507	7822734	Galaxy	
Diana	562545	7863695	Blue Ice	
Fornax	538081	7822328	Galaxy	
GW	548553	7842871	King Eider	
<b>Golden Plover</b>	<b>570881</b>	<b>7788579</b>	<b>Snowy Owl</b>	<b>concentrate</b>
Gosling	531945	7826315	Galaxy	
H1	536100	7853810	King Eider	
Horned Lark	571283	7789200	Snowy Owl	
<b>King Eider</b>	<b>542127</b>	<b>7847540</b>	<b>King Eider</b>	<b>concentrate</b>
<b>Jaeger</b>	<b>535201</b>	<b>7854547</b>	<b>King Eider</b>	<b>concentrate</b>
Juno	543538	7847200	King Eider	
<b>Longspur</b>	<b>571421</b>	<b>7788167</b>	<b>Snowy Owl</b>	<b>concentrate</b>
Meister	537093	7852995	King Eider	
Neptune	562144	7864035	Blue Ice	
Orion	541751	7819858	Blue Ice	
Pegasus	542171	7820035	Galaxy	
<b>Phalarope</b>	<b>574796</b>	<b>7787739</b>	<b>Snowy Owl</b>	<b>concentrate</b>
<b>Pintail</b>	<b>536563</b>	<b>7853470</b>	<b>King Eider</b>	<b>concentrate</b>
Pluto	563337	7863280	Blue Ice	
Ptarmigan	575139	7786975	Snowy Owl	
Sanderling	543080	7848675	King Eider	
<b>Sandpiper</b>	<b>543770</b>	<b>7818862</b>	<b>Galaxy</b>	
Sculptor	542032	7819950	Galaxy	
SLT4	540729	7820581	Galaxy	
<b>Snowbunting</b>	<b>544983</b>	<b>7817896</b>	<b>Galaxy</b>	<b>concentrate</b>
<b>Snow Goose</b>	<b>531855</b>	<b>7826550</b>	<b>Galaxy</b>	<b>concentrate</b>
<b>Snowy Owl</b>	<b>570067</b>	<b>7789137</b>	<b>Snowy Owl</b>	<b>all SnO xenoliths</b>
South Piper Tail	544105	7818612	Galaxy	
<b>Turnstone</b>	<b>539640</b>	<b>7851674</b>	<b>King Eider</b>	<b>concentrate</b>
Vega	543448	7819022	Galaxy	
Vega West	542984	7819333	Galaxy	
Virgo	544423	7818272	Galaxy	
Whimbrel	566383	7792864	Snowy Owl	
Zeta	540411	7820620	Galaxy	



Figure A1.1 Location of kimberlites on Victoria Island. Each square represents a kimberlite. The black square is the Snowy Owl kimberlite.

Table A1.2 Parry Peninsula kimberlites UTM NAD83 zone 12,13

Kimberlite	Easting	Northing	This Project
MT9-02	438363	7722490	
MT10-01	444428	7723818	
MT10-03	444316	7723788	
MT10-04	444272	7723829	
<b>MT100-01</b>	<b>432016</b>	<b>7724461</b>	<b>concentrate</b>
<b>MT101-01</b>	<b>438482</b>	<b>7722235</b>	<b>concentrate</b>
MT101-02	432393	7707318	
MT101-03	431630	7723475	
MT101-04	431630	7723475	
MT101-05	431630	7723475	
MT101-06	431630	7723475	
MT101-07	431630	7723475	
MT101-08	431630	7723468	
MT101-09	431630	7723468	
<b>MT102-01</b>	<b>435635</b>	<b>7730555</b>	<b>DB7-DB11 xenoliths</b>
MT104-02	432786	7719892	
MT104-11	431669	7723462	
<b>MT105</b>	<b>436311</b>	<b>7723717</b>	<b>concentrate</b>
<b>MT105-01</b>	<b>436310</b>	<b>7723712</b>	<b>concentrate</b>
<b>MT105-02</b>	<b>436239</b>	<b>7723715</b>	<b>concentrate</b>
MT106-01	435447	7722825	
<b>MT107-01</b>	<b>435891</b>	<b>7722927</b>	<b>concentrate</b>
MT107-01	435875	7722999	
MT108-01	432815	7719943	
MT108-02	429616	7706186	
MT109-01	429590	7706247	
<b>MT112-01</b>	<b>433717</b>	<b>7712614</b>	<b>DB1-DB6 xenoliths</b>
MT113-01	441998	7722283	

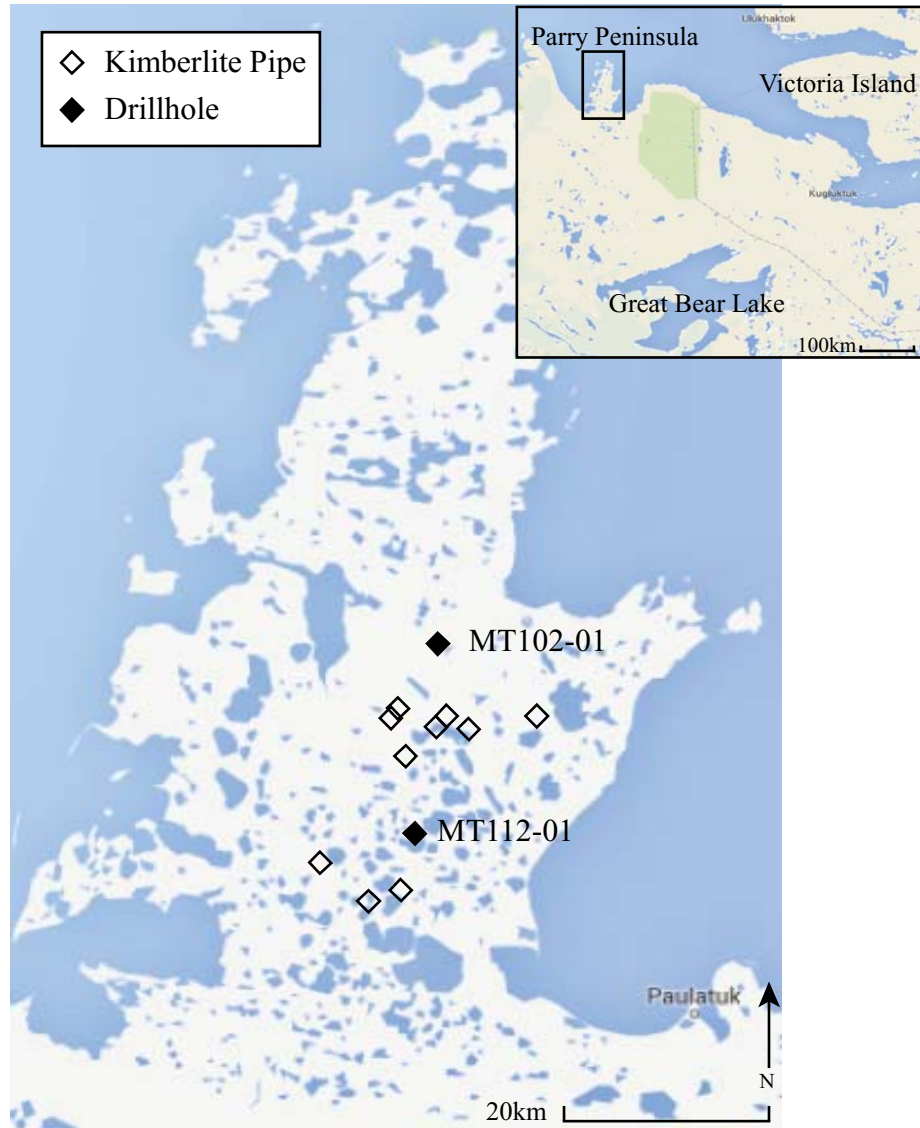


Figure A1.2 Location of kimberlites on Parry Peninsula. Black diamonds represent the locations of xenoliths from this study related to Table A1.2

## Appendix A2 Standards and Reproducibility

### ***Electron Microprobe***

Table A2.1 Standards used for calibration for both the Cameca and JEOL microprobe instruments.

Element	Standard	Locality	Reference
Na	Albite	Cazadero CA, USA	
Si,Mg,Ca	Diopside	Wakefield QC, Canada	
Fe	Fayalite	Rockport, MA, USA	Jarosewich, 2002
Mg	Fo93	Balsam Gap, NC, USA	Boone and Fernandez, 1971
Mg	Fo90	San Carlos, Gila County, NV, USA	Jarosewich, 2002
Al	FS Garnet	Frank Smith, South Africa	
Mn	Mn <sub>2</sub> O <sub>3</sub>	Synthetic	
Ni	Nickel wire	Synthetic	
Al	Pyrope	Kakanui, New Zealand	Jarosewich, 2002
Ti	Rutile	Synthetic	
V	V metal	Synthetic	
Al	Gore	Gore Mountain, NY, USA	Vielzeuf et al., 2005
Si,Mg,Ca	Kaersutite	Kakanui, New Zealand	Jarosewich, 2002
Si	Augite	Kakanui, New Zealand	Jarosewich, 2002
Fe	Hematite	Rio Marina mine, Elba	
Cr	Chromite	Tiebaghi Mine, New Caledonia	Jarosewich, 2002
K	Sanidine	Itrongay, Madagascar	Ackermann, 2005
Zn	Willemite	Franklin Furnace, NJ, USA	
Mn	Rhodonite	Franklin Furnace, NJ, USA	

Table A2.2 Microprobe counting times

Element	Counting Time (seconds)	
	Peak	Background
Si	15	30
Ti	25	50
Al	30	60
Cr	25	50
V	15	30
Fe	15	30
Mn	15	30
Mg	25	50
Ca	25	50
Ni	20	40
Na	30	60
K	30	60

### *Trace elements*

Table A2.3 Reproducibility of secondary standards at 2 standard deviations of the mean difference. BIR-1G is a glass, PN1 and PN2 well characterized natural garnet megacrysts.

	<b>BIR-1G</b>	<b>PN1</b>	<b>PN2</b>
<b>Ti</b>	0.10	0.03	0.02
<b>Ni60</b>	0.06	0.04	0.01
<b>Ni61</b>	0.07	0.05	0.01
<b>Sr</b>	0.04	0.10	0.09
<b>Y</b>	0.03	0.09	0.03
<b>Zr</b>	0.04	0.09	0.04
<b>Nb</b>	0.06	0.28	0.21
<b>Ba</b>	0.05	-	0.00
<b>La</b>	0.05	0.25	0.17
<b>Ce</b>	0.04	0.12	0.08
<b>Pr</b>	0.05	0.10	0.15
<b>Nd</b>	0.05	0.09	0.10
<b>Sm</b>	0.06	0.12	0.08
<b>Eu</b>	0.07	0.11	0.07
<b>Gd</b>	0.05	0.10	0.04
<b>Tb</b>	0.05	0.10	0.04
<b>Dy</b>	0.06	0.10	0.06
<b>Ho</b>	0.05	0.09	0.06
<b>Er</b>	0.06	0.14	0.05
<b>Tm</b>	0.09	0.18	0.05
<b>Yb</b>	0.06	0.24	0.06
<b>Lu</b>	0.06	0.28	0.07
<b>Hf</b>	0.09	0.10	0.08

## Appendix A3 Petrography

Table A3.1 - Central Victoria Island xenolith sample list with data capture

	Weight (g)	Thin Section	Mineral Separates (mounts)	XRF	Re-Os W/R	Garnet Trace Elements
<b>Central Victoria Island</b>						
SnO-1	9	Y			Y	
SnO-2	<1					
SnO-3	8					
SnO-4	<1					
SnO-5	23	Y			Y	
SnO-6	9					
SnO-7	7					
SnO-8	9					
SnO-9	5					
SnO-10	9					
SnO-11	7					Y
SnO-12	12		Y	Y	Y	Y
SnO-13	9					
SnO-14	50	Y		Y		
SnO-15	57		Y	Y	Y	Y
SnO-16	7	Y				
SnO-17	13		Y	Y	Y	Y
SnO-18	6					
SnO-19	20		Y	Y	Y	Y
SnO-20	38			Y	Y	Y
SnO-21	17			Y	Y	
SnO-22	6					
SnO-23	8		Y			Y
SnO-24	36		Y	Y	Y	Y
SnO-25	9		Y			
SnO-26	32		Y	Y	Y	Y
SnO-27	14		Y	Y	Y	
SnO-28	20		Y	Y	Y	Y
SnO-29	4		Y	Y		Y
SnO-30	<1					
SnO-31	5					
SnO-32	55		Y	Y	Y	Y
SnO-33	27		Y	Y	Y	Y
SnO-34	76	Y	Y	Y	Y	Y
SnO-35	23		Y	Y	Y	Y
SnO-36	16		Y	Y	Y	

Table A3.2 Parry Peninsula xenolith sample list with data capture

	Weight (g)	Thin Section	Mineral Separates (mounts)	XRF	Re-Os W/R	Re-Os Olivines
<b>Parry Peninsula</b>						
DB1A	302	Y	Y	Y	Y	Y
DB2D	90	Y	Y	Y	Y	Y
DB2E	8		Y			Y
DB3A	107		Y	Y	Y	Y
DB3C	28	Y			Y	
DB4B	160	Y	Y	Y	Y	Y
DB5A	3					
DB5C	47	Y	Y	Y	Y	Y
DB6A	49	Y	Y	Y	Y	Y
DB7A	6		Y			
DB8A	240	Y	Y	Y	Y	Y
DB9B	14	Y				
DB9C	21		Y			Y
DB10A	5		Y			
DB11A	25	Y		Y	Y	Y

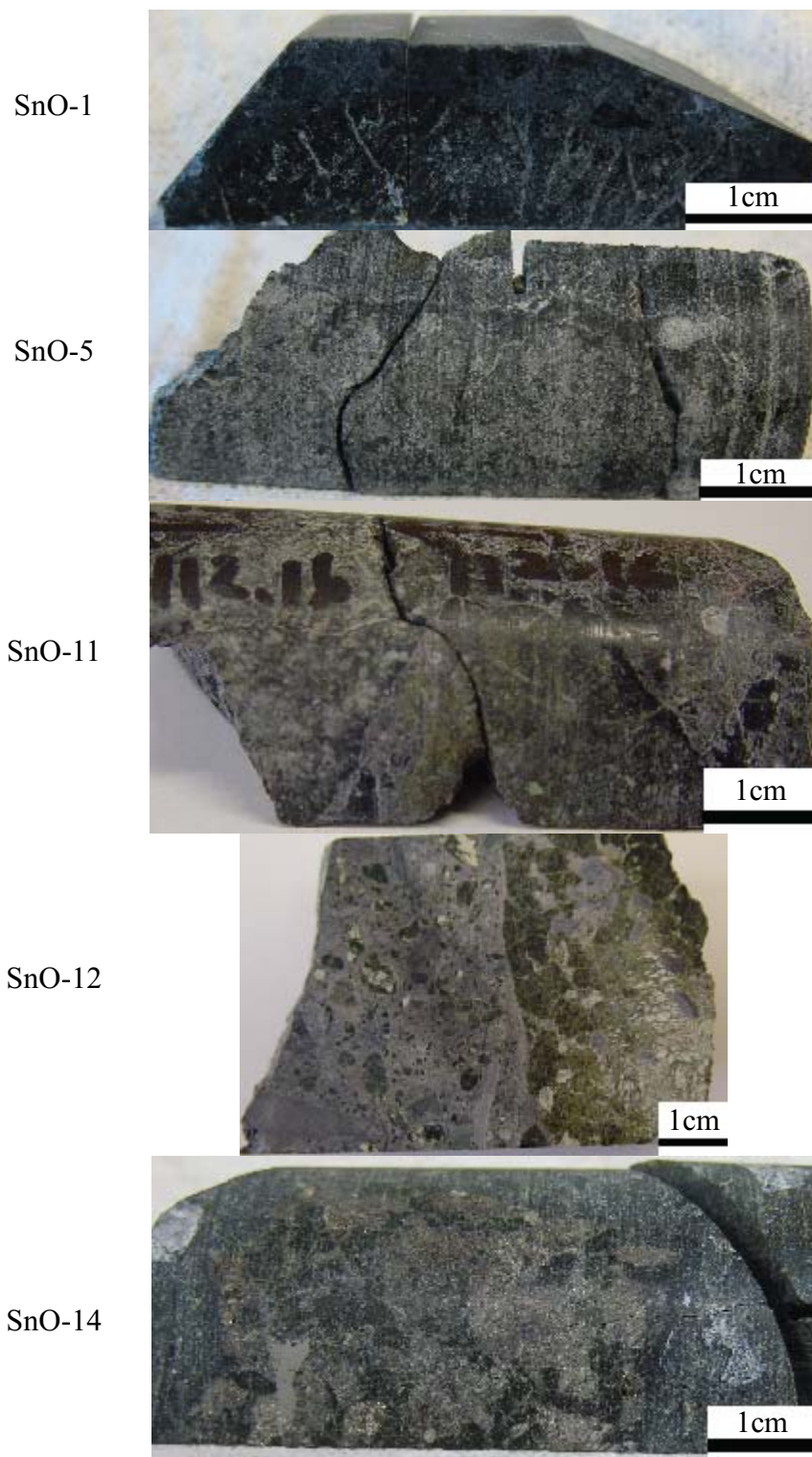


Figure A3.1 Hand sample images of central Victoria Island xenoliths in core

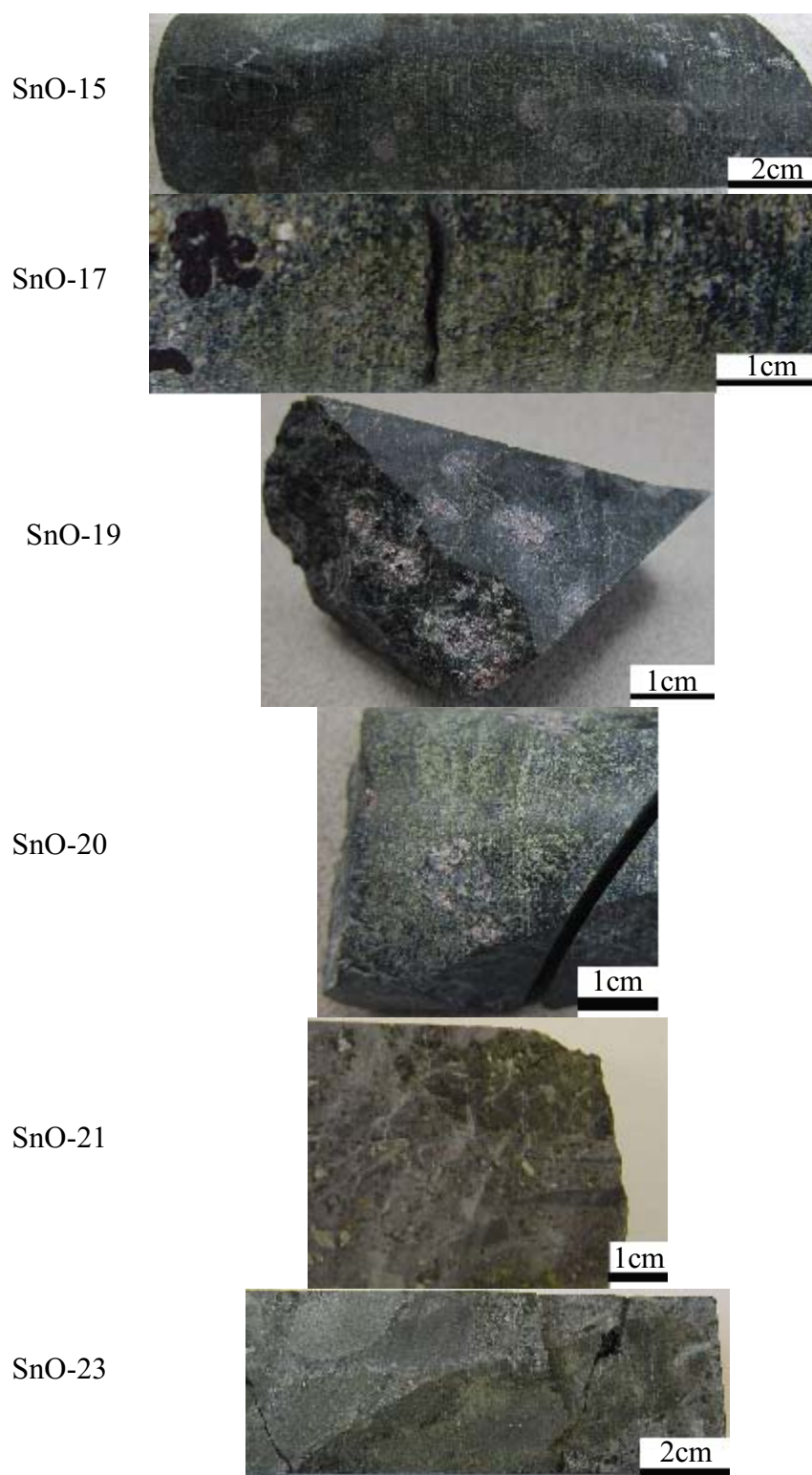


Figure A3.2 Hand sample images of central Victoria Island xenoliths in core

SnO-24



SnO-25



SnO-27  
SnO-28  
SnO-29



SnO-32



SnO-33



Figure A3.3 Hand sample images of central Victoria Island xenoliths in core

SnO-34



SnO-35



SnO-36



Figure A3.4 Hand sample images of central Victoria Island xenoliths in core

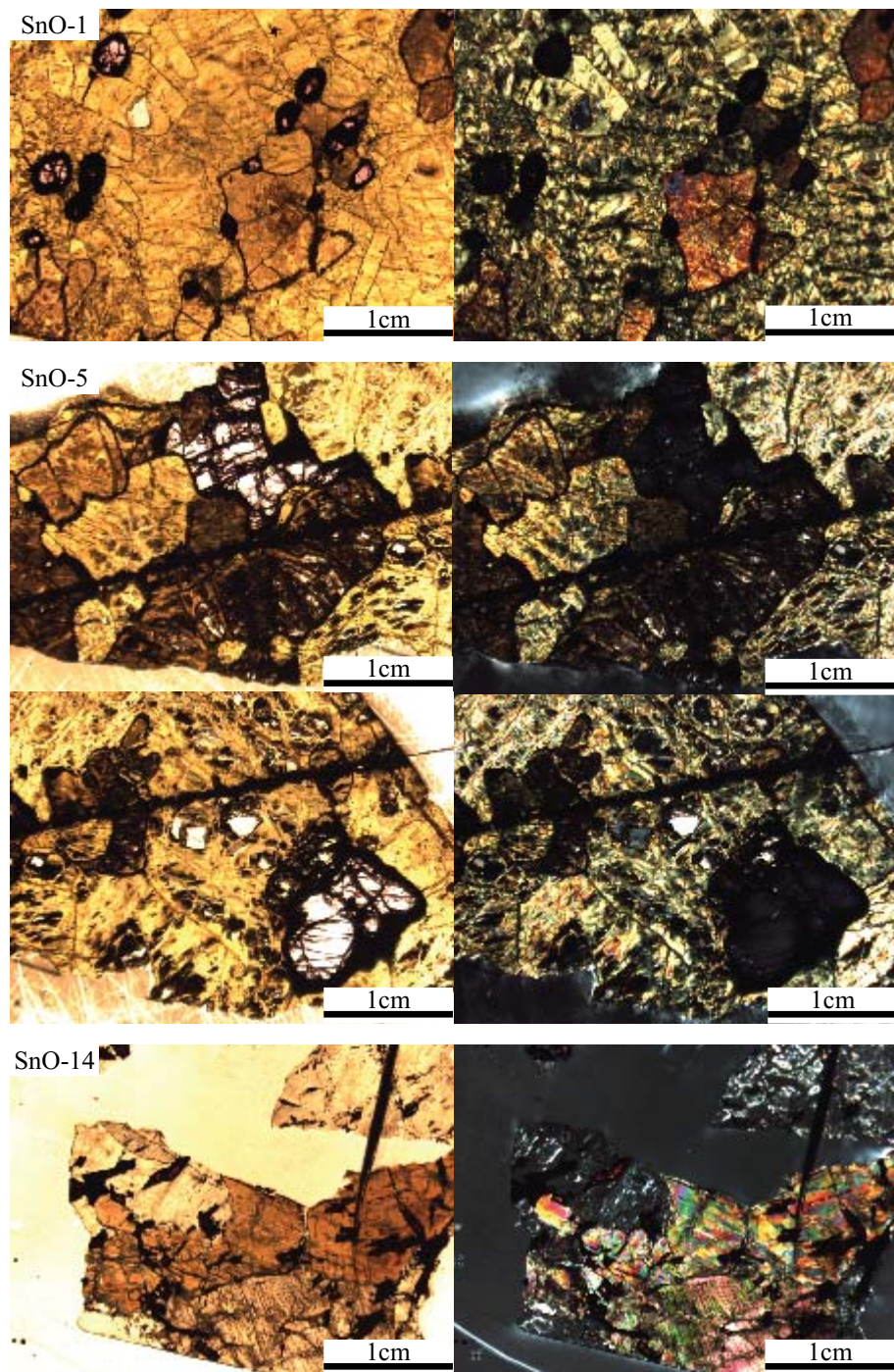


Figure A3.5 Thin section images of central Victoria Island xenoliths. Left images are in ppl, right images xpl.

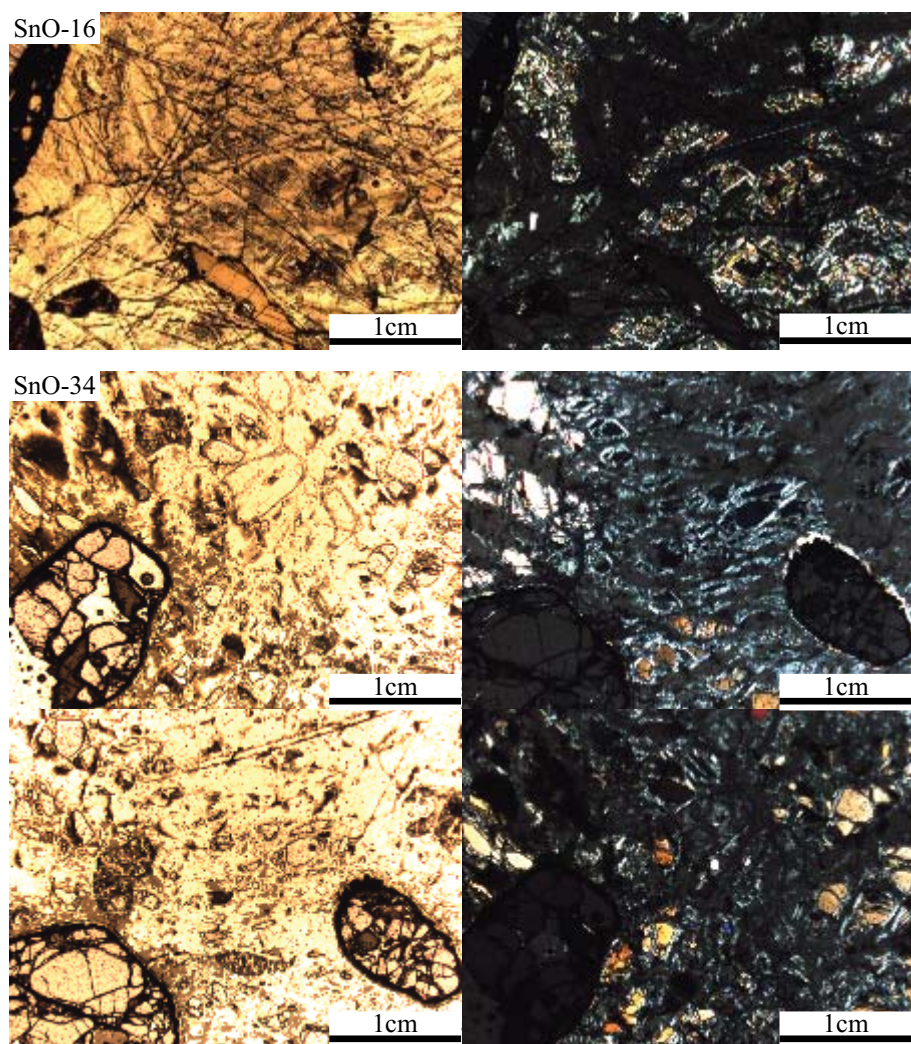


Figure A3.6 Thin section images of central Victoria Island xenoliths. Left images are in ppl, right images xpl.

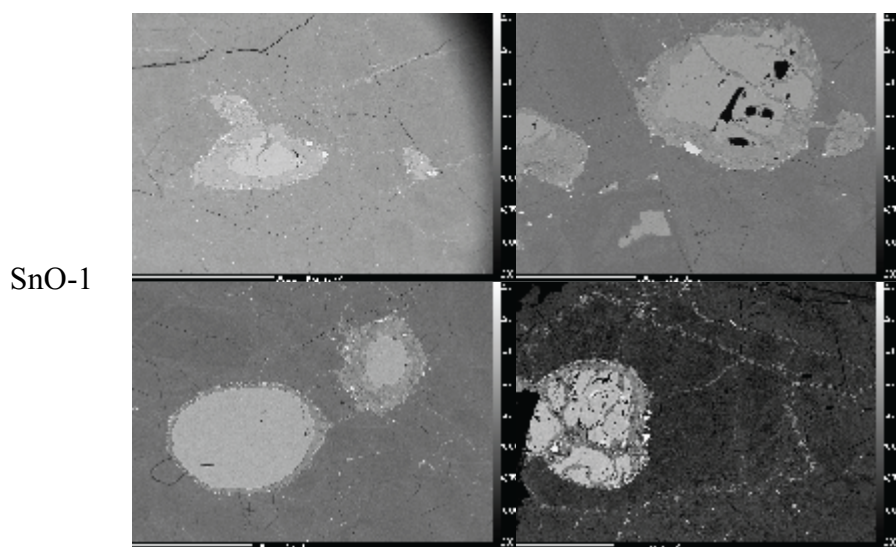


Figure A3.7 BSE images of SnO-1

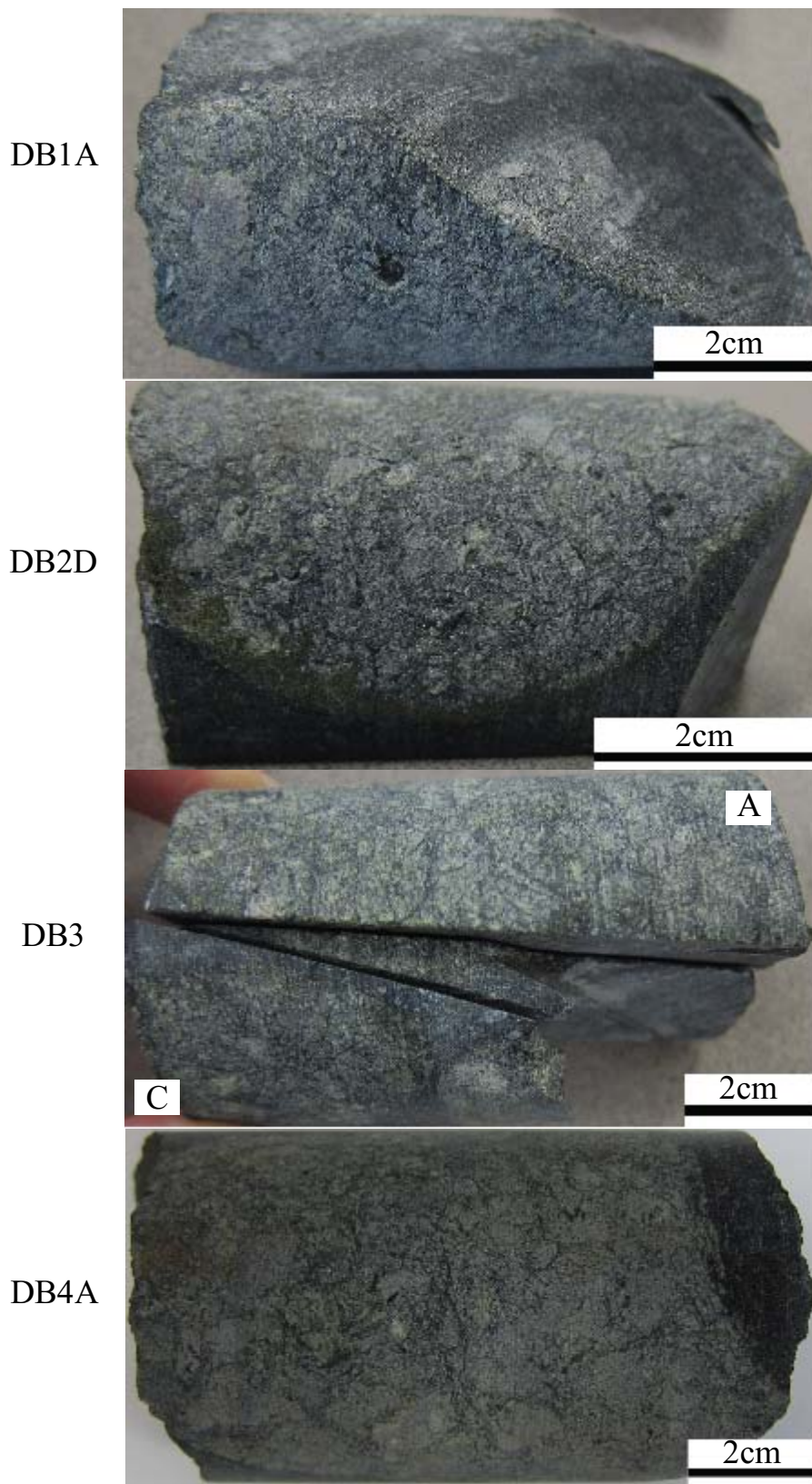
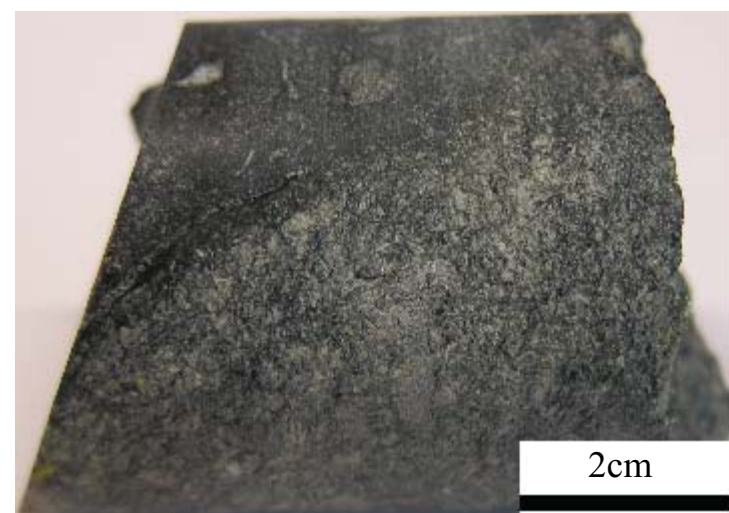


Figure A3.8 Hand sample images of Parry Peninsula peridotite xenoliths in core



Figure A3.9 Hand sample images of Parry Peninsula peridotite xenoliths in core

DB8A



2cm

DB9



C

2cm

DB11A



2cm

Figure A3.10 Hand sample images of Parry Peninsula peridotite xenoliths in core

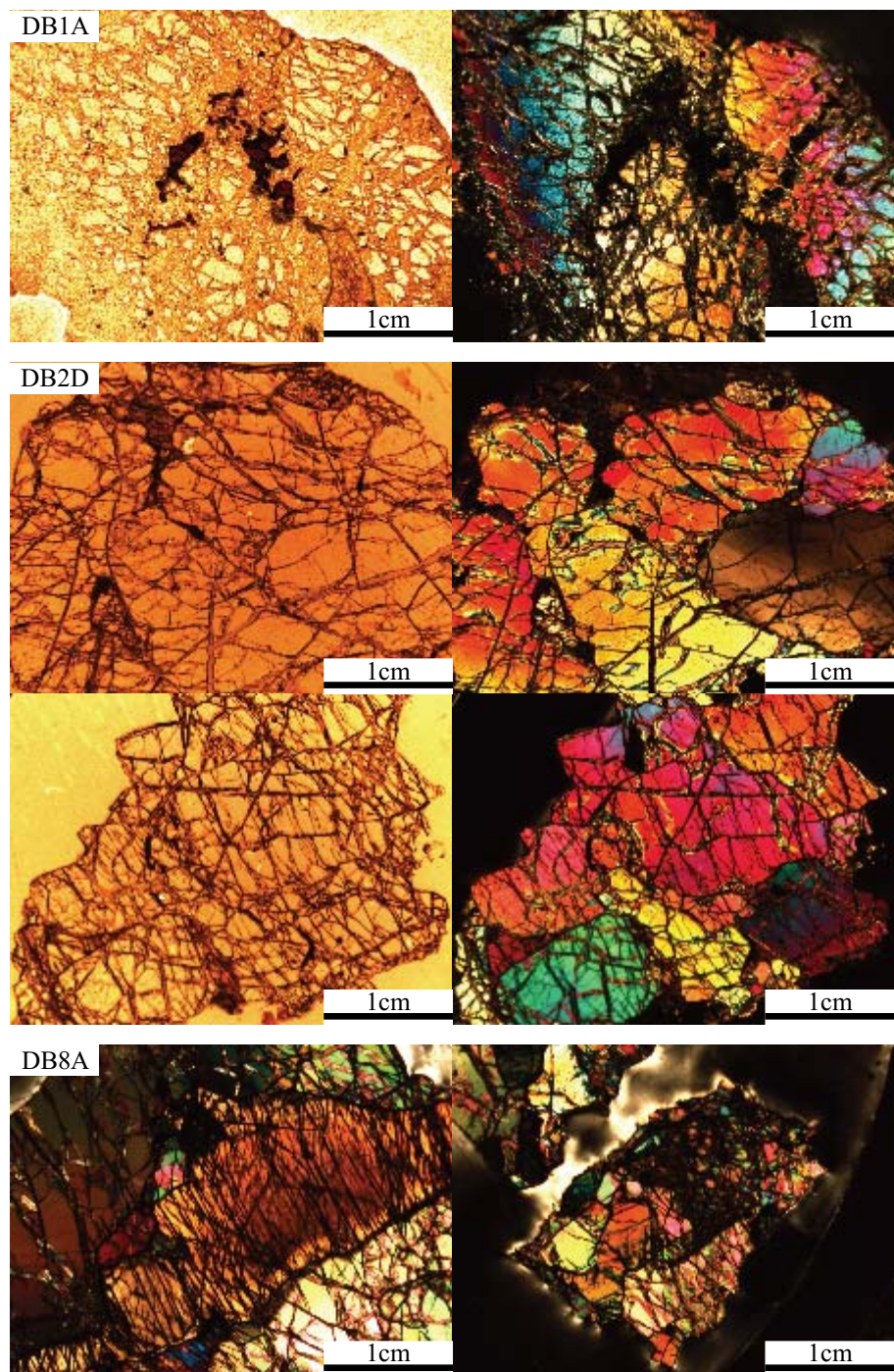


Figure A3.11 Thin section images of Parry Peninsula peridotite xenoliths. Left images are in ppl, right images xpl.

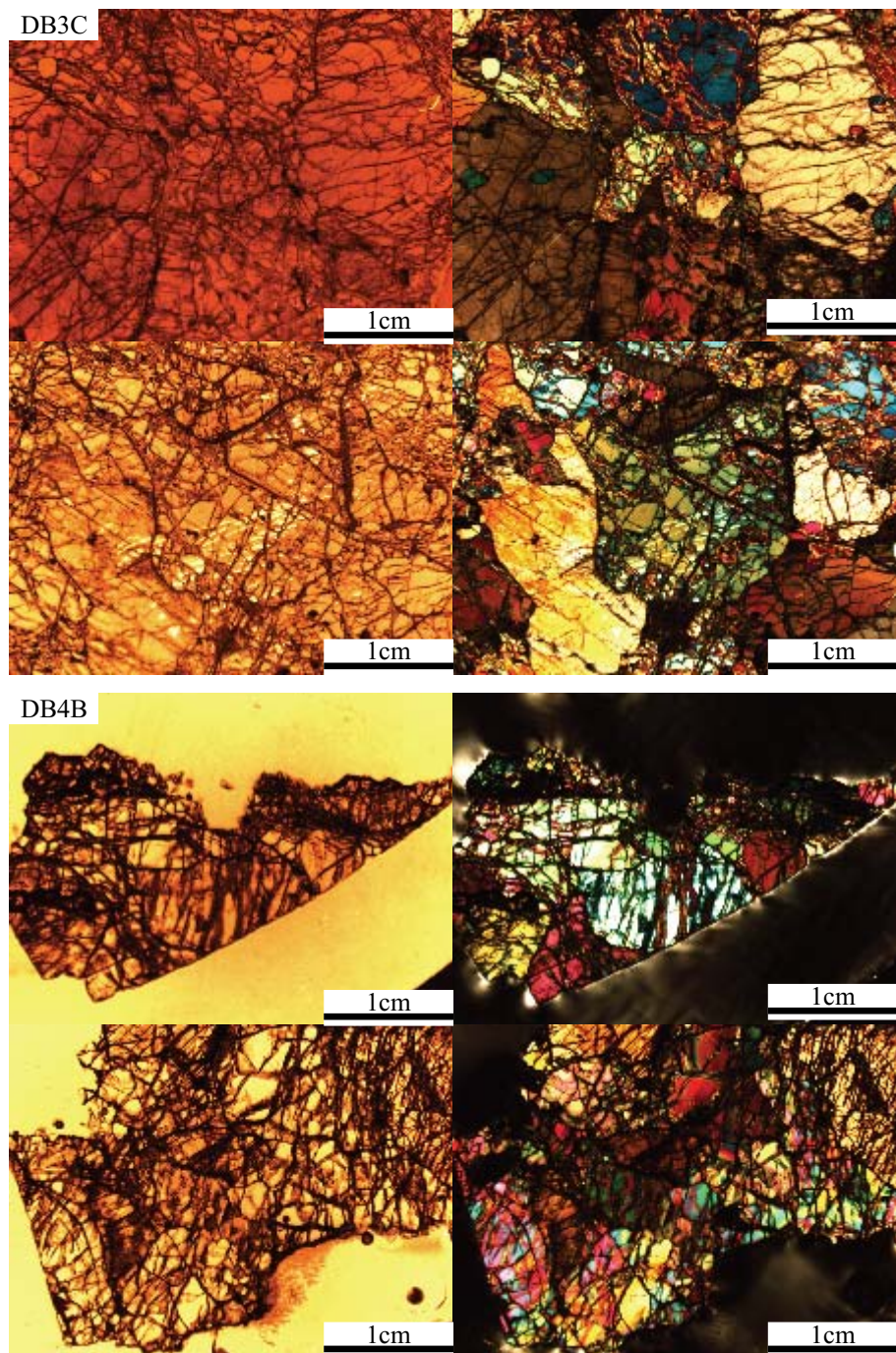


Figure A3.12 Thin section images of Parry Peninsula peridotite xenoliths. Left images are in ppl, right images xpl.

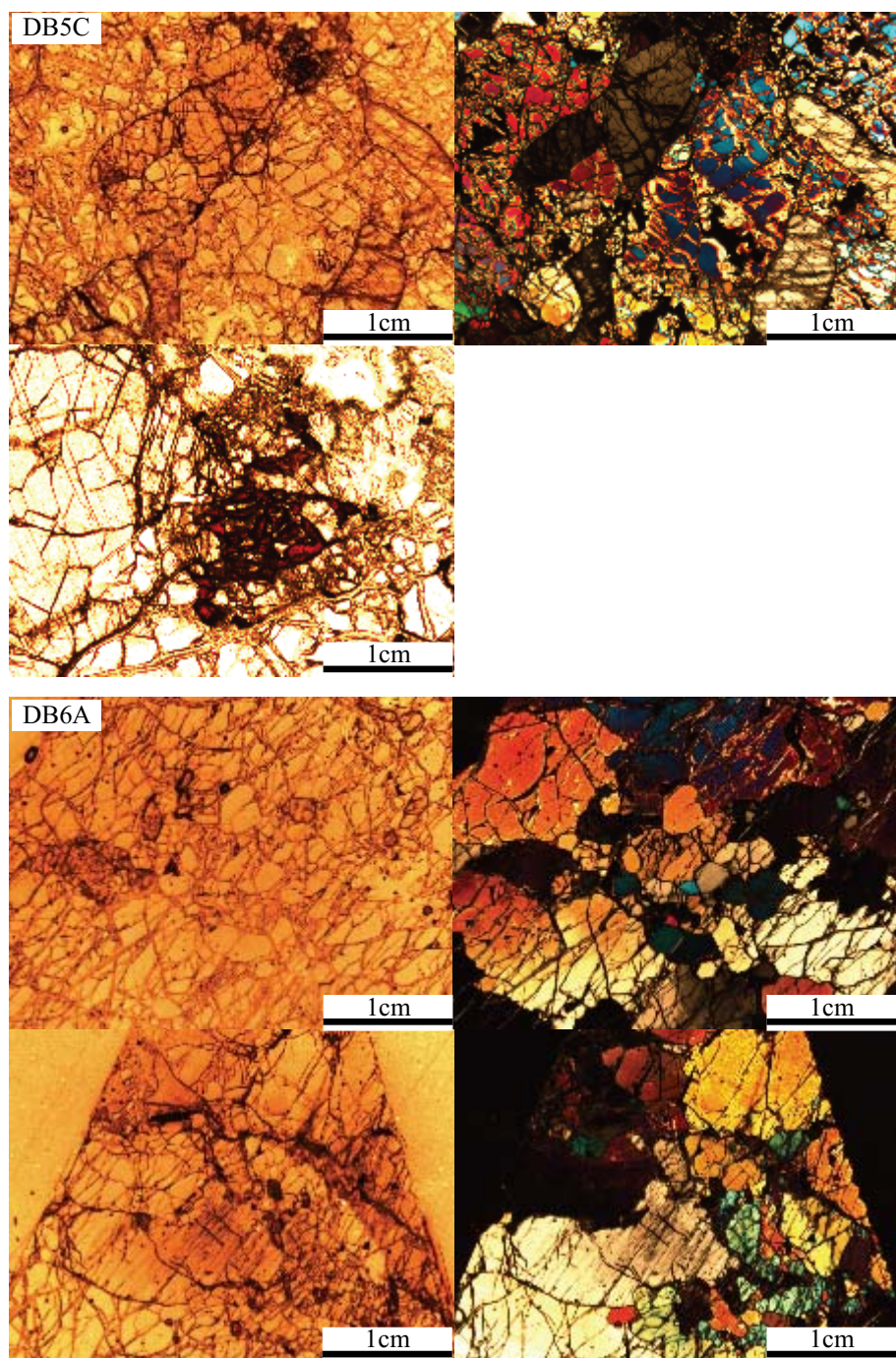


Figure A3.13 Thin section images of Parry Peninsula peridotite xenoliths. Left images are in ppl, right images in xpl.

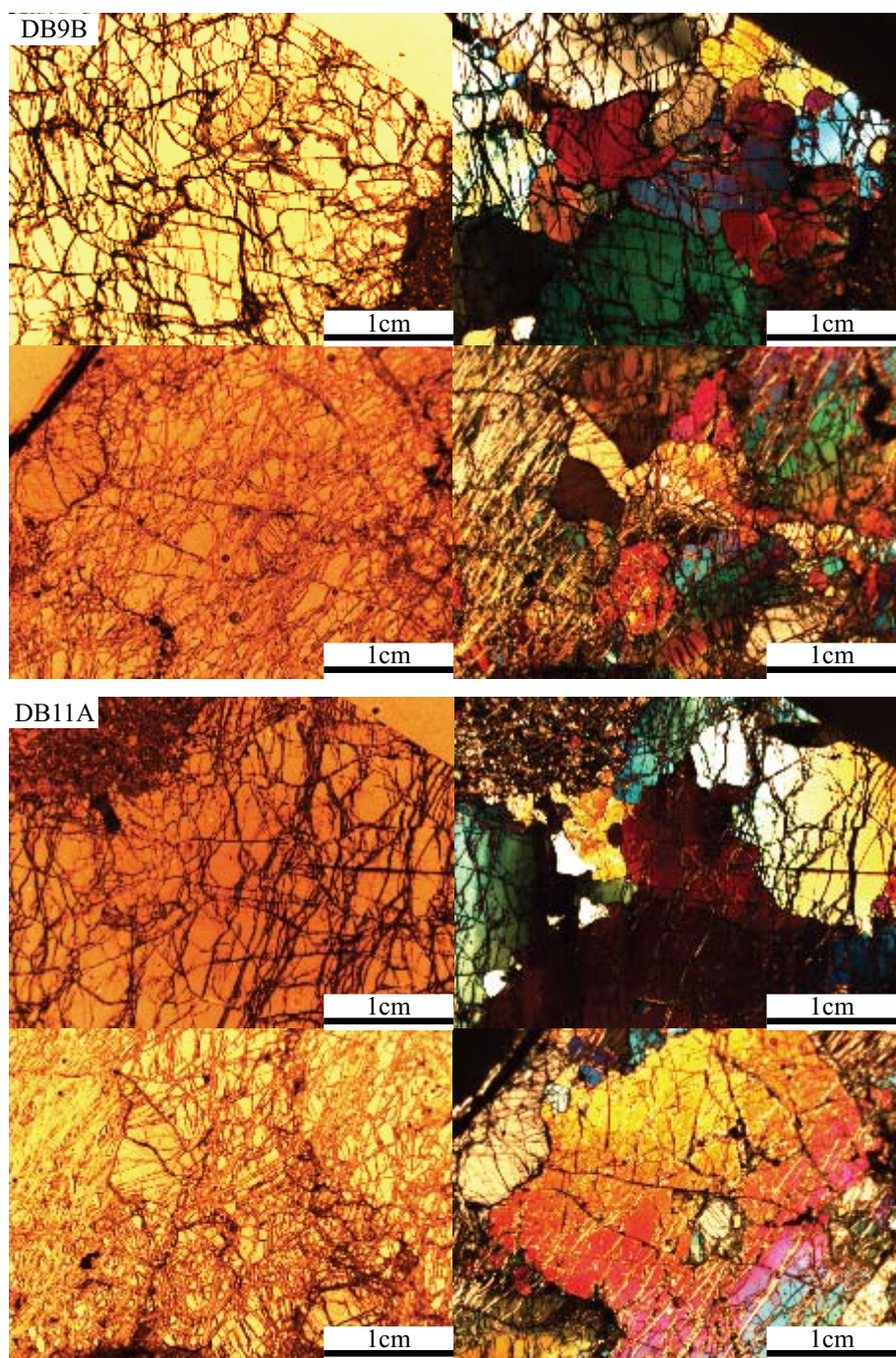


Figure A3.14 Thin section images of Parry Peninsula peridotite xenoliths. Left images are in ppl, right images in xpl.

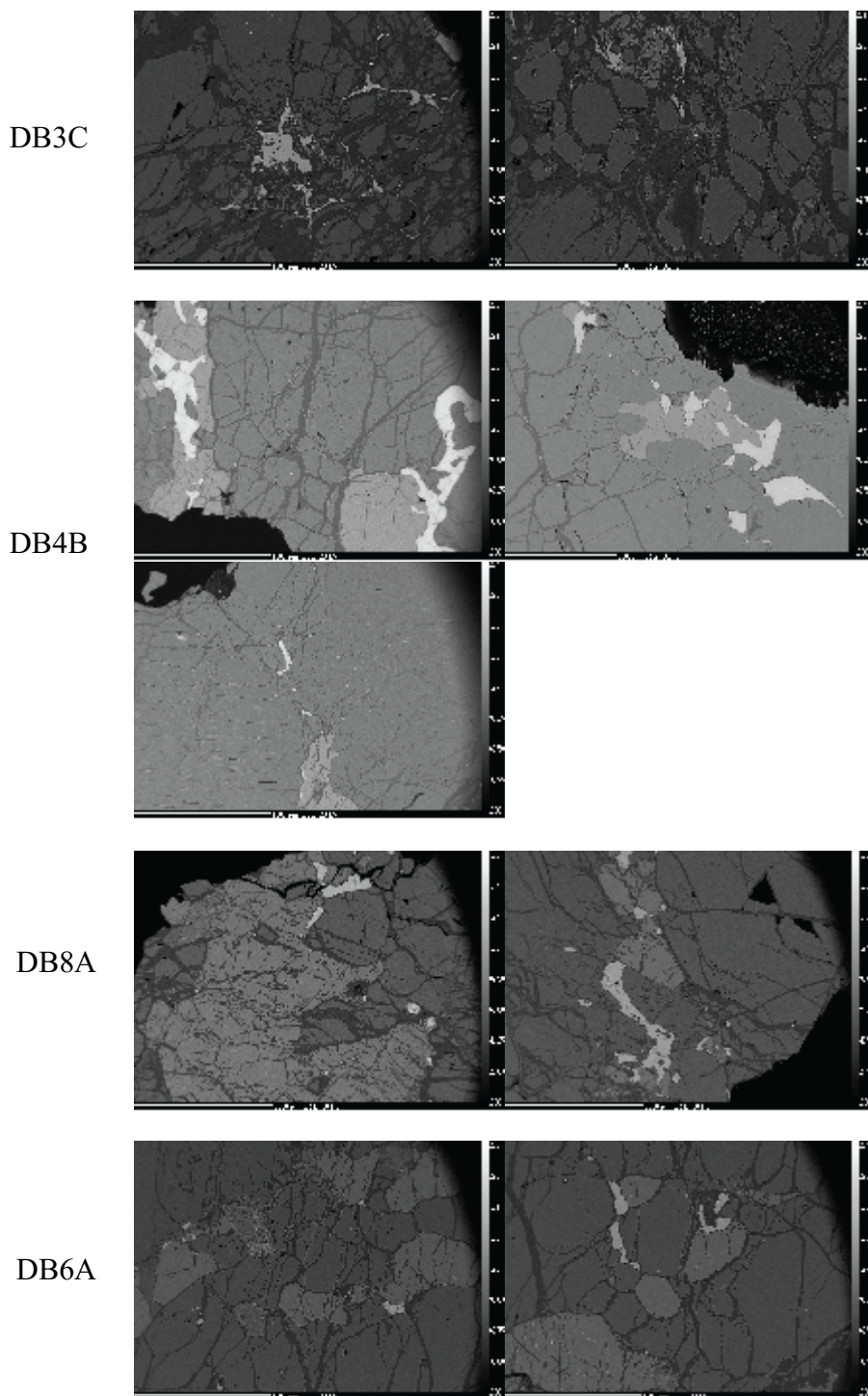


Figure A3.15: BSE images of Parry Peninsula peridotite xenoliths

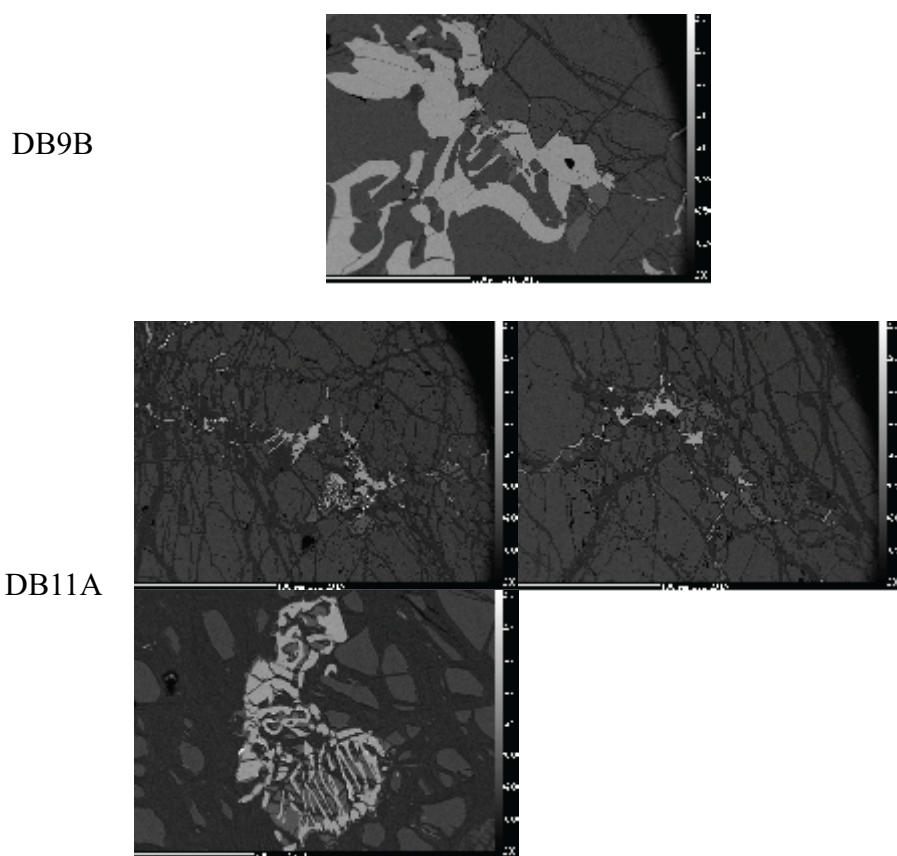


Figure A3.16: BSE images of Parry Peninsula peridotite xenoliths

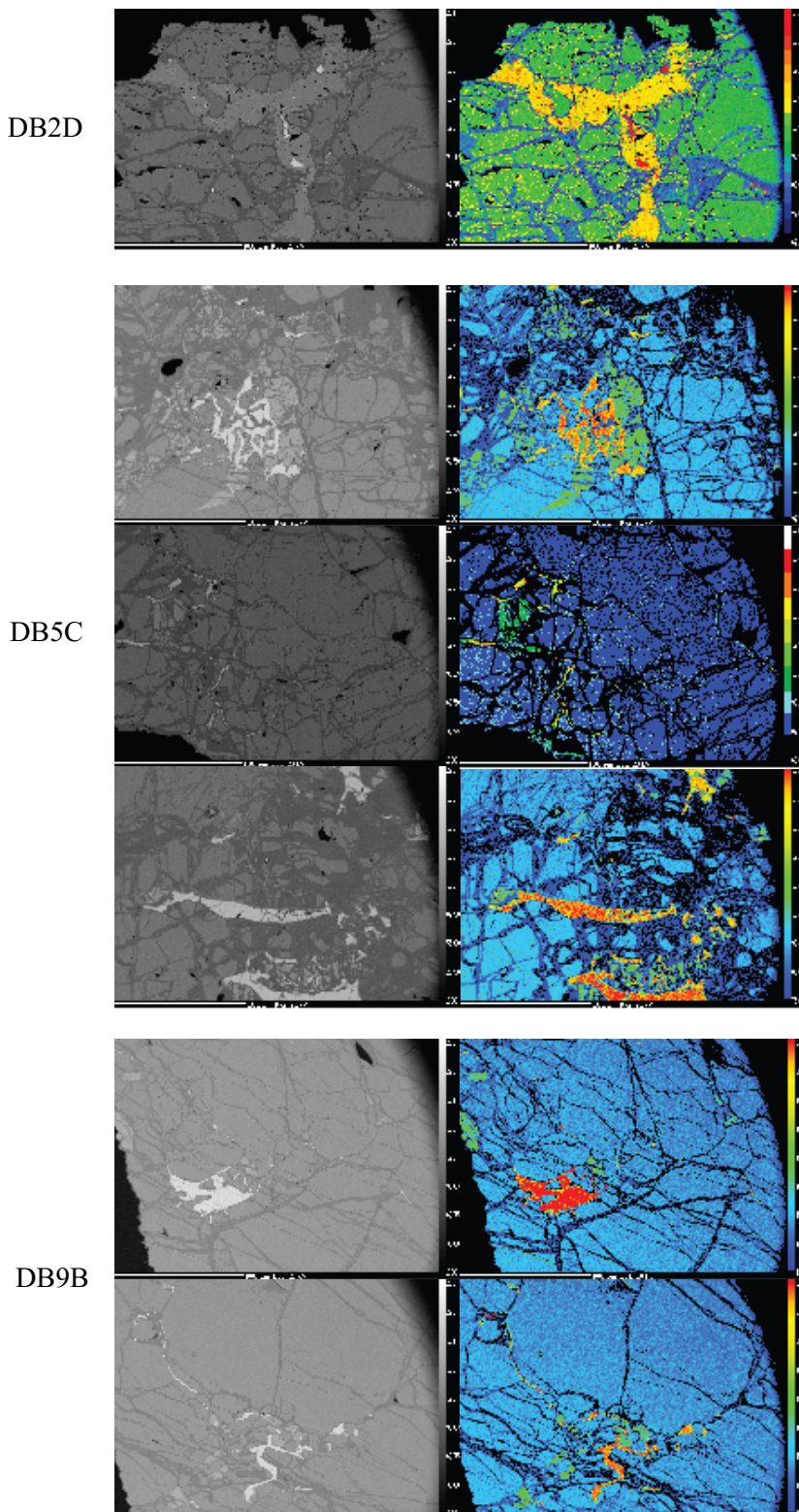


Figure A3.17 False colour BSE images of Parry Peninsula peridotite xenoliths. False coloured images show the degree of reflection, and correlate to different mineral phases. Brightest phases are spinels and clinopyroxene.

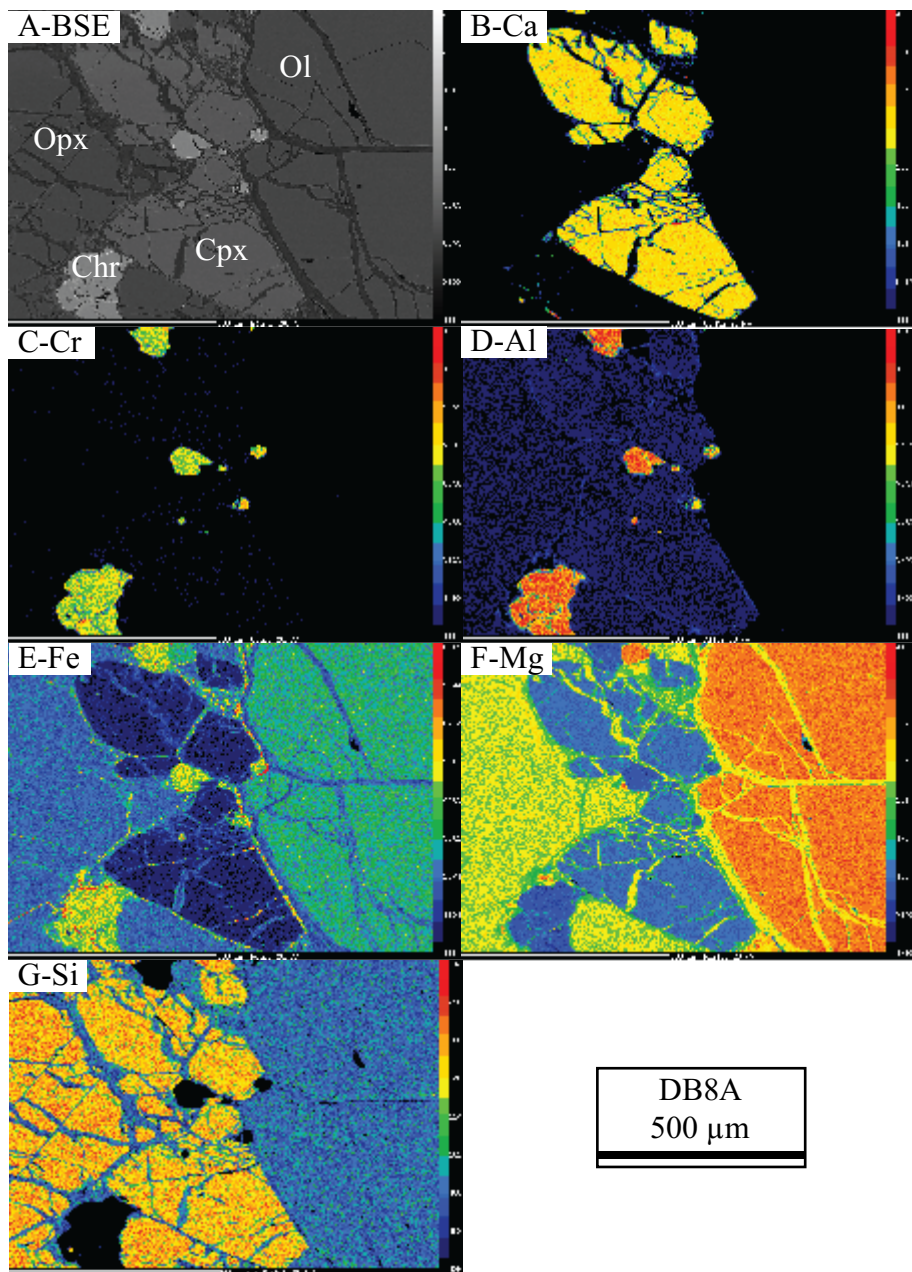


Figure A3.18 Electron microbeam mapping of DB8A at 20kV. A: grayscale BSE, phases are apparent by intensities of each element. B: Ca map highlighting clinopyroxene. C&D: Cr and Al maps, respectively, highlighting Cr-spinels. E,F,G: Fe, Mg, Si maps respectively. As scales are relative, olivine contains the most Mg, orthopyroxene and clinopyroxene similar Si that is higher than olivine. Fe is low (<10%) in all three phases with olivine>orthopyroxene>clinopyroxene. Chr=Chromite, Cpx=Clinopyroxene, Ol=Olivine and Opx=Orthopyroxene

## Appendix A4 Garnet Repeatability

Table A4.1 Garnet repeatability for SnO-24. Results after using a MAD outlier filter. Number of measurements=50, with only Ce displaying a large number of outliers (9). Barium is below detection limit for 47 out of 50 grains resulting in a very high standard deviation in relation to the mean.

	<b>Minimum</b>	<b>Maximum</b>	<b>Mean</b>	<b>St. Dev</b>
<b>Mineral Chemistry</b>				
SiO <sub>2</sub>	40.96	41.59	41.21	0.14
TiO <sub>2</sub>	0.05	0.12	0.08	0.022
Al <sub>2</sub> O <sub>3</sub>	16.88	17.35	17.17	0.13
FeO	7.29	7.55	7.42	0.08
MnO	0.36	0.41	0.38	0.012
MgO	19.15	19.59	19.38	0.11
CaO	6.08	6.21	6.15	0.032
Na <sub>2</sub> O	0.00	0.05	0.016	0.019
K <sub>2</sub> O	0.00	0.00	0.00	0
Cr <sub>2</sub> O <sub>3</sub>	7.88	8.29	8.04	0.09
NiO	0.00	0.00	0.00	0
V <sub>2</sub> O <sub>5</sub>	0.00	0.00	0.00	0
<b>Trace Elements</b>				
Ti	281	793	471	129
<sup>60</sup> Ni	58	71	63	2.58
<sup>61</sup> Ni	57	68	63	2.73
Sr	0.32	0.62	0.45	0.078
Y	0.81	2.1	1.41	0.361
Zr	6.19	13.8	9.68	2.18
Nb	0.62	0.87	0.73	0.064
Ba	0.00	1.24	0.03	0.175
La	0.09	0.13	0.12	0.010
Ce	0.89	1.20	1.04	0.071
Pr	0.16	0.31	0.23	0.039
Nd	1.21	2.08	1.60	0.227
Sm	0.50	0.83	0.66	0.088
Eu	0.15	0.30	0.22	0.036
Gd	0.31	0.87	0.60	0.150
Tb	0.03	0.11	0.07	0.022
Dy	0.14	0.50	0.31	0.103
Ho	0.02	0.08	0.05	0.015
Er	0.09	0.21	0.15	0.027
Tm	0.018	0.031	0.024	0.003
Yb	0.23	0.30	0.26	0.017
Lu	0.05	0.06	0.05	0.005
Hf	0.13	0.35	0.23	0.059

## Appendix A5 Concentrate Data

### A5.1 Concentrate mineral chemistry

A large database exists for both localities in terms of industry run mineral concentrate. Garnet, clinopyroxene, spinel, ilmenite, and phlogopite grains are available, although not at every location. A subset EDS analysis for CVI provided in Table A7.1.

Table A5.1 Count of concentrate grains by mineralogy

Mineral	Parry Peninsula	DeBeers provided data	Snowy Owl trend	Snowy Owl kimberlite
Garnet	2233	3250	894	550
Cpx	483	1063	49	7
Sp	1964	36	450	398
Ill	2213	614	300	190
Phl	-	16	-	-

### A5.2 Thermobarometry for mineral concentrate

#### A5.2.1 Single Clinopyroxene

Clinopyroxene concentrate from Central Victoria Island displays a much broader thermal structure than that available from the xenoliths. When grouped in to kimberlite trends, a trend becomes apparent, where the Northern most trends are sampling deeper mantle than those to the south. For the Snowy Owl Trend, of the 56 clinopyroxene grains that passed stoichiometric checks, only 4 (qualitatively plotted in Figure A6.1) produced a T-P pair, but none the quality filter. This is in comparison to the 520 of 1050 that produced a P-T pair and 98 (plotted in Figure A6.1) that passed the quality filters from the other two trends.

Table A5.2 Temperatures and pressures of central Victoria Island clinopyroxene concentrate (single-clinopyroxene method; Nimis & Taylor 2000).

Kimberlite	Kimberlite trend	Temperature (°C)			Pressure (kbar)			mean
		min	max	median	mean	min	max	
Snow Goose	Galaxy Structure	715	1309	990	1024	36	70	53
Snow Bunting	Galaxy Structure	689	1146	948	948	38	60	54
Turnstone	King Eider	867	1321	1231	1220	36	67	61
King Eider	King Eider	786	1328	1275	1213	45	67	64
								61

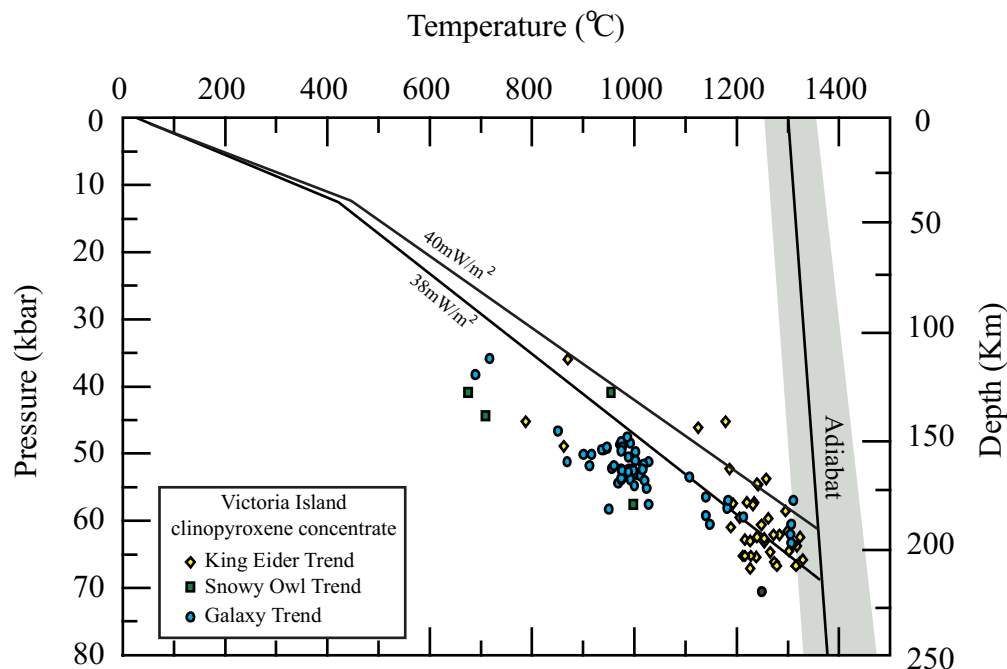


Figure A5.1 Victoria Island concentrate single-clinopyroxene temperatures and pressures calculated using the Nimis and Taylor (2000) method. Data roughly lies on a  $38 \text{ mW/m}^2$  geotherm of Hasterok and Chapman (2011). Snowy Owl trend is graphed for qualitative assessment only. The King Eider kimberlite trend samples mantle at a much deeper depth profile than those of the Snowy Owl kimberlite trend.

Table A5.3 Temperatures and pressures of Parry Peninsula clinopyroxene concentrate (single-clinopyroxene method; Nimis & Taylor 2000). Of 520 data points 352 passed the quality filters.

Sample Location	Temperature (°C)				Pressure (kbar)			
	min	max	median	mean	min	max	median	mean
Darnley Bay-1	1080	1204	1113	1134	46	53	48	49
Darnley Bay-2	845	1293	959	1054	30	57	38	43
Darnley Bay-5	829	1267	1208	1159	35	62	50	49
Darnley Bay-6	1043	1213	1083	1087	44	61	49	49
Darnley Bay-8	813	1151	883	899	33	57	36	37
Darnley Bay-9	883	1288	1105	1105	36	62	49	48
Darnley Bay-11	1250	1256	1253	1253	52	54	53	53

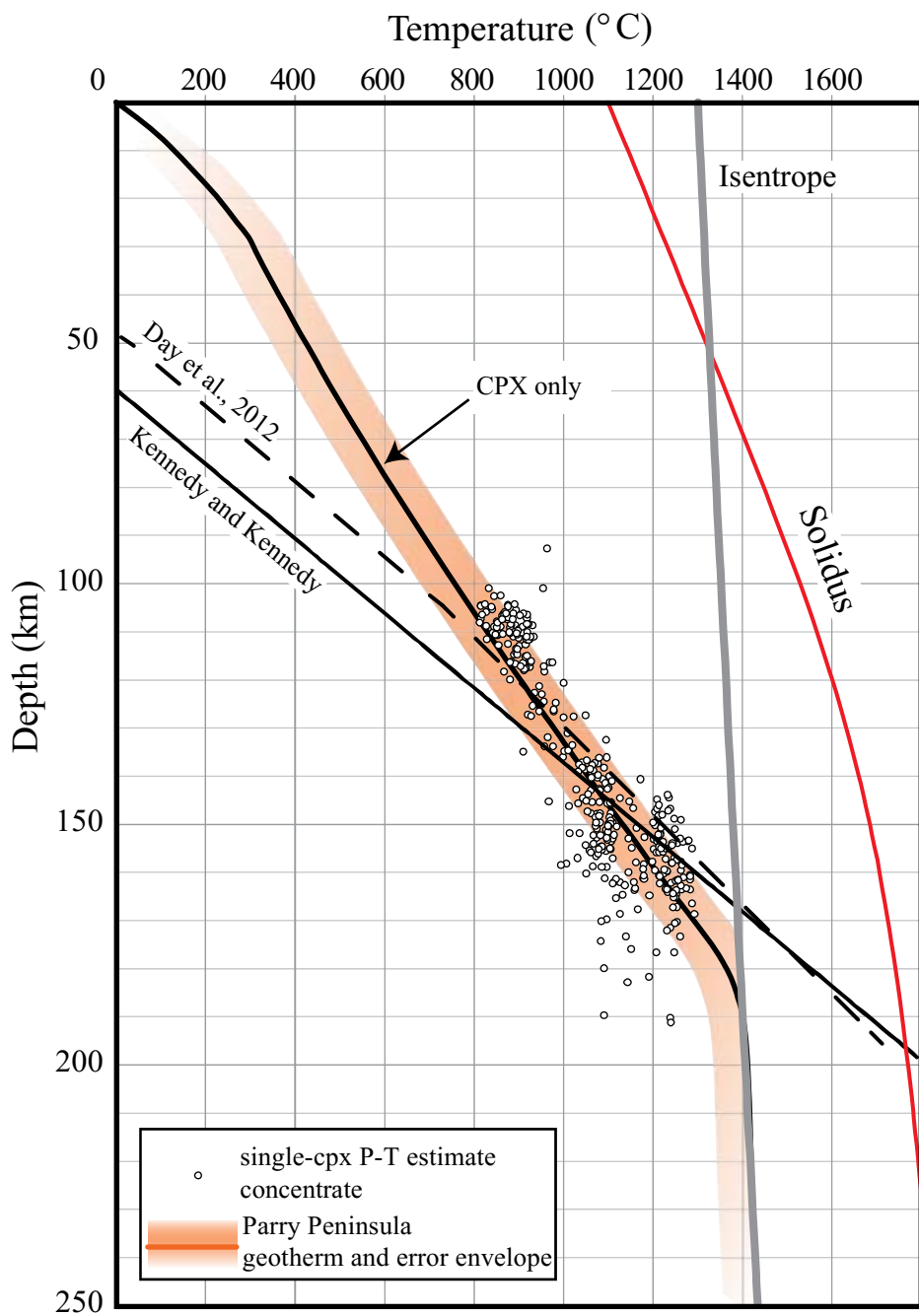


Figure A5.2 FITPLOT geotherm modeled on single-clinopyroxene temperatures and pressures from Parry Peninsula clinopyroxene concentrate. Compared to geotherms modeled on xenoliths or mixed xenolith-concentrate, concentrate alone results in a steeper curve that provides for a possible diamond stable lithosphere with a greater temperature and depth range.

### **A5.2.2 Nickel in Garnet Thermometer**

Laser trace element work was carried out on garnet concentrate to determine a Nickel temperature (Canil, 1999). A Ni-in-olivine concentration of 3000ppm was used for the calculations.

Table A5.4 Nickel temperatures from central Victoria Island garnet concentrate

Kimberlite	Mean Temperature (°C)	Standard Deviation (°C)	Median Temperature (°C)	Count
Jaeger 4	1046	85	1055	26
Jaeger 6	971	97	941	14
King Eider	1013	118	1059	8
Pintail	1052	65	1046	7

## Appendix A6 Thermobarometry

Table A6.1 FITPLOT parameters used for thermobarometry. FITPLOTS provided in the body of the thesis use crustal parameters. Those below in this Appendix use Slave crustal parameters (Figures A6.1 and A6.2) and crustal parameters with lower crust heat generation (Figure A6.3 and A6.4).

	Crustal Heat Parameters	Slave Crustal Heat Parameters	Crustal Parameters with Lower Crust Heat Generation
Lower crust (km)	10	22	10
Upper crust (km)	18	23	18
Upper Crust heat production (W/m <sup>3</sup> )	1.20E-06	1.20E-06	1.20E-06
Lower Crust heat production (W/m <sup>3</sup> )	4.00E-07	4.00E-07	1.50E-07
Mantle heat production (W/m <sup>3</sup> )	0	0	0
<b>Central Victoria Island estimated Diamond window (km)</b>	<b>119-215 ±12</b>	<b>118-219 ±14</b>	<b>117-215 ±13</b>
<b>Parry Peninsula estimated Diamond window (km)</b>	<b>145-185 ±15</b>	<b>144-194 ±10</b>	<b>144-182 ±18</b>

In general, FITPLOT geotherms fit to the xenolith peridotites produce very similar lithosphere thicknesses, within error, regardless of variations to crustal thickness or lower crust heat generation.

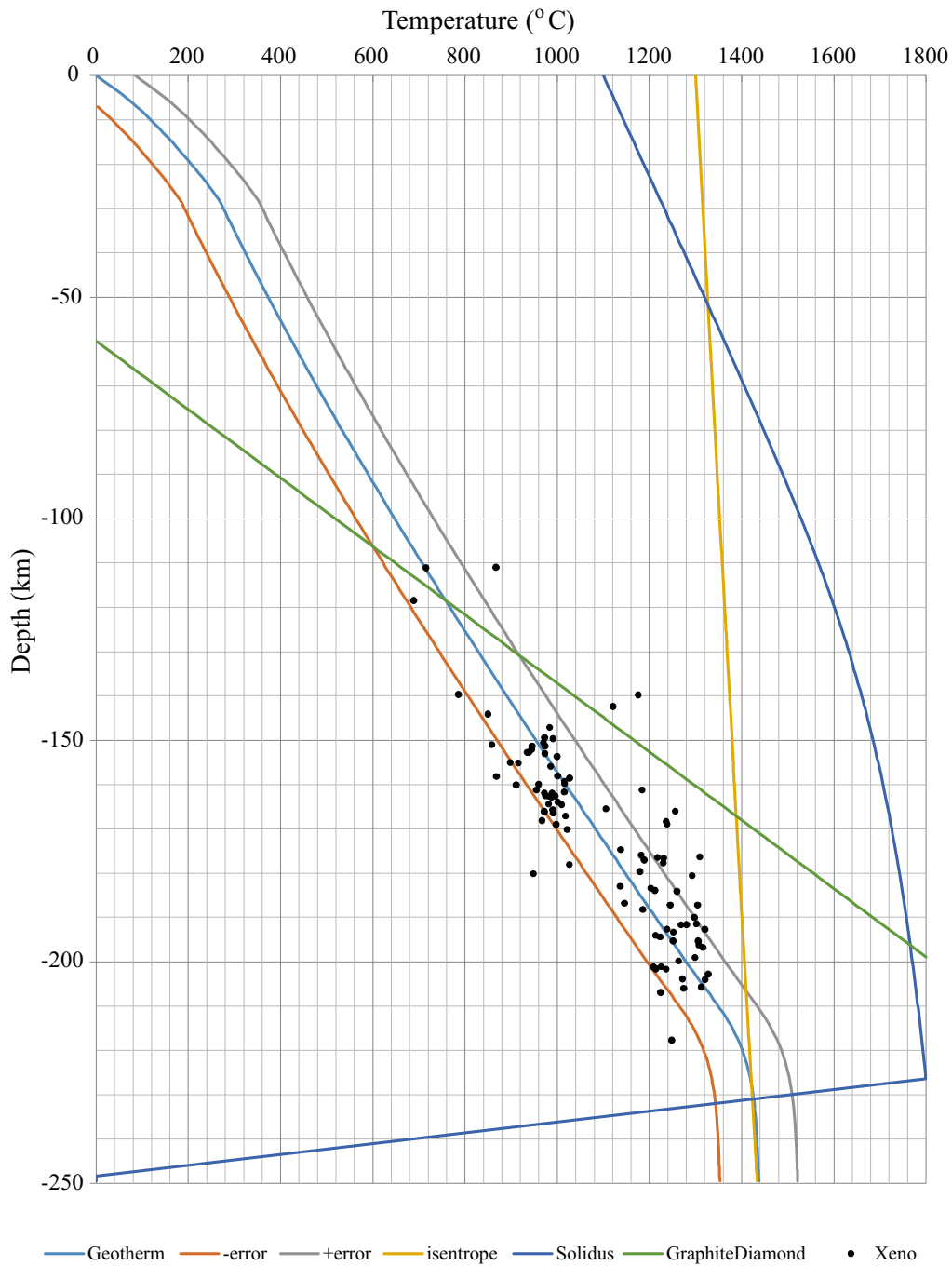


Figure A6.1 FITPLOT for Central Victoria Island xenoliths using Slave crustal parameters from Table A6.1.

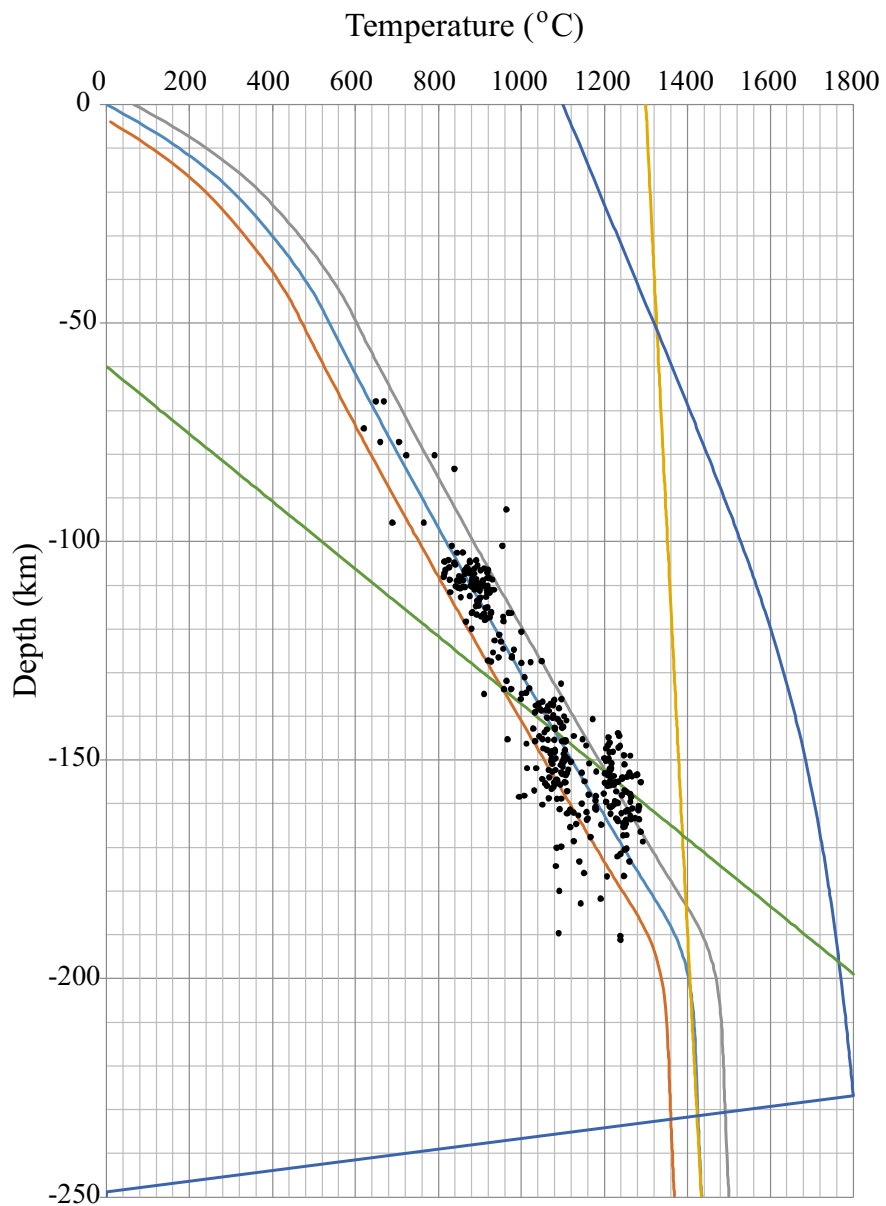


Figure A6.2 FITPLOT for Parry Peninsula xenoliths with concentrate using Slave crustal parameters from Table A6.1

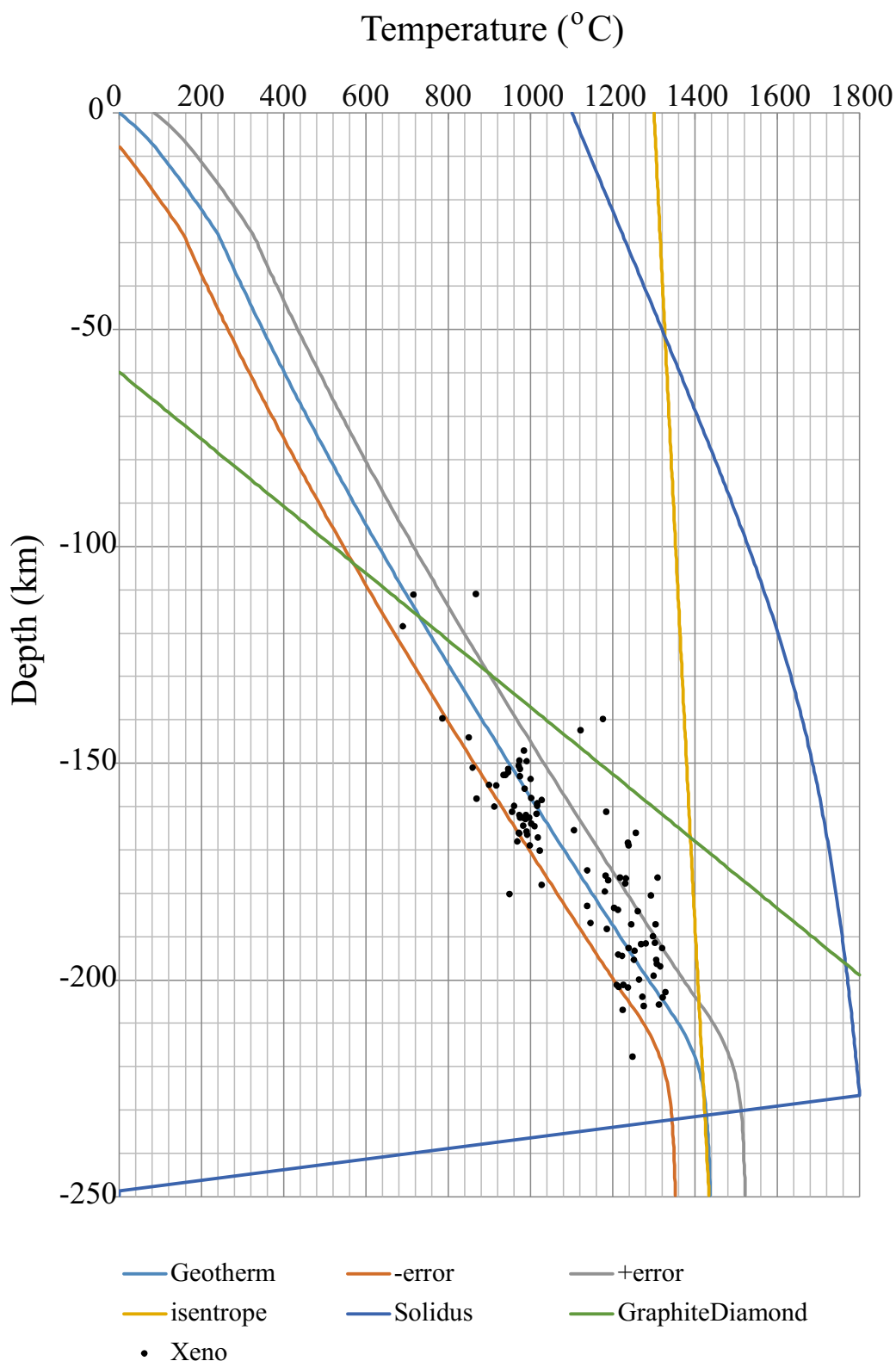


Figure A6.3 FITPLOT for Central Victoria Island xenoliths using crustal parameters with lower crust heat generation from Table A6.1.

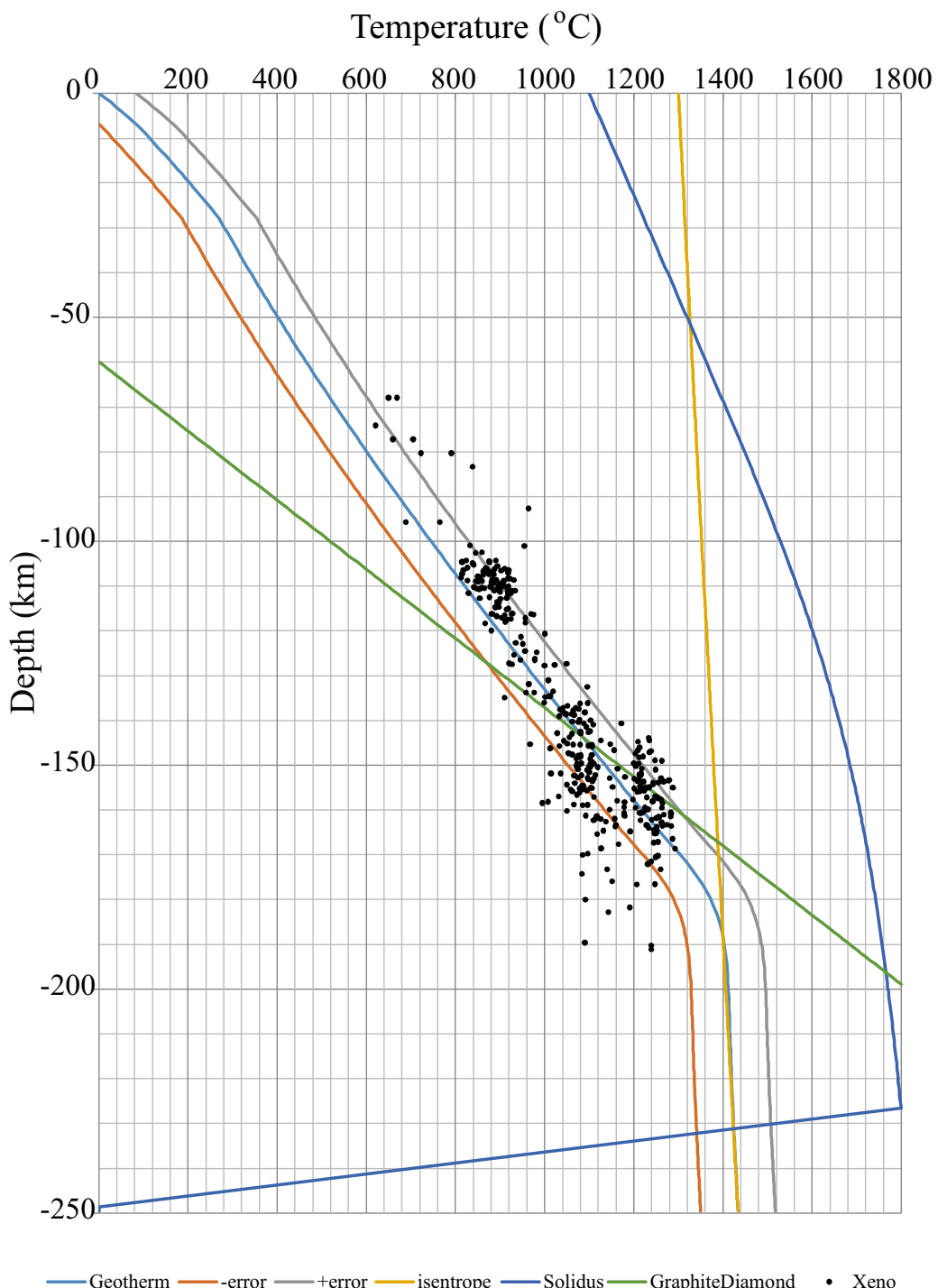


Figure A6.4 FITPLOT for Parry Peninsula xenoliths with concentrate using crustal parameters with lower crust heat generation from Table A6.1

## **Appendix A7 Central Victoria Island mineral grain re-analysis**

### **A7.1 Mineral Chemistry**

330 grains were selected from three different central pipes within the Blue Ice and King Eider trends and analyzed in house with WDS to compare to values reported using EDS from industry evaluation. As quickly attained EDS mineral composition data is widely used within the exploration field, and in particular, within the Canadian North, an assessment of this method against the longer run times associated with WDS can be used to inform the quality of millions of kimberlite indicator minerals available.

Graphically, these grains appear to show values near 1:1, implying that low resolution concentrate compositional analysis done for industry purposes can be compositionally valid to describe mineral chemistry. It is interesting to note that clinopyroxene Na<sub>2</sub>O values produce over-estimates (up to ~15%), while FeO, Al<sub>2</sub>O<sub>3</sub> and CaO perform result in high R<sup>2</sup> values and near 1:1 ratios to WDS. Garnet appears to have been less accurate, as displayed by a very poor trend line equation and low R<sup>2</sup> values, especially for Cr<sub>2</sub>O<sub>3</sub>. As garnet is prevalently used for assessment of lithospheric mantle sources using Ca-Cr plots, using them strictly for qualitative purposes is likely best.

Figure A7.1 EDS versus WDS for concentrate garnet. CaO visually displays very similar values but has conflicting equations and  $R^2$  values. While a subset of data records similar values between the two methods for  $\text{Cr}_2\text{O}_3$ , a large number outliers may indicate nugget effects within the garnets and results in a very low  $R^2$  value.

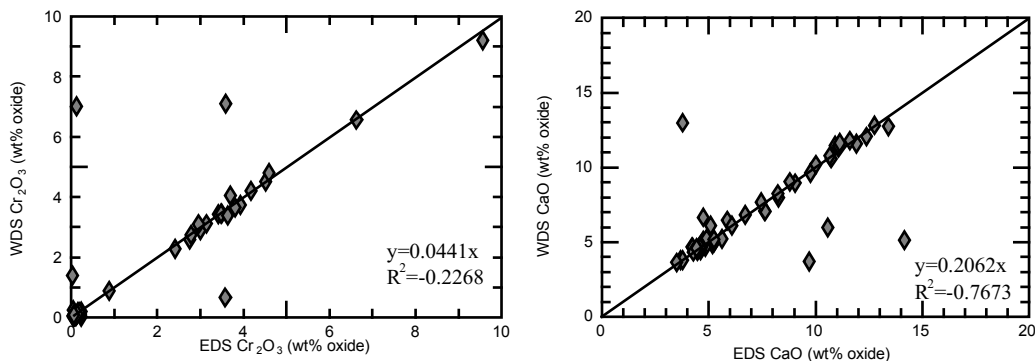


Figure A7.2 EDS versus WDS for concentrate clinopyroxene. FeO,  $\text{Al}_2\text{O}_3$ , and CaO display very similar values between the two methods, with CaO displaying some scatter;  $\text{Na}_2\text{O}$  has consistently lower measurements by EDS.

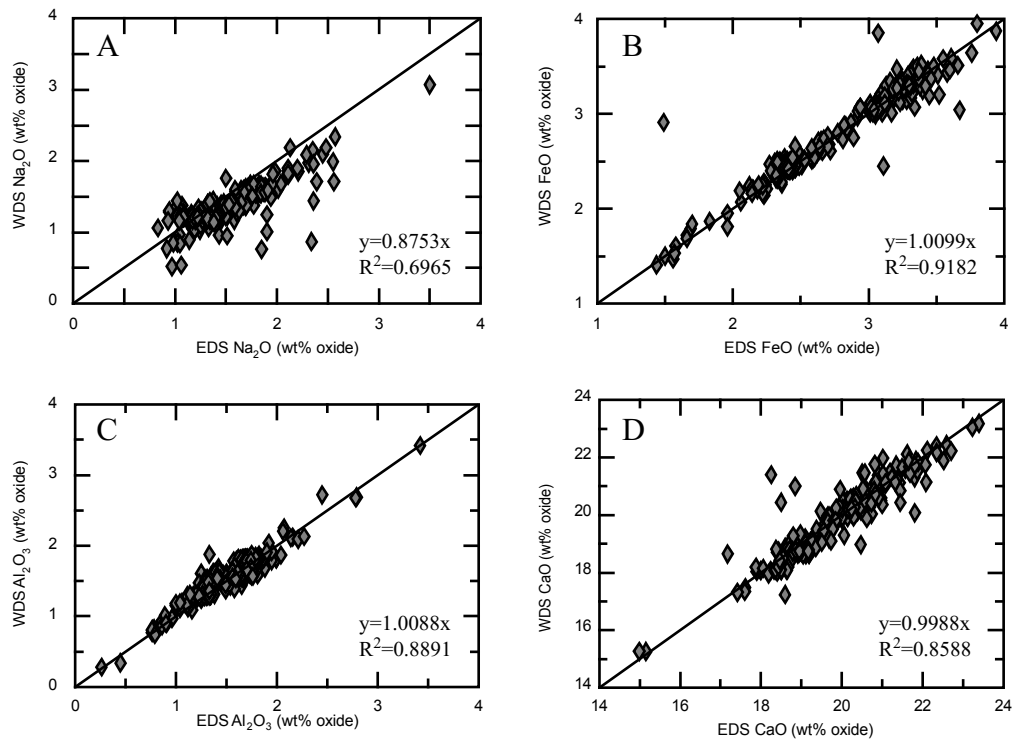


Table A7.1 DeBeers EDS garnet compositions used for industry comparison

grain name	SiO <sub>2</sub>	TiO <sub>2</sub>	Al <sub>2</sub> O <sub>3</sub>	FeO	MnO	MgO	CaO	Na <sub>2</sub> O	Cr <sub>2</sub> O <sub>3</sub>	Total	MG#
SANDPIPER-GAR-4-64	42.29	0.13	23.04	11.83	0.30	19.72	3.69	0.05	0.23	101.28	0.75
SANDPIPER-GAR-4-35	41.90	0.13	21.70	7.90	0.39	21.37	4.46	0.07	2.41	100.33	0.83
PINTAIL-GAR-6-91	43.05	0.11	19.52	7.20	0.33	18.84	5.17	0.00	4.52	98.74	0.82
PINTAIL-GAR-6-69	44.10	0.11	19.52	7.88	0.44	18.03	5.61	0.00	4.60	100.29	0.80
PINTAIL-GAR-6-68	43.69	0.14	19.84	7.75	0.40	18.57	5.25	0.16	4.18	99.98	0.81
PINTAIL-GAR-6-27	42.87	0.10	22.93	13.45	0.25	14.37	7.62	0.01	0.04	101.64	0.66
PINTAIL-GAR-6-41	41.04	0.10	22.35	15.91	0.38	12.15	7.64	0.03	0.06	99.66	0.58
JAEGER-GAR-6-6	41.81	0.10	21.10	13.89	0.30	11.39	10.72	0.10	0.03	99.44	0.59
JAEGER-GAR-6-3	41.39	0.09	21.99	12.10	0.35	10.97	13.42	0.02	0.04	100.37	0.62
JAEGER-GAR-6-20	42.60	0.10	20.89	7.86	0.41	20.24	4.82	0.03	3.00	99.95	0.82
JAEGER-GAR-6-39	40.94	0.13	21.68	15.59	0.31	11.47	9.75	0.11	0.09	100.07	0.57
JAEGER-GAR-6-43	41.64	0.11	22.36	12.19	0.21	12.08	12.37	0.08	0.09	101.13	0.64
JAEGER-GAR-6-57	43.40	0.12	20.51	7.66	0.38	19.87	4.73	0.04	3.58	100.29	0.82
JAEGER-GAR-6-64	42.78	0.11	21.19	7.72	0.41	20.02	4.66	0.08	3.50	100.47	0.82
JAEGER-GAR-6-75	41.38	0.13	22.30	14.38	0.33	11.69	10.59	0.13	0.12	101.05	0.59
JAEGER-GAR-6-77	40.91	0.09	21.98	15.31	0.33	11.50	9.70	0.06	0.04	99.92	0.57
JAEGER-GAR-6-78	41.51	0.09	22.03	14.53	0.37	16.35	3.77	0.06	0.23	98.94	0.67
JAEGER-GAR-6-81	42.12	0.10	22.76	13.28	0.27	13.59	9.06	0.05	0.07	101.30	0.65
JAEGER-GAR-6-100	41.58	0.10	21.73	10.63	0.26	12.11	13.58	0.04	0.03	100.06	0.67
JAEGER-GAR-6-92	41.01	0.09	21.51	16.93	0.48	14.69	4.60	0.04	0.88	100.23	0.61
JAEGER-GAR-6-69	41.65	0.11	22.55	10.43	0.29	10.84	14.16	0.08	0.00	100.11	0.65
JAEGER-GAR-6-54	42.74	0.13	19.92	7.92	0.44	19.88	5.07	0.00	3.59	99.69	0.82
JAEGER-GAR-6-35	41.54	0.12	21.83	12.63	0.48	12.04	11.93	0.05	0.08	100.70	0.63
JAEGER-GAR-6-36	40.96	0.14	21.44	11.96	0.21	11.22	12.75	0.06	0.04	98.78	0.63
KING_EIDER-GAR-3-2	42.82	0.03	21.87	7.97	0.46	18.81	4.75	0.04	3.93	100.68	0.81
KING_EIDER-GAR-3-22	43.02	0.07	21.35	7.21	0.37	19.85	4.20	0.03	3.42	99.52	0.83
KING_EIDER-GAR-3-18	42.80	0.10	21.51	8.22	0.50	19.35	4.63	0.07	3.80	100.98	0.81
KING_EIDER-GAR-3-12	42.18	0.13	23.85	10.85	0.31	17.46	4.88	0.04	0.21	99.91	0.74
KING_EIDER-GAR-3-69	41.50	0.10	23.30	14.47	0.34	14.08	5.87	0.05	0.10	99.81	0.63
KING_EIDER-GAR-3-97	42.66	0.11	21.58	8.19	0.47	19.42	4.63	0.01	3.69	100.76	0.81
KING_EIDER-GAR-3-77	42.93	0.09	21.22	7.54	0.40	19.93	4.23	0.06	3.48	99.88	0.82
SANDPIPER-GAR-5-65	43.11	0.10	21.31	7.79	0.36	21.47	4.26	0.03	2.75	101.18	0.83
SANDPIPER-GAR-5-66	42.65	1.02	16.70	6.90	0.35	20.19	6.09	0.08	6.63	100.61	0.84
SANDPIPER-GAR-5-67	42.33	0.13	22.68	11.50	0.37	18.10	3.78	0.07	0.18	99.14	0.74
JAEGER-GAR-4-20	41.28	0.13	22.20	17.06	0.33	11.06	8.27	0.06	0.04	100.43	0.54
JAEGER-GAR-4-18	42.84	0.09	21.05	7.92	0.36	20.84	4.62	0.00	3.14	100.86	0.82
JAEGER-GAR-4-44	43.45	0.14	20.24	7.79	0.39	20.04	4.58	0.05	3.64	100.32	0.82
JAEGER-GAR-4-58	43.00	0.14	20.96	7.93	0.43	20.75	4.48	0.04	2.78	100.51	0.82
JAEGER-GAR-4-59	42.75	0.08	22.68	10.19	0.24	14.04	10.66	0.14	0.12	100.90	0.71
JAEGER-GAR-4-83	42.07	0.14	22.41	13.60	0.32	13.09	8.80	0.06	0.07	100.56	0.63
JAEGER-GAR-4-84	42.09	0.02	16.07	7.68	0.48	17.42	6.69	0.07	9.56	100.08	0.80
JAEGER-GAR-4-77	42.36	0.11	23.20	12.43	0.27	11.91	10.93	0.03	0.08	101.32	0.63
JAEGER-GAR-4-56	41.71	0.12	22.41	12.43	0.29	12.21	11.09	0.12	0.09	100.47	0.64
JAEGER-GAR-4-35	42.44	0.08	21.80	14.55	0.38	16.58	3.50	0.03	0.15	99.51	0.67
JAEGER-GAR-4-26	41.93	0.07	22.25	13.22	0.34	16.27	5.24	0.02	0.18	99.52	0.69
JAEGER-GAR-4-7	42.48	0.13	22.35	16.50	0.35	11.21	8.22	0.09	0.05	101.38	0.55
JAEGER-GAR-4-47	43.59	0.12	20.42	7.45	0.35	20.39	4.43	0.02	2.96	99.73	0.83
JAEGER-GAR-4-33	41.80	0.11	22.56	11.93	0.32	12.38	11.62	0.07	0.04	100.83	0.65
JAEGER-GAR-4-28	41.83	0.11	21.96	12.93	0.31	11.92	11.09	0.08	0.08	100.31	0.62
JAEGER-GAR-4-29	42.30	0.14	22.23	12.70	0.29	14.83	7.46	0.09	0.14	100.18	0.68
JAEGER-GAR-4-49	42.17	0.11	21.46	15.32	0.34	11.08	10.00	0.14	0.00	100.62	0.56
JAEGER-GAR-4-71	41.52	0.13	22.36	12.46	0.24	12.13	11.13	0.08	0.06	100.11	0.63



















## A7.2 Thermobarometry

### A7.2.1 Single Clinopyroxene

It should be noted that only 30% of industry run samples passed the filters required to use the single-clinopyroxene method, compared to the 60% of WDS samples. Only those samples with both the EDS and WDS data producing both a temperature and pressure, and that met the filters are used for Figure A7.3 and supplied in Table A7.5.

Temperatures and pressures derived using the Nimis and Taylor (2000) single clinopyroxene thermobarometer result in data clumps when solved iteratively. When using fixed pressures, concentrate data results in lower temperatures, due to the over estimates of Na<sub>2</sub>O. It is therefore important that quickly run concentrate compositions common to industry should be used with caution, as they will produce warmer geotherms than may actually exist.

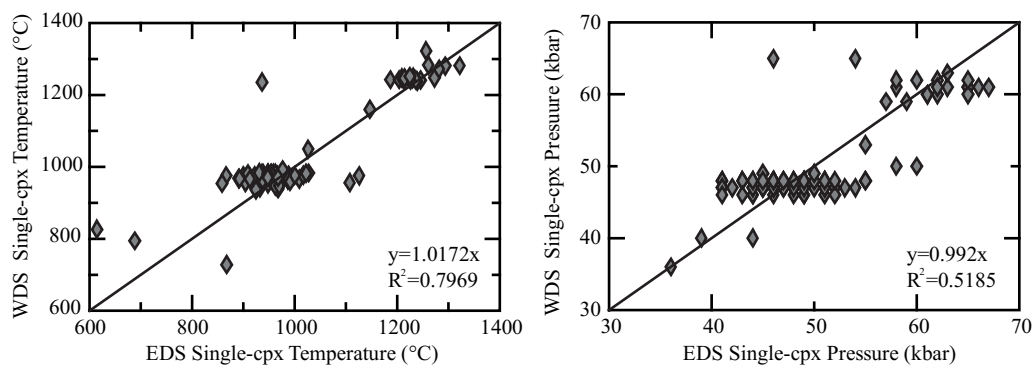


Figure A7.3 Comparison of temperatures and pressures produced by the Nimis and Taylor (2000) single clinopyroxene thermobarometer. EDS appears to report a broader range of temperatures over the 800-1000°C and pressures of 40-60kbar that are more concise when using WDS. The trend line equation implies on average 1:1 ratios between the methods, however lower  $R^2$  values more accurately reflect the lack of correlation displayed by data clumping.

Table A7.5 Comparison between University of Alberta WDS and Industry EDS and the resulting difference to single-clinopyroxene thermobarometry.

Grain ID	Debeers		UofA Probe	
	Temp (°C)	P(kbar)	Temp (°C)	P(kbar)
SNOW_GOOSE-CPX-8-4	957	43	967	48
SNOW_GOOSE-CPX-8-5	866	43	975	48
SNOW_GOOSE-CPX-8-6	900	41	976	48
SNOW_GOOSE-CPX-8-8	951	46	974	48
SNOW_GOOSE-CPX-8-9	971	51	968	46
SNOW_GOOSE-CPX-8-11	966	52	977	47
SNOW_GOOSE-CPX-8-14	931	51	969	48
SNOW_GOOSE-CPX-8-15	904	46	955	46
SNOW_GOOSE-CPX-8-18	968	48	950	47
SNOW_GOOSE-CPX-8-19	936	49	983	46
SNOW_GOOSE-CPX-8-20	938	41	980	48
SNOW_GOOSE-CPX-8-22	913	41	971	47
SNOW_GOOSE-CPX-8-23	935	43	970	46
SNOW_GOOSE-CPX-8-24	937	47	971	48
SNOW_GOOSE-CPX-8-25	890	42	968	47
SNOW_GOOSE-CPX-8-28	928	48	964	47
SNOW_GOOSE-CPX-8-30	908	49	981	48
SNOW_GOOSE-CPX-8-31	924	50	969	47
SNOW_GOOSE-CPX-8-37	977	49	972	48
SNOW_GOOSE-CPX-8-38	892	44	967	48
SNOW_GOOSE-CPX-8-39	970	44	948	46
SNOW_GOOSE-CPX-8-40	926	50	966	48
SNOW_GOOSE-CPX-8-41	858	44	954	47
SNOW_GOOSE-CPX-8-45	933	47	957	47
SNOW_GOOSE-CPX-8-47	947	48	963	47
SNOW_GOOSE-CPX-8-48	932	46	942	48
SNOW_GOOSE-CPX-8-50	928	46	968	47
SNOW_GOOSE-CPX-8-53	987	48	963	46
SNOW_GOOSE-CPX-8-54	937	44	968	46
SNOW_GOOSE-CPX-8-55	938	41	962	47
SNOW_GOOSE-CPX-8-57	946	45	971	47
SNOW_GOOSE-CPX-8-58	948	49	953	46
SNOW_GOOSE-CPX-8-59	935	44	965	47
SNOW_GOOSE-CPX-8-61	948	46	977	47
SNOW_GOOSE-CPX-8-62	967	45	939	47
SNOW_GOOSE-CPX-8-63	958	47	982	47
SNOW_GOOSE-CPX-8-64	921	45	975	47
SNOW_GOOSE-CPX-8-65	949	45	975	49
SNOW_GOOSE-CPX-8-67	937	46	963	48
SNOW_GOOSE-CPX-8-68	930	51	984	47
SNOW_GOOSE-CPX-8-71	1107	53	956	47
SNOW_GOOSE-CPX-8-74	963	49	977	48
SNOW_GOOSE-CPX-8-75	988	49	978	47
SNOW_GOOSE-CPX-8-76	962	51	982	48
SNOW_GOOSE-CPX-8-77	912	44	966	48

Table A7.5 Con't

Grain ID	Debeers		UofA Probe	
	Temp (°C)	P(kbar)	Temp (°C)	P(kbar)
SNOW_GOOSE-CPX-8-78	954	45	964	48
SNOW_GOOSE-CPX-8-81	1008	46	965	47
SNOW_GOOSE-CPX-8-82	947	48	982	48
SNOW_GOOSE-CPX-8-84	976	46	992	48
SNOW_GOOSE-CPX-8-85	954	47	983	48
SNOW_GOOSE-CPX-8-88	953	46	981	48
SNOW_GOOSE-CPX-8-89	947	49	982	48
SNOW_GOOSE-CPX-8-90	987	51	964	47
SNOW_GOOSE-CPX-8-91	962	52	947	46
SNOW_GOOSE-CPX-8-93	969	48	947	47
SNOW_GOOSE-CPX-8-94	991	48	959	48
SNOW_GOOSE-CPX-8-100	947	41	971	46
SNOW_GOOSE-CPX-20-19	936	46	1236	65
SNOW_GOOSE-CPX-20-58	1125	55	975	53
SNOW_BUNTING-CPX-15-1	924	55	936	48
SNOW_BUNTING-CPX-15-50	1146	60	1160	50
SNOW_GOOSE-CPX-4-23	1027	51	983	48
SNOW_GOOSE-CPX-4-25	1016	52	977	48
SNOW_GOOSE-CPX-4-40	1000	50	976	49
SNOW_GOOSE-CPX-4-56	1022	55	982	48
SNOW_GOOSE-CPX-4-59	967	54	970	47
SANDPIPER-CPX-8-41	614	39	826	40
SNOW_BUNTING-CPX-8-77	1026	58	1049	50
SNOW_BUNTING-CPX-8-93	688	44	794	40
TURNSTONE-CPX-11-3	1321	62	1282	62
TURNSTONE-CPX-11-15	1272	66	1248	61
TURNSTONE-CPX-11-16	867	36	728	36
TURNSTONE-CPX-11-54	1293	58	1281	61
TURNSTONE-CPX-11-66	1256	54	1323	65
TURNSTONE-CPX-11-98	1281	62	1272	60
TURNSTONE-CPX-11-95	1245	61	1242	60
TURNSTONE-CPX-11-87	1238	62	1238	61
TURNSTONE-CPX-11-86	1230	58	1245	62
TURNSTONE-CPX-6-2	1213	63	1242	61
TURNSTONE-CPX-6-5	1186	61	1243	60
TURNSTONE-CPX-6-8	1231	57	1249	59
TURNSTONE-CPX-6-10	1260	60	1283	62
TURNSTONE-CPX-6-11	1203	59	1243	59
TURNSTONE-CPX-6-13	1209	65	1247	61
TURNSTONE-CPX-6-14	1236	65	1242	61
TURNSTONE-CPX-6-16	1223	63	1248	63
TURNSTONE-CPX-6-34	1225	65	1241	60
TURNSTONE-CPX-6-37	1214	65	1247	62
TURNSTONE-CPX-6-40	1224	67	1252	61

### **A7.2.2 Ni-in-Garnet**

See section A5.2.2 for Ni-in-garnet temperatures attained using garnet trace elements. Generally, concentrate defines a broader temperature range than that of the xenoliths, but a very similar median (see thesis Figure 4.14)

### **A7.3 Garnet trace elements**

Table A7.6 Concentrate garnets by xenolith garnet trace element trends

Trend	Number of Grains
Type I	37
Type II	1
Type IIIa	4
Type IIIb	8

## Appendix A8 Model ages

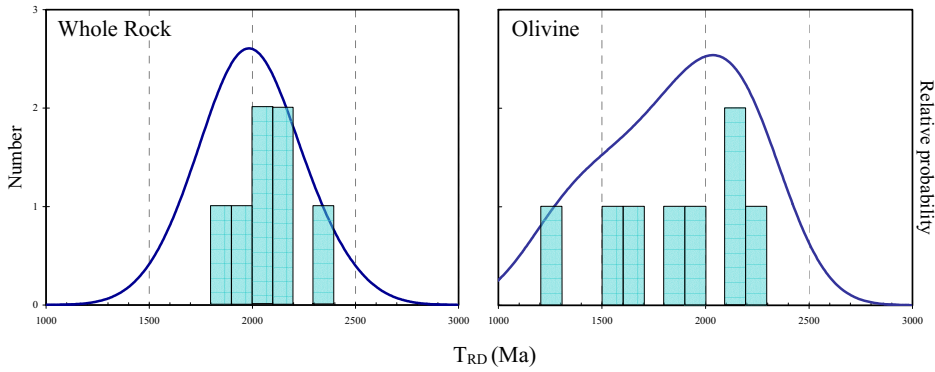


Figure A8.1  $T_{RD}$  model ages for Parry Peninsula whole rock and olivines. Whole rock ages display the same 2000 Ma peak defined by both populations together as well as CVI whole rocks. PP olivines have a slightly lower peak and are broadly younger.

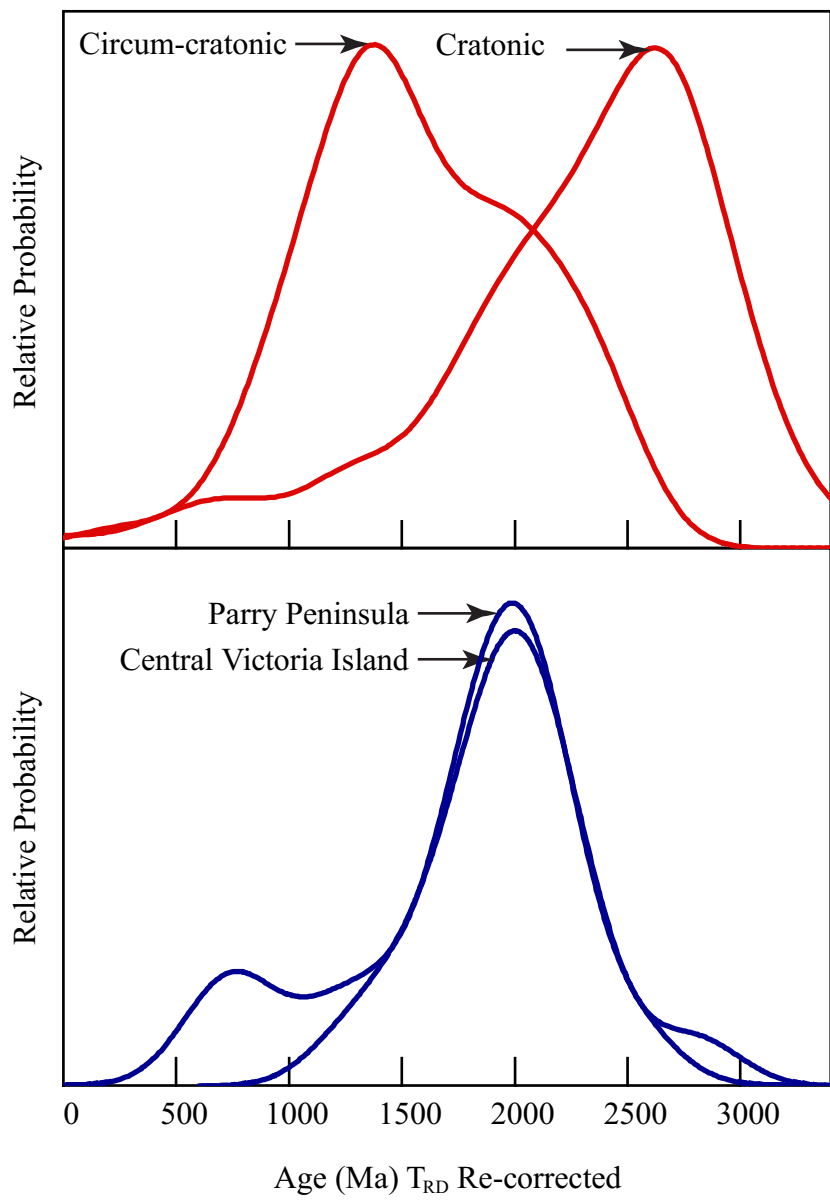


Figure A8.2 Probability density figure of  $T_{RD}$  model ages for central Victoria Island and Parry Peninsula plotted against those for cratonic and circum-cratonic (dataset from Pearson et al., 2004)

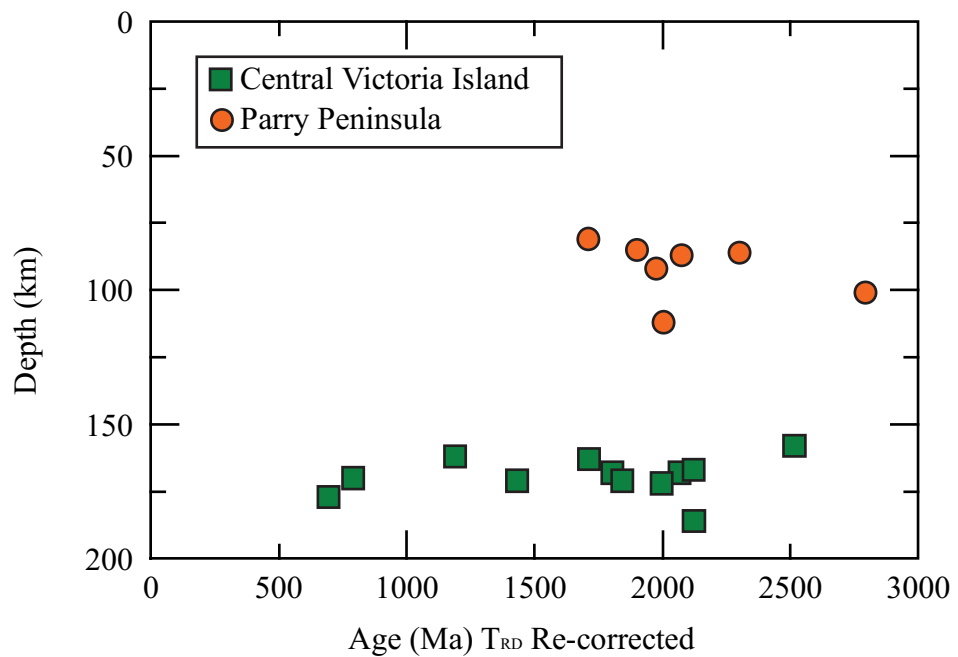


Figure A8.3  $T_{RD}$  Age versus depth. Depths for central Victoria are extrapolated from Ni-in-garnet temperature to the FITPLOT geotherm. Depths for Parry Peninsula are from the single-clinopyroxene calculations from Section 3.4.2. No systematic relationships are observed in the age-depths in either suite.